

# How the Kerr-Cat Qubit Dies—And How to Rescue It

Othmane Benhayoune-Khadraoui,<sup>1</sup> Cristóbal Lledó,<sup>1,2</sup> and Alexandre Blais<sup>1,3</sup>

<sup>1</sup>*Institut Quantique and Département de Physique,*

*Université de Sherbrooke, Sherbrooke J1K 2R1 Quebec, Canada*

<sup>2</sup>*Departamento de Física, Facultad de Ciencias Físicas y Matemáticas, Universidad de Chile, Santiago 837.0415, Chile*

<sup>3</sup>*CIFAR, Toronto, ON M5G 1M1, Canada*

(Dated: July 9, 2025)

Kerr-cat qubits have been experimentally shown to exhibit a large noise bias, with one decay channel suppressed by several orders of magnitude. In superconducting implementations, increasing the microwave drive on the nonlinear oscillator that hosts the Kerr-cat qubit should, in principle, further enhance this bias. Instead, experiments reveal that above a critical drive amplitude the tunneling time — the less dominant decay channel — ceases to increase and even decreases. Here, we show that this breakdown arises from the multimode nature of the circuit implementation: specifically, the buffer mode used to control the Kerr-cat qubit can induce multiphoton resonances that sharply degrade Kerr-cat coherence if its frequency is not carefully chosen. We uncover this mechanism by retaining the full circuit nonlinearities and treating the strong drive exactly within a Floquet–Markov framework that incorporates quasidegeneracies in the Kerr-cat spectrum. Our results not only provide an explanation for the sudden reduction of the tunneling time but also demonstrate the robustness of the Kerr-cat qubit when its surrounding electromagnetic environment is carefully engineered.

## I. INTRODUCTION

Bosonic codes are promising candidates for achieving fault tolerance with minimal hardware overhead, a feature often referred to as hardware efficiency [1–7]. These codes leverage the large Hilbert space of an oscillator to encode logical information in a carefully chosen  $d$ -dimensional subspace. A particularly compelling example is the cat qubit, where the logical states are encoded in the manifold spanned by superposition of coherent states  $|\alpha\rangle$  referred to as Schrödinger cat states,  $|C_\alpha^\pm\rangle = (|\alpha\rangle \pm |-\alpha\rangle)/N_\alpha^\pm$  with  $N_\alpha^\pm$  the normalization [8]. This choice is motivated by the fact that local noise—acting locally in the oscillator’s phase space—induces transitions between  $|+\alpha\rangle$  and  $|-\alpha\rangle$  with rates that are exponentially suppressed in  $|\alpha|^2$  [9–11]. This suppression of phase-flip errors is only modestly counterbalanced by a linear in  $|\alpha|^2$  increase in the rate of bit-flip errors—that is, transitions between the cat states  $|C_\alpha^+\rangle$  and  $|C_\alpha^-\rangle$ —induced by local noise. The resulting large noise bias can be leveraged to implement error correction protocols with minimal hardware resources [12–20].

In superconducting quantum circuits, the two main types of cat qubits are the dissipative cat qubit [10, 21–27] and the Kerr-cat qubit [11, 28–34]. In the dissipative approach, engineered dissipation stabilizes a steady-state manifold that spans the desired cat-states subspace. By contrast, the Kerr-cat approach relies on Hamiltonian engineering where the cat states emerge as degenerate eigenstates of the squeezed Kerr Hamiltonian

$$\begin{aligned}\hat{H}_{\text{SK}} &= -K\hat{a}^{\dagger 2}\hat{a}^2 + \varepsilon_2\hat{a}^{\dagger 2} + \varepsilon_2^*\hat{a}^2, \\ &= -K(\hat{a}^{\dagger 2} - \alpha^{*2})(\hat{a}^2 - \alpha^2) + K|\alpha|^4,\end{aligned}\quad (1)$$

where  $\hat{a}$  is the annihilation operator of the oscillator,  $\varepsilon_2$  is the strength of the two-photon drive, and  $K$  is the self-

Kerr nonlinearity. The factorized form of  $\hat{H}_{\text{SK}}$  makes it explicit that the coherent states  $|\pm\alpha\rangle$  with  $\alpha = \sqrt{\varepsilon_2/K}$  are degenerate eigenstates of the Hamiltonian [11]. Their symmetric and antisymmetric superpositions are the cat states  $|C_\alpha^\pm\rangle$ , whose average photon number is given by  $|\alpha|^2 = |\varepsilon_2|/K$ .

To gain intuition into the structure of this Hamiltonian, it is useful to analyze its phase-space representation  $H(\text{Re}[\alpha], \text{Im}[\alpha])$ , obtained via the Weyl correspondence [35]. This metapotential, shown in Fig. 1(a), exhibits a double-well structure with a barrier height  $\sim K|\alpha|^4$  separating two minima centered at  $\pm\alpha$ , corresponding to the locations of the Kerr-cat coherent states. As the two-photon drive and hence  $|\alpha|^2$  is increased, pairs of states successively enter the wells. As they drop deeper into the potential landscape, tunneling between them is rapidly suppressed because of the barrier. This leads to spectral kissing, where pairs of energy levels become nearly degenerate; see Fig. 1(b), with circles indicating the kissing of different pairs [30].

In practice, however, the exponential suppression of tunneling between the coherent states at the bottom of the well does not persist indefinitely with increasing  $|\alpha|^2$ . Thermal excitation from these coherent states to higher-lying states that have not yet kissed can restore tunneling between the wells [36–38]. This phenomenon repeats itself as each new pair of states enters the wells, resulting in a staircase-like dependence of the tunneling time with  $|\alpha|^2$ . This behavior has been measured experimentally [30, 32] and studied theoretically using perturbative methods [39]. More strikingly, at still larger photon numbers, the staircase behavior breaks down: the tunneling time is observed to decrease with increasing photon number, accompanied by sharp features at specific values of the drive amplitude [34, 40]. While existing theoretical models capture the qualitative features of the staircase

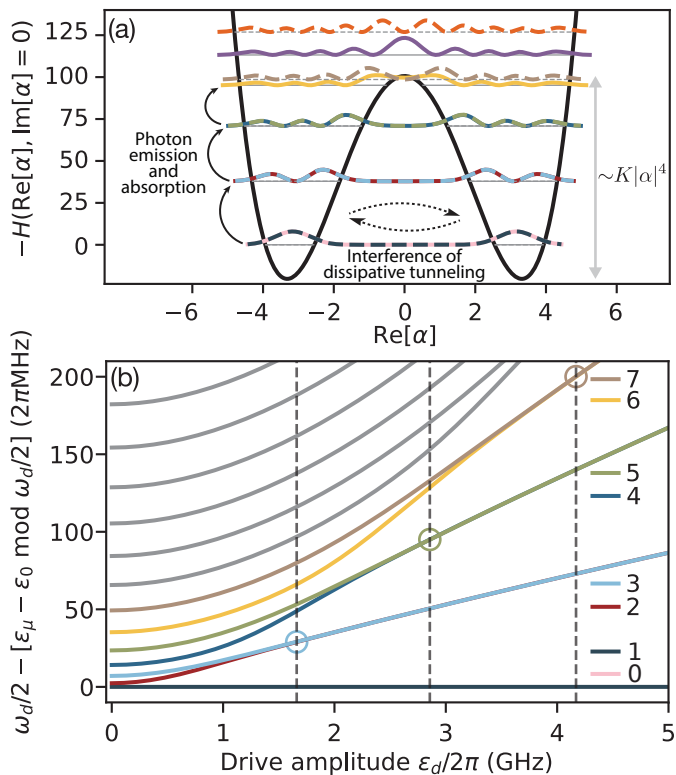


FIG. 1. (a) Cut along  $\text{Re}[\alpha]$  of the metapotential associated with the shifted squeezed Kerr Hamiltonian  $\hat{H}_{\text{SK}} - \varepsilon_2^2/K$  for  $\varepsilon_2 = 10$  and  $K = 1$ . Horizontal gray lines indicate the eigenenergies, and the colored curves the marginals of the Wigner distributions of the corresponding eigenstates. For the quasidegenerate level pairs 0–1, 2–3, and 4–5, dissipative tunneling across the double well is suppressed due to destructive interference between two relaxation pathways. Population transfer between wells can instead occur by climbing the energy ladder—via photon emission and absorption—until nondegenerate levels (here 6 and 7) are populated. The number of quasidegenerate level pairs within the well is controlled by the photon number  $|\alpha|^2 = \varepsilon_2/K = 10$ . (b) Floquet quasienergy spectrum of the Kerr-cat qubit showing spectral kissings (circles) where the quasienergy differences between pairs of excited states asymptotically approach  $\omega_d/2$ . Dashed lines indicate drive amplitudes at which these differences become comparable to the decay rate. The circuit parameters are chosen close to those of Ref. [30], with  $E_J/2\pi = 272.436$  GHz,  $E_C/2\pi = 107.8$  MHz,  $\alpha = 0.046$ , and  $\varphi_{\text{ext}} = 0.33 \times 2\pi$ , yielding a 0–1 transition frequency  $\omega_{01}/2\pi = 6.094$  GHz and a self-Kerr nonlinearity  $K/2\pi = 1.18$  MHz.

regime, they do not quantitatively match the experimental data. Moreover, the breakdown of the staircase pattern is not reproduced by current theoretical approaches, raising the question of whether this discrepancy reflects limitations of the perturbative treatment or the presence of additional mechanisms not yet accounted for in the theory.

In this work, we answer this question by showing that both the breakdown of the staircase behavior of the tun-

neling time and the appearance of sharp resonances originate from the multimode nature of the circuit implementation of the Kerr-cat qubit in Refs. [34, 41] and can be captured by a model foregoing any perturbative expansion but including additional modes of the circuit. In the absence of additional modes, we find that the Kerr-cat qubit is remarkably robust. This observation suggests that engineering the Kerr-cat’s electromagnetic environment such as to avoid the presence of these modes can lead to significantly longer tunneling times than currently observed experimentally.

These results are obtained using three key ingredients. First, we retain the full nonlinear potential of the circuit, as any finite-order expansion of the potential risks missing the resonances between the nonlinear oscillator and the other degrees of freedom in the circuit. Second, the drive is treated exactly using the Floquet formalism, ensuring that multiphoton processes and nonlinear effects are fully accounted for. This type of multiphoton process has already been shown to be at the origin of ionization of highly-excited atoms driven by a microwave field [42] and of drive-induced resonances of the transmon qubit [43–52]. Third, we incorporate the interplay between the drive and dissipation by employing the partial secular Floquet–Markov master equation [53–55]. This approach captures the coherent interplay between different relaxation channels—an essential feature to accurately model dissipation in the Kerr-cat qubit.

This paper is organized as follows. In Sec. II we review the standard single-mode approximation of the Kerr-cat qubit. We then show how Floquet theory reproduces essential features of this system, such as spectral kissing, and introduce a form of the Floquet–Markov Lindblad master equation that accounts for these near-degeneracies. Using this framework, we compute the tunneling time of the Kerr-cat qubit, demonstrating its intrinsic robustness. In Sec. III, we incorporate the buffer mode used to drive the Kerr-cat qubit in experiments, and show that it leads to an abrupt reduction of the tunneling time above a critical drive amplitude. In Sec. IV and Appendix G we examine the effects of SNAIL array modes and of a stray geometric inductance on the qubit’s coherence. Further details of the derivations can be found in the Appendices. Our findings are summarized in Sec. V.

## II. SINGLE-MODE DESCRIPTION

Experimental realizations of the Kerr-cat qubit in circuit QED rely on superconducting nonlinear asymmetric inductive elements (SNAIL) [41, 56] shunted by a large capacitance and controlled via a buffer mode, see Fig. 2(a) [29–34]. In this section, we analyze the behavior of the Kerr-cat qubit in the single-mode approximation of this circuit, identifying the key assumptions underlying this simplification. While sufficient to reproduce the physics of the spectral kissing and the observed plateaus

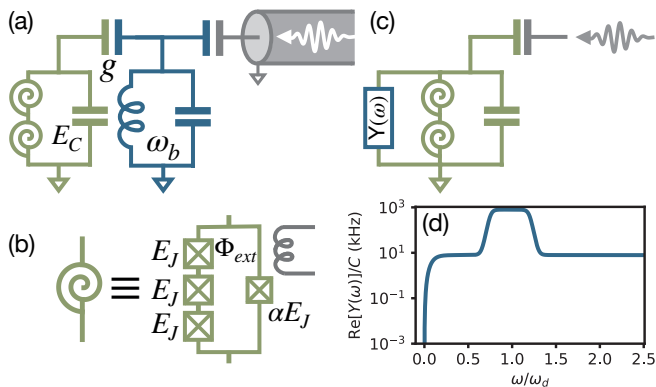


FIG. 2. (a) Circuit implementation of the Kerr-cat qubit, consisting of an array of SNAILS shunted by a large capacitor (green) and driven through a buffer mode (blue) whose resonance frequency is close to the drive frequency. (b) Circuit diagram of a single SNAIL composed of an array of large Josephson junctions with energy  $E_J$  in parallel with a smaller junction of energy  $\alpha E_J$ , forming a loop threaded by an external magnetic flux (gray). (c) Semiclassical representation of the circuit in (a), where the driven buffer mode is replaced by a classical drive (gray) and a dissipative environment modeled by an admittance  $Y(\omega)$  (blue). (d) Typical spectral density  $J(\omega) = \text{Re}[Y(\omega)]/C$  featuring a broad peak around the drive frequency  $\omega_d$  reflecting the low quality factor of the buffer mode. The values around  $J(m\omega_d/2)$  for  $m \in \mathbb{Z}^+$  are taken from Ref. [39].

in the tunneling time [30, 32], we find that this reduced model does not capture the observed abrupt reduction of the tunneling time above a drive amplitude threshold. Building on these observations, in the next section, we show how this breakdown is captured when accounting for the multimode nature of the circuit of Fig. 2(a). The present section introduces the key ideas and methods necessary to understand this more general multimode case.

Accounting for the buffer mode, the Hamiltonian describing the circuit of Fig. 2(a) reads ( $\hbar = 1$ )

$$\hat{H}'' = \omega_b \hat{a}_b^\dagger \hat{a}_b + \hat{H}_s + ig\hat{n} (\hat{a}_b^\dagger - \hat{a}_b) + i\Omega(t) (\hat{a}_b^\dagger - \hat{a}_b). \quad (2)$$

In this expression,  $\omega_b$  is the frequency of the buffer mode with annihilation operator  $\hat{a}_b$ . The implementation of the buffer mode varies depending on the experiment: it may correspond to a 3D box mode defined by the cavity geometry [29–31, 34], a stripline resonator that facilitates parametric driving of the SNAILS [33], or a filter mode engineered to suppress Purcell loss around the qubit frequency without compromising the drive strength [32]. In all cases, the presence of this mode is intentional, with its resonance frequency engineered to be close to that of the drive frequency to allow driving the SNAIL. The second term of Eq. (2),  $\hat{H}_s$  is the SNAIL array Hamiltonian defined below. The third term corresponds to the coupling of the buffer mode to the SNAIL array with

$g$  the strength of that coupling and  $\hat{n}$  the SNAIL array charge operator. The last term corresponds to a charge drive  $\Omega(t) = \Omega_0 \sin(\omega_d t)$  applied to the buffer mode at frequency  $\omega_d$ . To see more clearly how the drive on the buffer effectively acts on the SNAIL array, we displace the buffer mode by its classical response using a displacement transformation [57]. This results in the displaced Hamiltonian

$$\hat{H}' = \omega_b \hat{a}_b^\dagger \hat{a}_b + \hat{H}_s + ig\hat{n} (\hat{a}_b^\dagger - \hat{a}_b) + \varepsilon_d \cos(\omega_d t) \hat{n}, \quad (3)$$

where  $\varepsilon_d$  is the amplitude of the effective drive proportional to the square root of the buffer mode photon population. So far, no approximations have been made; the displacement transformation being exact, see Refs. [47, 58] for instance. In the following, we use  $\varepsilon_d$  rather than  $\Omega_0$  as a measure of the drive strength. As a first approximation, following Refs. [46, 47], we ignore quantum fluctuations in the buffer mode resulting in the simplified Hamiltonian

$$\hat{H} \simeq \hat{H}_s + \varepsilon_d \cos(\omega_d t) \hat{n}, \quad (4)$$

which describes a voltage-driven SNAIL, as illustrated in Fig. 2(c). We go beyond this approximation in Sec. III by accounting for the buffer mode exactly.

As illustrated in Fig. 2(a,b), the circuit is built from an array of two SNAILS, each comprised of an array of three identical large Josephson junctions with energy  $E_J$  in parallel with a smaller junction of energy  $\alpha E_J$  (with  $\alpha < 1$ ). Assuming that the total phase drop across the array is evenly distributed among the six large junctions allows the SNAIL array to be described by a single degree of freedom. This single-phase approximation relies on the assumption that this forms a weakly nonlinear oscillator whose resonance frequency  $\omega_0$  is much smaller than the plasma frequency of the individual large junctions. This condition is satisfied provided the stray capacitance  $C_{J,g}$  to ground of each island in the array is small ( $C_{J,g} \ll C_J/6^2$ ) [59–61]. We go beyond this approximation in Sec. IV where we analyze the influence of higher-frequency collective modes of the array on both the spectrum and lifetime of the Kerr-cat qubit.

Under the single-phase approximation, the Hamiltonian of the capacitively shunted double SNAIL is given by

$$\begin{aligned} \hat{H}_s = & 4E_C \hat{n}^2 - 6E_J \cos\left(\frac{\hat{\varphi}}{6}\right) \\ & - 2\alpha E_J \cos\left(\frac{\hat{\varphi}}{2} + \varphi_{\text{ext}}\right), \end{aligned} \quad (5)$$

where  $E_C$  denotes the charging energy dominated by the shunting capacitance, and  $\varphi_{\text{ext}} = 2\pi\Phi_{\text{ext}}/\Phi_0$  the external reduced flux bias of each SNAIL. The operators represent the phase  $\hat{\varphi}$  across the SNAIL array and its canonically conjugate charge  $\hat{n}$ .

Introducing the annihilation operator  $\hat{a}$  of the shunted SNAIL such that  $\hat{\varphi} = \varphi_{\text{zpf}}(\hat{a} + \hat{a}^\dagger)$ , where  $\varphi_{\text{zpf}}$  represents

quantum fluctuations of the phase operator, we expand the potential energy terms of Eq. (5) to fourth order in  $\varphi_{\text{zpf}}$ . Choosing the drive frequency  $\omega_d \approx 2\omega_0$ , and moving to the appropriate frame and applying the rotating-wave approximations (RWA), the single-mode Hamiltonian of Eq. (4) takes the standard form of the Kerr-cat Hamiltonian Eq. (1) [29]. This approximate model is sufficient to capture the basic properties of the system [11]. However, in the context of measurement-induced state transitions in the transmon [43, 47, 62], making these approximations (cosine potential expansion and RWA) substantially modifies the threshold drive amplitude before transitions are observed. We expect these approximations to similarly modify the threshold of the breakdown of the staircase behavior of the Kerr-cat. For this reason, in this work we use the full cosine potential of Eq. (5).

To accurately account for the effect of the strong drive, we use Floquet theory. At any time, the state of the system can be decomposed in terms of periodic Floquet modes  $|\phi_\mu(t)\rangle = |\phi_\mu(t+T)\rangle$  and their corresponding quasienergies  $\epsilon_\mu$ , which satisfy the eigenvalue equation

$$\hat{U}(t+T, t) |\phi_\mu(t)\rangle = e^{-i\epsilon_\mu T} |\phi_\mu(t)\rangle, \quad (6)$$

where  $\hat{U}(t+T, t)$  is the unitary propagator over one period  $T = 2\pi/\omega_d$  of the drive [55]. The Floquet modes and quasienergies are obtained by numerically diagonalizing this operator. Since they are obtained as the argument of a phase, the quasienergies are defined modulo the drive frequency,  $\epsilon_\mu \in [-\omega_d/2, \omega_d/2)$ . Hereinafter, we denote  $|\phi_\mu\rangle \equiv |\phi_\mu(0)\rangle$  the Floquet modes at time  $t = 0$ . At  $\epsilon_d = 0$ , the quasienergies coincide with the eigenenergies (modulo  $\omega_d$ ) of the undriven double-SNAIL Hamiltonian  $\hat{H}_s$ , and the Floquet modes reduce to the corresponding undriven eigenstates. Starting from this point, we increment  $\epsilon_d$  in small steps and assign labels to the Floquet spectrum at each step by maximizing their modes' overlap with the modes at the previous drive amplitude. This procedure enables a consistent tracking of each mode based on its origin in the undriven spectrum [42, 47, 63].

Increasing the drive amplitude, the two lowest Floquet modes,  $\mu = 0, 1$ , continuously evolve from the ground and first excited states of the undriven Hamiltonian  $\hat{H}_s$  into (displaced) cat states, see Fig. 3(a) showing the Wigner distributions of these modes for  $\epsilon_d/2\pi = 2.5$  GHz. Unlike in the approximate squeezed-Kerr Hamiltonian Eq. (1), where the cat eigenstates are centered at the origin, here they are slightly displaced because they are displayed in the laboratory frame and not the displaced frame. Importantly, in these calculations, to compensate for the ac-Stark shift the drive frequency  $\omega_d$  is adjusted at each value of the drive amplitude to match twice the Floquet quasienergy difference between the two lowest modes,  $\omega_d = 2|\epsilon_1 - \epsilon_0|$ . This mirrors the experimental procedures used, for example, in Refs. [30, 33, 34]. Away from this choice of frequency, the Floquet modes  $\mu = 0$  and 1 associated with the Hamiltonian in Eq. (4) no longer correspond to symmetric superpositions of opposite coherent states in phase space [31, 34].

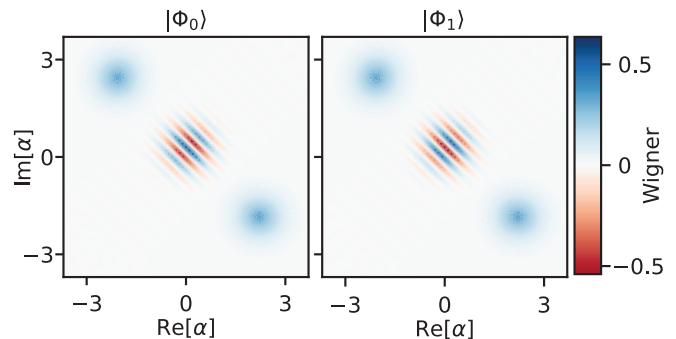


FIG. 3. (a) Wigner distributions of the first two Floquet modes,  $|\phi_0\rangle$  and  $|\phi_1\rangle$ , at a drive amplitude  $\epsilon_d/2\pi = 2.5$  GHz corresponding to approximately nine photons in the cat manifold. These two modes are the logical cat states.

### A. Spectral kissing in the presence of strong drive and full nonlinearities

Having obtained the Floquet spectrum as a function of the drive amplitude, it is useful to present it in a way that facilitates comparison with the spectroscopy measurements reported in Refs. [30–33], see Appendix A for more details. To do so, we first unfold the quasienergies from the Floquet Brillouin zone  $[-\omega_d/2, \omega_d/2)$  onto the real line, and then re-fold them modulo  $\omega_d/2$  relative to the ground state energy. This results in the spectrum shown in Fig. 1(b) with a series of pairwise degeneracies, or spectral kissings (circles). This spectral kissing is a crucial feature of the ideal squeezed Kerr oscillator Hamiltonian of Eq. (1) which we also observe—consistent with experiments—when using the full nonlinear model of Eq. (5).

Remarkably, the quasienergy spectrum of the Kerr-cat remains free of avoided crossings indicative of unwanted resonances up to  $\epsilon_d/2\pi = 10$  GHz, corresponding to 36 photons—the maximum amplitude considered in our simulations (not shown). This is in stark contrast to other qubits under strong drives, such as the transmon, where the quasienergy spectra show a multitude of avoided crossings resulting from unwanted multiphoton resonances [43–50]. Crucially, in the transmon the quasienergies corresponding to the computational states experience an ac-Stark shift of opposite sign to that of states near the top of the transmon's cosine potential (where the anharmonicity changes sign). This can lead to a collision of quasienergies at a ‘critical’ drive amplitude and to unwanted transitions from the computational states to highly-excited states. Because the transmon's cosine potential is relatively shallow and only supports of the order of  $\sim 10$  states, these collisions typically occur at moderate drive amplitudes. The situation is very different in the Kerr-cat qubit, whose robustness to multiphoton resonances results from its very deep potential well. Indeed, for the parameters used in this work, which are close to those of the experiment of Ref. [30] (see

the caption of Fig. 1(b)), the number of bound states in the SNAIL well is approximately 530. As a result, all the relevant levels—including the cat-states and higher-excited levels—experience an ac-Stark shift of the same sign. Collisions of quasienergies are thus avoided up to very large drive amplitudes. This observation suggests that the single-mode approximation of the Kerr-cat qubit does not contain the necessary ingredients to capture the sudden decrease of the tunneling time with drive amplitude. The same conclusion can be reached by considering this system from the point of classical chaos [46, 64].

### B. Floquet-Markov-Lindblad with quasidegenerate transitions

To fully account for the effect of the drive and SNAIL nonlinearity, we employ the Floquet-Markov master equation [54, 55, 65]. In contrast to the standard quantum optics master equation—where dissipation is treated as incoherent transitions between eigenstates of a time-independent Hamiltonian [66]—the Floquet-Markov approach describes dissipation in terms of transitions between Floquet modes. Crucially, the corresponding rates account for processes involving simultaneous absorption or emission of drive photons and environment photons [55, 67].

In the context of the Kerr-cat, it is essential for the master equation to capture the spectral kissing of the quasienergies. As a result, in the derivation of the master equation we cannot employ the commonly used secular approximation which assumes that all transition frequencies are well separated, leading to a sum of independent dissipators, one for each transition [55]. Instead, we use a partial secular approximation accounting for the near degeneracy of certain transitions while discarding fast-oscillating off-diagonal terms between widely separated transition frequencies [53, 54]. This approach allows for an accurate description of the dynamics near spectral degeneracies, which are central to the protection of the Kerr-cat coherence.

More precisely, the Floquet-Markov master equation we use is given in the interaction picture by

$$\partial_t \hat{\rho} = \mathcal{D}_{\text{inc}} \hat{\rho} + \mathcal{D}_{\text{coh}} \hat{\rho} \equiv \mathcal{L} \hat{\rho}, \quad (7)$$

with two different collections of dissipators. The first collection

$$\mathcal{D}_{\text{inc}} = \sum_{\mu, \nu, k} \kappa(\Delta_{\mu\nu k}) \mathcal{D}[X_{\mu\nu k} |\phi_\mu\rangle \langle\phi_\nu|], \quad (8)$$

with  $\mathcal{D}[\hat{L}] \hat{\rho} \equiv \hat{L} \hat{\rho} \hat{L}^\dagger - \{\hat{L}^\dagger \hat{L}, \hat{\rho}\}/2$ , takes the form of an incoherent sum of all processes involving transitions that are not nearly degenerate. In this expression,

$$\Delta_{\mu\nu k} = \epsilon_\mu - \epsilon_\nu + k\omega_d \quad (9)$$

is the detuning between Floquet modes  $\mu$  and  $\nu$  up to

$k \in \mathbb{Z}$  drive photons, and

$$X_{\mu\nu k} = \frac{1}{T} \int_0^T e^{-ik\omega_d t} \langle\phi_\mu(t)| i(\hat{a}^\dagger - \hat{a}) |\phi_\nu(t)\rangle dt \quad (10)$$

is a Fourier coefficient of the  $(\mu, \nu)$  matrix element of the SNAIL's charge operator  $\hat{n}/n_{\text{zpf}} = i(\hat{a}^\dagger - \hat{a})$  in the Floquet mode basis at time  $t$ . In Eq. (10), the zero-point fluctuations of the charge operator,  $n_{\text{zpf}}$ , are implicitly included in the definition of  $\kappa(\omega)$ . The index  $k$  accounts for the fact that transitions can involve the emission or absorption of  $|k|$  drive photons. The second collection takes the form

$$\mathcal{D}_{\text{coh}} = \sum_{\mu, \nu, k} \kappa(\Delta_{\mu\nu k}) \mathcal{D} \left[ \sum_{\substack{\mu', \nu', k' \\ \sim (\mu, \nu, k)}} X_{\mu' \nu' k'} |\phi_{\mu'}\rangle \langle\phi_{\nu'}| \right] \quad (11)$$

and is the sum of all processes involving transitions that are quasidegenerate, which are coherently added together inside the dissipators. The prime indices  $(\mu', \nu', k')$  run over triplets for which the associated transition frequency  $\Delta_{\mu' \nu' k'}$  is quasidegenerate with  $\Delta_{\mu\nu k}$ . For the parameters used in this work, we define two transitions  $\Delta_{\mu\nu k}$  and  $\Delta_{\mu' \nu' k'}$  as quasidegenerate when  $|\Delta_{\mu\nu k} - \Delta_{\mu' \nu' k'}|/2\pi < 100$  kHz.

In both collections, the rates are given by

$$\kappa(\omega) = n_{\text{th}}(\omega) J(\omega) + [1 + n_{\text{th}}(-\omega)] J(-\omega), \quad (12)$$

with  $n_{\text{th}}(\omega)$  the thermal population of the environment at frequency  $\omega$ , and  $J(\omega) = \theta(\omega) \text{Re}[Y(\omega)]/C$  the bath spectral density expressed in terms of the external admittance  $Y(\omega)$ , see Fig. 2(c) and (d). With  $\theta(\omega)$  the Heaviside function,  $\kappa(\omega > 0)$  corresponds to absorption from the bath while  $\kappa(\omega < 0)$  to emission. The derivation of this master equation can be found in Appendix B.

For the Kerr-cat qubit, transitions between Floquet modes cluster around harmonics of  $\omega_d/2$  or, in other words,  $\Delta_{\mu\nu k} \sim m\omega_d/2$  with  $m \in \mathbb{Z}$ ; see Fig. 3(b) and Fig. 12(a) in Appendix A. We assume that the spectral density  $J(\omega)$  is flat in the vicinity of each of these harmonics, consistent with the Markovian approximation [68]. Accordingly, we parametrize the spectral density by its values at the relevant harmonics. Since the buffer mode acts as a bandpass filter at  $\omega_d$ , we take  $J(\omega_d) \gg J(\omega_d/2) = J(3\omega_d/2)$ , as illustrated in Fig. 2(c). Moreover, following Ref. [39] we account for imperfect thermalization of the buffer mode resulting in a higher frequency at the drive frequency than at the other harmonics,  $T(\omega_d) > T(\omega_d/2) = T(3\omega_d/2)$ . In Sec. II E, we explore in more detail how the spectral density and the thermal population influence the tunneling rate in the Kerr-cat qubit.

### C. Examples of processes entering $\mathcal{D}_{\text{coh}}$ and $\mathcal{D}_{\text{inc}}$

Before presenting results obtained using the above Floquet-Markov master equation, it is instructive to first

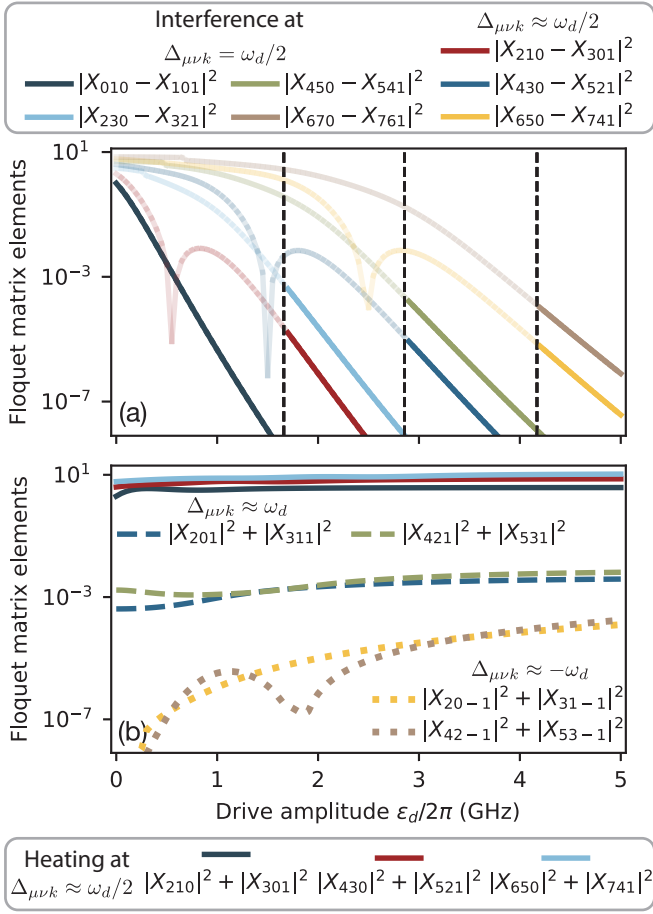


FIG. 4. Matrix elements of the SNAIL charge operator in the Floquet mode basis as a function of drive amplitude, responsible for (a) direct tunneling and (b) intrawell leakage. In (b), we highlight three types of heating processes: solid lines indicate photon absorption at  $\omega_d/2$ , dashed lines at  $\omega_d$ , and dotted lines denote drive-induced processes that persist at zero temperature. Before the kissing between  $\varepsilon_2$  and  $\varepsilon_3$  (left-most vertical dashed line), tunneling is dominated by the intermediate transitions to these modes outside of the metapotential double well, with a rate proportional to  $|X_{210}|^2 + |X_{301}|^2$ , with additional contributions from other transitions whose matrix elements are shown in (b). After the kissing, these dominant processes interfere, and their contribution  $|X_{210} - X_{301}|^2$  to the tunneling rate becomes suppressed. Furthermore, leakage to these modes does not lead to direct tunneling because the rate  $|X_{230} - X_{321}|^2$  also becomes suppressed. This pattern repeats for higher modes at each of the other two spectral kissings indicated by the vertical dashed lines.

consider a few examples of the kinds of processes that enter the dissipators  $\mathcal{D}_{\text{coh}}$  and  $\mathcal{D}_{\text{inc}}$ . First, given the choice of drive frequency  $\omega_d/2 = |\varepsilon_1 - \varepsilon_0|$ , there are exact degeneracies  $\Delta_{010} = \Delta_{101} = \omega_d/2$  and  $\Delta_{100} = \Delta_{01,-1} = -\omega_d/2$  for all drive amplitudes. The corresponding transitions join the same dissipators in  $\mathcal{D}_{\text{coh}}$ . For example, focusing on the transitions of frequency  $\omega_d/2$ , the sum of operators entering  $\mathcal{D}$  in Eq. (11) is  $X_{010} |\phi_0\rangle \langle \phi_1| + X_{101} |\phi_1\rangle \langle \phi_0|$ . Because the cat states

of amplitude  $\pm\alpha$  are approximately given by  $|\phi_{0,1}\rangle \approx (|\beta + \alpha\rangle \pm e^{i\theta} |\beta - \alpha\rangle)/\sqrt{2}$  where  $\beta$  is the displacement from the origin, this expression can be written as

$$\begin{aligned} & X_{010} |\phi_0\rangle \langle \phi_1| + X_{101} |\phi_1\rangle \langle \phi_0| = \\ & \frac{X_{010} + X_{101}}{2} (|\beta + \alpha\rangle \langle \beta + \alpha| - |\beta - \alpha\rangle \langle \beta - \alpha|) \\ & + \frac{X_{010} - X_{101}}{2} |\beta + \alpha\rangle \langle \beta - \alpha| \\ & - \frac{X_{010} - X_{101}}{2} |\beta - \alpha\rangle \langle \beta + \alpha|. \end{aligned} \quad (13)$$

The first term on the right-hand side induces bit flips (logical Pauli  $\hat{X}_L$ ) at a rate proportional to  $|X_{010} + X_{101}|^2$  within the cat qubit manifold. The second and third terms induce transitions between the coherent states corresponding to phase flips (logical Pauli  $\hat{Z}_L$ ) at a rate proportional to  $|X_{010} - X_{101}|^2$ . In other words, these last two terms lead to tunneling between the two wells of the metapotential. As expected from the discussion in Sec. I and shown in Fig. 4 (a), this rate decreases exponentially with increasing drive amplitude (dark blue line) [11, 69].

This noise bias is significantly reduced when higher levels are considered [36–38], something that is captured in the Floquet-Markov master equation of Eq. (7) by the incoherent or coherent addition of transitions before and after level kissings. For example, before kissing, the two heating processes from the states at the bottom of the well,  $\{|\phi_0\rangle, |\phi_1\rangle\}$ , to the next pair of states,  $\{|\phi_2\rangle, |\phi_3\rangle\}$ , are accounted for in  $\mathcal{D}_{\text{inc}}$  by an incoherent sum of dissipators,  $\kappa(\Delta_{210})\mathcal{D}[X_{210} |\phi_2\rangle \langle \phi_1|] + \kappa(\Delta_{301})\mathcal{D}[X_{301} |\phi_3\rangle \langle \phi_0|]$ . As discussed above, upward transition to states that have not yet kissed leads to tunneling across the double well potential happening here at a rate  $\propto |X_{210}|^2 + |X_{301}|^2$  given by the dark blue line in Fig. 4(b). This effect is illustrated in Fig. 5(a) which shows how the coherent state  $|\beta + \alpha\rangle$ , initially localized in one well of the metapotential, transforms under the action of this incoherent sum of dissipators, resulting in a mixture of states localized in the two wells.

After spectral kissing of  $\varepsilon_2$  and  $\varepsilon_3$ , the above two transitions coherently add contributing to  $\mathcal{D}_{\text{coh}}$  as  $\kappa(\Delta_{210})\mathcal{D}[X_{210} |\phi_2\rangle \langle \phi_1| + X_{301} |\phi_3\rangle \langle \phi_0|]$ . As illustrated in Fig. 5(b), the action of this joint jump operator on  $|\beta + \alpha\rangle$  no longer leads to delocalization across the metapotential. To understand this we express the Floquet modes  $|\phi_{2,3}\rangle$  as superpositions of states localized in each well

$$|\phi_{2,3}\rangle \simeq (\hat{D}(\beta + \alpha) |1\rangle \mp e^{i\theta'} \hat{D}(\beta - \alpha) |1\rangle)/\sqrt{2}, \quad (14)$$

where  $\hat{D}$  is the displacement operator and  $|1\rangle$  is the one-photon Fock state [20]. Using this expression to perform a similar decomposition as in Eq. (13), we find that the above dissipator generates two types of processes. First, it contributes to intrawell leakage  $|\beta \pm \alpha\rangle \rightarrow \hat{D}(\beta \pm \alpha) |1\rangle$  at a rate  $\propto |X_{210} + X_{301}|^2 \approx |X_{210}|^2 + |X_{301}|^2$ . Second, it contributes to interwell tunneling  $|\beta \pm \alpha\rangle \rightarrow \hat{D}(\beta \mp \alpha) |1\rangle$  at a rate  $\propto |X_{210} - X_{301}|^2$ . Crucially, this interwell

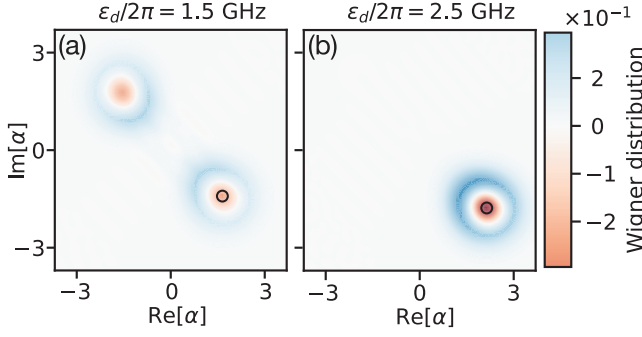


FIG. 5. Wigner distributions illustrating how the action of the dissipator affects the initially localized coherent state  $|\beta + \alpha\rangle$  (indicated by the black circle). (a) At  $\varepsilon_d/2\pi = 1.5$  GHz, before the spectral kissing, the jump operators  $\hat{L}_1 = X_{210} |\phi_2\rangle \langle \phi_1|$  and  $\hat{L}_2 = X_{301} |\phi_3\rangle \langle \phi_0|$  act incoherently. The resulting state is  $p_1 \hat{\rho}_1 + p_2 \hat{\rho}_2$ , where  $\hat{\rho}_{1,2} = \hat{L}_{1,2} |\beta + \alpha\rangle \langle \beta + \alpha| \hat{L}_{1,2}^\dagger / p_{1,2}$  and  $p_{1,2} = \langle \beta + \alpha | \hat{L}_{1,2}^\dagger \hat{L}_{1,2} | \beta + \alpha \rangle$ . The state becomes delocalized across the double-well. (b) At  $\varepsilon_d/2\pi = 2.5$  GHz, after the kissing, the jump operators interfere coherently. The resulting state is  $\hat{L} |\beta + \alpha\rangle / \sqrt{\langle \beta + \alpha | \hat{L}^\dagger \hat{L} | \beta + \alpha \rangle}$  with  $\hat{L} = \hat{L}_1 + \hat{L}_2$ , preserving localization in the original well.

transition rate is exponentially suppressed as the drive amplitude increases beyond the kissing point, as shown by the red line in Fig. 4(a), and further supported by analytical results presented in Appendix D. The intrawell leakage rate, though, is not suppressed; see the dark blue line in Fig. 4(b).

If the high-energy Floquet modes were limited to  $|\phi_2\rangle$  and  $|\phi_3\rangle$ , tunneling across the double-well barrier would remain exponentially suppressed after the first kissing event, as shown by the light blue line in Fig. 4(a). However, the master equation (7) accounts for dissipators connecting  $|\phi_{2,3}\rangle$  to higher modes, causing the above scenario of tunneling through higher levels to repeat. Before each new spectral kissing, an incoherent sum of dissipative pathways enables tunneling. After the kissing, interference between two competing transitions suppresses tunneling, leading to only intrawell leakage; see in Fig. 4(a) how further matrix-element differences become suppressed with  $\varepsilon_d$ .

#### D. Tunneling and coherence times of the Kerr-cat qubit

We now turn to the main results of this section: (1) Under the single-mode approximation of Eq. (4), the tunneling time increase in a staircase-like fashion and continues to grow with drive amplitude without saturation; and (2) the tunneling time does not coincide with the Kerr-cat coherence time  $T_Z$ , which initially increases but then decreases as the drive amplitude is further increased. Figure 6(a) shows the Kerr-cat tunneling time as a func-

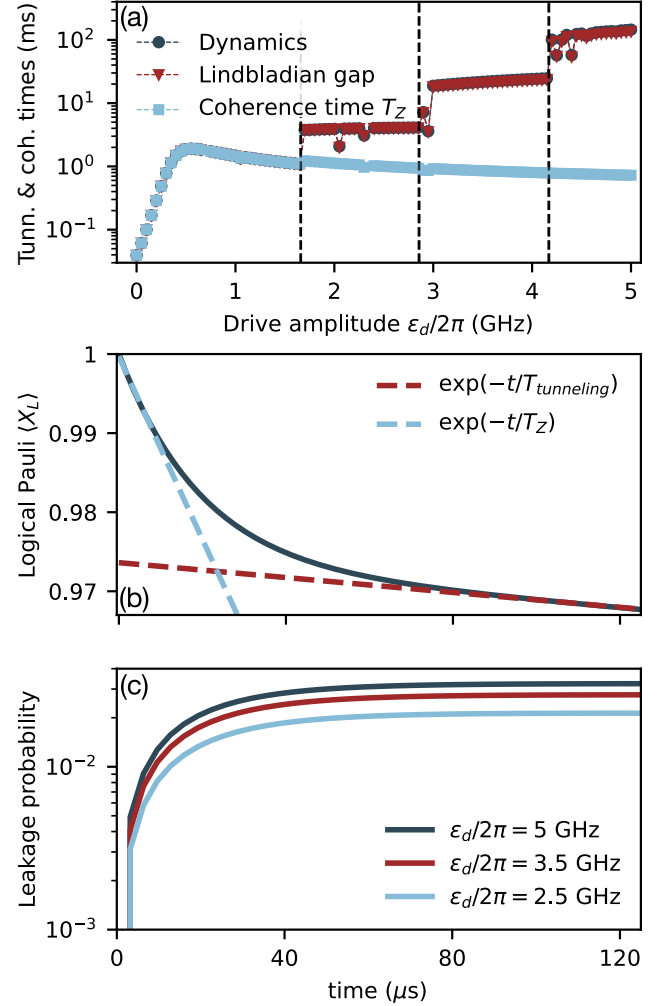


FIG. 6. (a) Tunneling time of the Kerr-cat qubit extracted from time dynamics (dark blue) and the inverse of the Lindbladian gap (red). The coherence time, defined by the initial decay of the logical Pauli operator  $\hat{X}_L = |\beta + \alpha\rangle \langle \beta + \alpha| - |\beta - \alpha\rangle \langle \beta - \alpha|$ , is shown in light blue. Dashed vertical lines mark the drive amplitudes corresponding to spectral kissing events. (b) Time evolution of the expectation value of  $\hat{X}_L$  for an initial state  $|\beta + \alpha\rangle$  at drive amplitude  $\varepsilon_d/2\pi = 3.5$  GHz. Red and light blue dashed lines indicate exponential fits at short and long times, respectively. (c) Intrawell leakage probability as a function of time for three values of drive amplitudes. System parameters are identical to those used in Fig. 3. The bath parameters are taken from Ref. [39], with  $J(\omega_d) = 796$  kHz and  $T(\omega_d) = 350$  mK; at other harmonics  $J(\omega_d/2) = 7.96$  kHz and  $T(\omega_d/2) = 50$  mK.

tion of drive amplitude, obtained from two methods: i) the discrimination of the time-evolved distribution of the coherent states  $|\beta \pm \alpha\rangle$  spanning the cat states (blue circles) and ii) the smallest gap of the Lindbladian (7) (red triangles). The agreement between these approaches is excellent.

In the first method, for each value of the drive ampli-

tude  $\varepsilon_d$ , the system is initialized in one of two coherent states,  $|\beta + \alpha\rangle$  or  $|\beta - \alpha\rangle$ , constructed from superpositions of the lowest Floquet modes  $|\phi_0\rangle$  and  $|\phi_1\rangle$ . These coherent states are then evolved under the Floquet-Markov master equation Eq. (7). At each time step, the Husimi Q distributions of these evolved states are computed and used to construct the log-likelihood function from which the assignment error of a hypothetical heterodyne measurement is evaluated. By analyzing the time dependence of the assignment error and fitting it to an exponential decay, we obtain the tunneling time. This procedure closely mirrors the experimental approach used to measure tunneling via heterodyne detection [30, 32–34]; see Appendix C for details. In the second method, the tunneling time is obtained as the inverse of the Lindbladian gap, which defines the slowest relaxation rate in the system. It is obtained from the diagonalization of the Lindbladian on the right-hand side of Eq. (7) in the Floquet-mode basis.

In agreement with experimental observations [30, 32], we find in Fig. 6(a) that the tunneling time increases in a staircase-like manner with the drive amplitude, with each plateau ending precisely at a spectral kissing point (vertical dashed lines). We also observe occasional very sharp features in some of the plateaus. These features originate from accidental degeneracies in the Floquet spectrum—for instance, near  $\varepsilon_d/2\pi \approx 4.4$  GHz, the transition frequency  $\Delta_{6,12,k}$  coincides with the degenerate pairs  $\Delta_{2,6,k}$  and  $\Delta_{3,7,k}$ , which leads momentarily to enhanced leakage. Importantly, however, there is no hybridization of the Floquet modes, as the quasienergies involved do not cross each other. As a result, the impact of these accidental resonances on the tunneling time is minimal.

Importantly, these results do not rely on a perturbative expansion in the nonlinearity or the drive strength. Rather, it follows from minimal assumptions: the single-mode approximation of the system Hamiltonian of Eq. (4) and the standard approximations of weak, short-time correlated dissipation. Interestingly, the staircase behavior can also be reproduced within a perturbative framework, based on an expansion of the cosine nonlinearity and an effective Lindbladian derived by retaining terms beyond the standard rotating-wave approximation [39]. However, both approaches—the exact single-mode treatment presented here and the perturbative analysis—fail to capture the sharp decrease in tunneling time observed at large drive amplitudes.

We also find that the tunneling time differs dramatically from the coherence time  $T_Z$  of the Kerr-cat, as defined by the decay time of the expectation value of the logical Pauli operator  $\hat{X}_L = |\beta + \alpha\rangle\langle\beta + \alpha| - |\beta - \alpha\rangle\langle\beta - \alpha|$  at short times; see the light blue squares in Fig. 6(a). Indeed, the latter quantity rapidly reaches a maximum value and does not show the characteristic staircase behavior of the tunneling time. As shown in Fig. 6(b), the expectation value of  $\hat{X}_L$  exhibits a two-stage decay: an initial drop over a timescale  $T_Z$  (light blue dashed line), followed by a much slower decay gov-

erned by the tunneling time (red dashed line). These two timescales coincide at low drive amplitude—specifically before the first spectral kissing, see Fig. 6(a) where  $T_Z$  matches the tunneling time before the first vertical dashed line—but begin to differ as the drive amplitude increases beyond that point. This difference arises because, although interwell tunneling is strongly suppressed as  $\varepsilon_d$  increases, the *intrawell leakage* rate continues to grow, reducing the occupation probability of the coherent states. This is illustrated in Fig. 6(c), which shows the intrawell leakage probability as a function of time for three values of drive amplitude. Here we define the leakage probability as  $p_{\pm} - p_{\beta\pm\alpha}$ , where  $p_{\beta\pm\alpha}$  is the probability of occupying the coherent state  $|\beta \pm \alpha\rangle$ , and  $p_{\pm}$  denotes the probability of being on the side of phase space where the coherent state  $|\beta \pm \alpha\rangle$  is localized. Intrawell leakage accumulates over time and saturates at a value that increases with drive amplitude. Further details about this leakage probability can be found in Appendix C.

Finally, we note that the absence of any breakdown in the resulting tunneling time at large drive amplitudes, despite the minimal assumptions used here, suggests a limitation in one of our underlying approximations. In Sects. III and IV, we show—using the same general formalism presented in this section—how the multimode nature of the circuit leads to a breakdown of the tunneling time at moderate photon number.

## E. Heating and drive-induced dissipation

In Sec. II C, we have discussed processes associated with the absorption of a photon at  $\omega_d/2$  from the bath and contributing to interwell tunneling and intrawell leakage, such as  $|X_{210}|^2$  and  $|X_{301}|^2$ . Here, we describe other heating processes that limit the coherence and tunneling times of the Kerr-cat qubit and explain the roles of the spectral density and the effective temperature.

In addition to the processes discussed above, the environment can induce leakage near  $\omega_d$ , where the spectral density  $J(\omega)$  peaks—see Fig. 2(d)—despite smaller associated matrix elements. In particular, the matrix elements  $X_{20\pm 1}$  and  $X_{31\pm 1}$  correspond to transitions that connect states of the same parity, such as  $|\phi_0\rangle \rightarrow |\phi_2\rangle$  and  $|\phi_1\rangle \rightarrow |\phi_3\rangle$ . Before the first spectral kissing, these transitions contribute to tunneling with a total rate given by

$$\frac{1}{2}\kappa(\omega_d)(|X_{201}|^2 + |X_{311}|^2) + \frac{1}{2}\kappa(-\omega_d)(|X_{20-1}|^2 + |X_{31-1}|^2). \quad (15)$$

The first term corresponds to photon absorption from the bath at frequency  $\omega_d$  and is present even at zero drive amplitude. Indeed, in the limit  $\varepsilon_d = 0$ , the associated Floquet matrix elements reduce to the charge matrix elements  $\langle 0|\hat{n}|2\rangle/n_{\text{zpf}}$  and  $\langle 1|\hat{n}|3\rangle/n_{\text{zpf}}$  between bare SNAIL states  $|i\rangle$ . These matrix elements are small but nonzero—of order  $10^{-2}$  for the parameters used here—reflecting the fact that the double-SNAIL Hamiltonian  $\hat{H}_s$  does

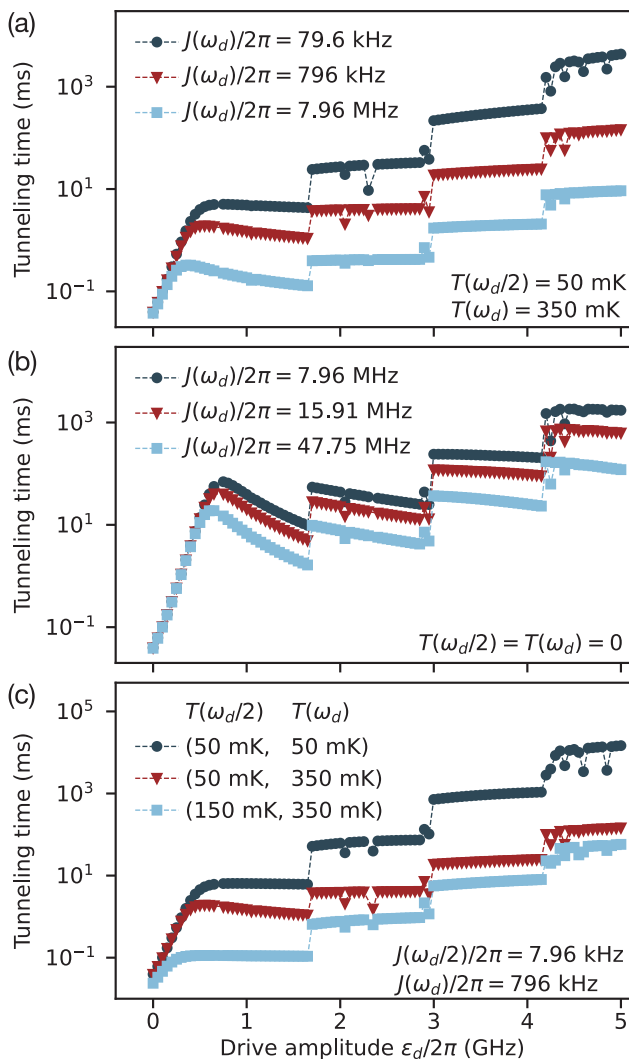


FIG. 7. Tunneling time as a function of the drive amplitude for different bath spectral densities and temperatures. (a) Fixed temperature with three different spectral densities  $J(\omega)$ . (b) Zero temperature with three different spectral densities  $J(\omega)$ . (c) Fixed  $J(\omega_d)$  with three combinations of bath temperatures  $T(\omega_d/2)$  and  $T(\omega_d)$ . The specific values of  $J(\omega)$  and  $T(\omega)$  are indicated in the plots.

not have parity symmetry. Increasing the drive amplitude, the matrix elements  $|X_{201}|^2 + |X_{311}|^2$  are further enhanced; see the blue dashed line in Fig. 4(b). This is supported by analytical results presented in Appendix D. Importantly, this leakage mechanism is absent in circuit implementations that preserve parity symmetry—i.e., those for which the Hamiltonian is invariant under  $\hat{n} \rightarrow -\hat{n}$  and  $\hat{\varphi} \rightarrow -\hat{\varphi}$ —such as symmetric SQUID-based designs [11, 70].

On the other hand, the second term of Eq. (15) corresponds to a more subtle drive-induced emission to the bath at frequency  $\omega_d$  which persists at zero temperature.

As shown by the dotted yellow and brown lines in Fig. 4(b), the corresponding matrix elements vanish as

$\varepsilon_d \rightarrow 0$  but grow by several orders of magnitude as  $\varepsilon_d$  increases. Perturbative expressions for these rates are given in Appendix D. This type of drive-induced emission to the bath occurring concurrently with qubit leakage has been shown to be a limiting factor for dispersive readout in the high-frequency regime [51, 52].

For the bath parameters used in Fig. 6—taken from Ref. [39]—we find  $\kappa(\omega_d)/\kappa(\omega_d/2) \sim 10^4$ . As a result, we find that

$$\kappa(\omega_d)(|X_{201}|^2 + |X_{311}|^2) \sim \kappa(\omega_d/2)(|X_{210}|^2 + |X_{301}|^2),$$

even though  $|X_{201}|^2 + |X_{311}|^2 \gg |X_{210}|^2 + |X_{301}|^2$ ; see Figure 4. Moreover, these two rates are much larger than  $\kappa(-\omega_d)(|X_{20-1}|^2 + |X_{31-1}|^2)$ , indicating that drive-induced processes are negligible for this choice of parameters. Importantly, these different rates depend sensitively on the specific form of the spectral density and the bath temperature at the relevant frequencies. For instance, in the case of a flat spectral density and a constant temperature over the whole frequency range, leakage would be dominated by the heating process at  $\omega_d/2$  if  $T \gtrsim 20$  mK. In contrast, at lower temperatures, the dominant contribution would come from drive-assisted processes.

As an illustration, Fig. 7 shows the tunneling time as a function of drive amplitude, using the same system parameters as in Fig. 6, but with different values of the bath spectral density  $J(\omega_d)$  and temperatures  $T(\omega_d)$  and  $T(\omega_d/2)$ . First, we find that both the overall scale of the tunneling time and the heights of its staircase-like features are highly sensitive to these parameters: decreasing either  $J(\omega_d)$  or the temperature increases the tunneling time, in agreement with the above discussion. In panel (a), we vary  $J(\omega_d)$  while keeping  $J(\omega_d/2)$  and both temperatures fixed. As a result, we observe a transition from a regime dominated by heating at  $\omega_d$  (light blue) to one dominated by heating at  $\omega_d/2$  (dark blue). The red curve represents the intermediate regime, previously discussed, where both channels contribute comparably. A key signature of  $\omega_d$ -induced heating is the gradual decrease of the first plateau, rather than a flat one. This behavior arises because the corresponding matrix elements  $|X_{201}|^2 + |X_{311}|^2$  grow with drive amplitude, as seen in the blue dashed line of Fig. 4(b). In panel (b), we consider the zero-temperature limit with  $T(\omega) = 0$  for all frequencies such that that drive-induced processes constitute the sole heating mechanism. In this regime, the plateaus between kissing events have a steeper decline with increasing drive amplitude due to the strong enhancement of the relevant matrix elements ( $|X_{20-1}|^2 + |X_{31-1}|^2$  and  $|X_{42-1}|^2 + |X_{53-1}|^2$ ) with drive amplitude, as shown by the orange and brown dotted lines in Fig. 4(b). Panel (c) shows a similar effect as in (a), but now by varying the temperatures at  $\omega_d$  and  $\omega_d/2$  while keeping the spectral density fixed. The dark and light blue curves again highlight regimes where heating at  $\omega_d/2$  dominates, while the red curve is reproduced from (a) for comparison.

### III. BUFFER MODE

The single-mode approximation of Eq. (4), when combined with a Floquet-Markov treatment and the full nonlinear SNAIL potential, captures many key features of the Kerr-cat qubit. In particular, it reproduces spectral kissing and the staircase-like growth of the tunneling time with increasing drive amplitude. However, it fails to capture the breakdown of this staircase structure observed at large drive amplitudes. A key limitation is the absence of spectral resonances within the single-mode spectrum that could mediate leakage out of the cat manifold. These resonances have been identified in previous work as the main mechanism behind ionization in highly-excited hydrogen atoms [42] and in driven superconducting circuits [43, 44, 46–50, 62, 71, 72]. As a result, the one-mode model does not reproduce the experimentally observed sudden decrease in tunneling time.

To address this limitation, we now reintegrate the buffer mode into our description of the system and investigate its impact on the Kerr-cat qubit. Our starting point is the exact displaced-frame Hamiltonian of Eq. (3), which includes the interaction between the cat mode and the buffer. For experimentally relevant parameters—specifically, a buffer-drive detuning of  $|\Delta_{bd}|/2\pi = |\omega_b - \omega_d|/2\pi \approx 285$  MHz and a coupling strength of  $g/2\pi \approx 100$  MHz—this interaction leads to a dispersive shift of approximately 2.56 kHz between the buffer and the double-SNAILs oscillator [30, 31, 33]. As we show below, this additional degree of freedom introduces the resonant processes missing from the single-mode model and results in the breakdown of the staircase behavior.

#### A. Impact of the buffer mode on the Floquet spectrum

The analysis follows the same steps as above, with the particularity that special care must be taken in identifying the dressed states of the joint SNAIL–buffer system. To do so, we begin by diagonalizing the undriven Hamiltonian,

$$\hat{H}_{sb} = \hat{H}_s + \omega_b \hat{a}_b^\dagger \hat{a}_b + ig\hat{n}(\hat{a}_b^\dagger - \hat{a}_b), \quad (16)$$

yielding a set of dressed eigenstates  $\{|\lambda\rangle\}$  with corresponding dressed energies  $\{E_\lambda\}$ . Following Ref. [45], we label the spectrum by first identifying the dressed states  $\{|i_s, 0_b\rangle\}$  with  $i_s$  excitation of the SNAIL and zero excitation of the buffer mode by comparison to the bare states with no buffer excitation. We then apply  $\hat{a}_b^\dagger$  to each of these dressed states to generate candidates for the  $\{|i_s, 1_b\rangle\}$  states, selecting those among the remaining  $\{|\lambda\rangle\}$  with the largest overlaps. This iterative process is repeated to construct and label the higher-excitation states  $\{|i_s, j_b\rangle\}$ . As in the previous section, we truncate the Hilbert space to include 160 levels in the double-SNAIL mode and up to five excitations in the buffer mode.

Working in the displaced frame, we then include the drive on the double-SNAILs mode as in Eq. (3) and obtain the Floquet spectrum as a function of the drive amplitude following the procedure discussed in Sec. II using a step-size increment of  $\delta\varepsilon_d/2\pi = 2.5$  MHz in the tracking of the spectrum; see Ref. [47] for a discussion of the choice of increment  $\delta\varepsilon_d$ . In this extended system, the cat states correspond to the Floquet modes  $|\phi_{0_s, 0_b}\rangle$  and  $|\phi_{1_s, 0_b}\rangle$ . To facilitate comparison with the single-mode approximation, we show in Fig. 8(a) the Floquet spectrum (folded at  $\omega_d/2$ ) for the lowest modes with zero buffer excitation (full lines), alongside three relevant modes with one buffer excitation (dashed lines).

As in the single-mode approximation, for drive amplitudes up to  $\varepsilon_d/2\pi \approx 3.4$  GHz we recover the spectral kissings involving, for example, the quasienergy pairs  $(\epsilon_{2_s, 0_b}, \epsilon_{3_s, 0_b})$  and  $(\epsilon_{4_s, 0_b}, \epsilon_{5_s, 0_b})$ ; see the circles. However, avoided crossings emerge between low-energy quasienergies without buffer-mode excitation and higher-energy states involving one buffer-mode excitation. These features are marked by squares in panel (a) and shown in detail in the zoomed-in view of panel (b). The first anticrossing is between  $\epsilon_{7_s, 0_b}$  and  $\epsilon_{17_s, 1_b}$  at  $\varepsilon_d/2\pi \approx 3.4$  GHz—corresponding to  $\langle\phi_{0(1)}|\hat{a}^\dagger\hat{a}|\phi_{0(1)}\rangle \approx 12$  photons in the cat manifold. Similar avoided crossings occur between  $\epsilon_{5_s, 0_b}$  and  $\epsilon_{15_s, 1_b}$  at  $\varepsilon_d/2\pi \approx 4.29$  GHz, and between  $\epsilon_{2_s, 0_b}$  and  $\epsilon_{12_s, 1_b}$  at  $\varepsilon_d/2\pi \approx 4.81$  GHz. Importantly, each of these features interrupts a spectral kissing.

Crucially, the three avoided crossings highlighted above are not the only ones present, but merely those resolved with the finite step size  $\delta\varepsilon$  of drive amplitude used in our Floquet spectrum tracking. Indeed, in the absence of any selection rule, as is the case here, there is finite coupling between all pairs of quasienergies, such that crossings are generically replaced by avoided crossings. Thus, when the quasienergies indicated by the gray dashed lines in Fig. 8(a) intersect with lower-lying quasienergies, they in fact form avoided crossings which are not resolved here. These involve hybridization between higher-lying states—such as  $|13_s, 1_b\rangle$ ,  $|14_s, 1_b\rangle$ , and  $|16_s, 1_b\rangle$ —and lower-lying states involved in spectral kissing, and they occur densely within the drive range  $\varepsilon_d/2\pi \in [2.8, 5]$  GHz. While their splitting are small, on the order of  $\sim 10$  kHz as in those shown in Fig. 8(c), their presence nonetheless has significant consequences on the tunneling time, as further discussed in the next subsection.

These avoided crossings can be resolved despite their small gap size because they are wide: the involved quasienergies remain nearly parallel over a broad range of drive amplitudes, so their relative separation evolves slowly compared to the size of the step-size increment  $\delta\varepsilon_d/2\pi = 2.5$  MHz. As a result, the modes hybridize appreciably over an extended range of drive amplitude, even if the eigenstate labels do not swap at the avoided crossing. Further reducing the step-size increment in the tracking, although possible, is not necessary for resolving these features, and we avoid it due to its computational

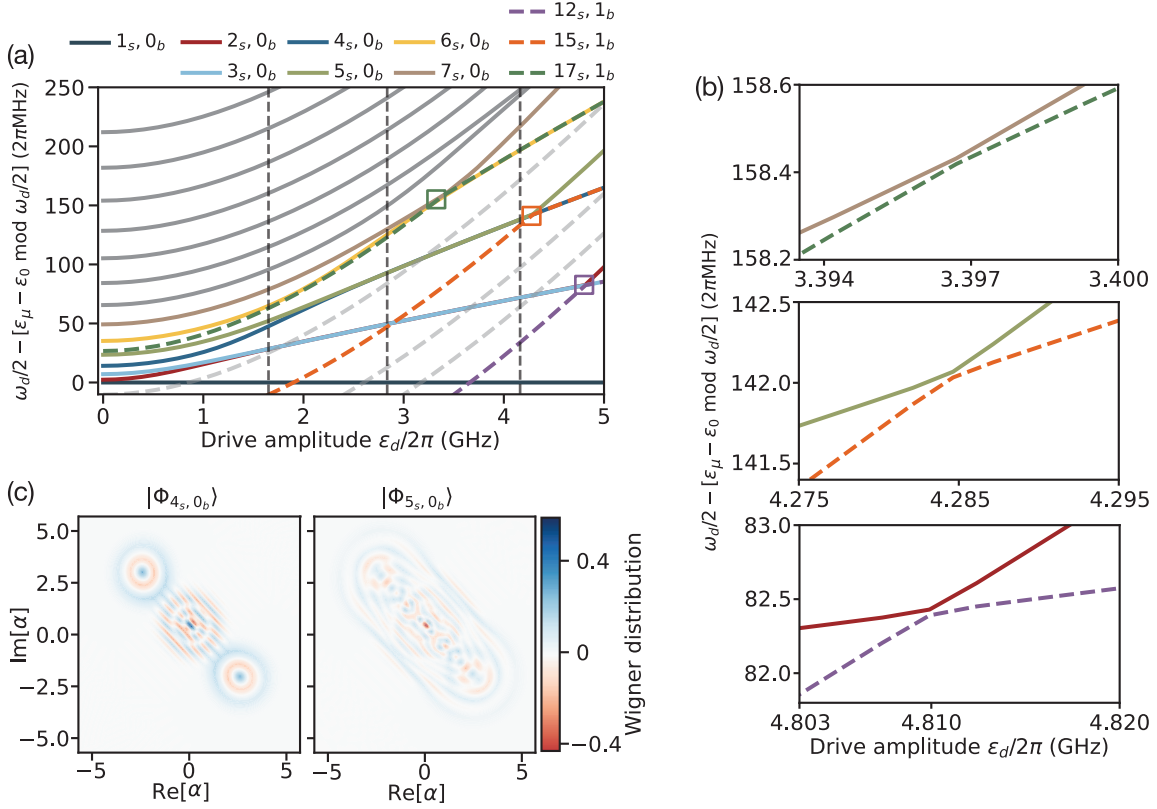


FIG. 8. (a) Spectral kissing of the quasienergies in the presence of the buffer mode. Solid lines indicate quasienergies without buffer excitation, while dashed lines correspond to modes with one buffer excitation. (b) Detailed view of three avoided crossings highlighted by squares in panel (a) and which interrupt the spectral kissing of low-lying quasienergies. (c) Wigner functions of the modes  $|\phi_{4s, 0_b}\rangle$  (left) and  $|\phi_{5s, 0_b}\rangle$  (right) near the avoided crossing at  $\epsilon_d/2\pi = 4.81$  GHz.

cost.

The importance of these avoided crossings is that at any one of them, no superposition of the Floquet modes involved in kissings can be localized within a single well of the Kerr-cat metapotential. This is illustrated in Fig. 8(c) which shows the Wigner distributions of the Floquet modes  $|\phi_{4s, 0_b}\rangle$  and  $|\phi_{5s, 0_b}\rangle$  at  $\epsilon_d/2\pi = 4.81$  GHz corresponding to the avoided crossing between  $\epsilon_{5s, 0_b}$  and  $\epsilon_{15s, 1_b}$ . Prior to the avoided crossing,  $|\phi_{5s, 0_b}\rangle$  is approximately related to  $|\phi_{4s, 0_b}\rangle$  by a displaced parity transformation; as a result, their superpositions yield states of the form  $\hat{D}(\beta \pm \alpha)|n=2\rangle$ , which are localized in a single well [20]. At the avoided crossing, however,  $|\phi_{5s, 0_b}\rangle$  becomes significantly hybridized with a higher-energy mode—as manifested by its Wigner distribution—and can no longer be combined with  $|\phi_{4s, 0_b}\rangle$  to produce a well-localized state.

The avoided crossings, along with the resulting successive interruption of spectral kissing, are the result of the ac-Stark shifts of the energy levels as well as the moderate detuning between the buffer mode and the drive frequency. To illustrate this, we focus on the avoided crossing between  $\epsilon_{7s, 0_b}$  and  $\epsilon_{17s, 1_b}$ . In the absence of a drive, the energy difference between the corresponding

dressed states is approximately

$$E_{17s, 1_b} - E_{7s, 0_b} \approx 6\omega_d + \Delta_{bd} - (17 \cdot 16 - 7 \cdot 6)K, \quad (17)$$

where the last term arises from the self-Kerr nonlinearity which is here  $K/2\pi = 1.18$  MHz. This expression shows that, in the presence of a drive, these two states can become resonant (modulo  $\omega_d$ ) if the ac-Stark shift is strong enough to compensate for the detuning  $\Delta_{bd} - (17 \cdot 16 - 7 \cdot 6)K$ . This situation is likely to occur for this or other transitions when  $\Delta_{bd} > 0$ , as considered here and as is the case in recent experiments [30, 34]. This is because the drive induces a negative ac-Stark shift to the transition from  $E_{i_s, 0_b}$  to  $E_{j_s, 1_b}$  for  $j_s > i_s$ , leading to a multiphoton resonance condition whenever  $\Delta_{bd} \gtrsim [j_s(j_s - 1) - i_s(i_s - 1)]K$ . For the range of drive amplitudes considered here, detunings  $\Delta_{bd} - [j_s(j_s - 1) - i_s(i_s - 1)]K$  of  $\sim 2\pi \times 100$  MHz or less are problematic, as the ac-Stark shift can bridge that gap at moderate drive amplitudes. In the single-mode case, these types of resonances cannot occur as energy differences like  $E_{17s} - E_{7s} \approx 5\omega_d - (17 \cdot 16 - 7 \cdot 6)K$  cannot be compensated by the negative shift induced by the drive. The preceding discussion immediately suggests that no avoided crossings would be found in our range of drive amplitudes when  $\Delta_{bd} < 0$ . This simple strategy is con-

firmed in Appendix E2 to save the Kerr-cat qubit from crashing.

Moreover, because a small Kerr implies a slowly increasing ac-Stark shift with growing  $\varepsilon_d$ , the near-resonance condition can persist over a wide range of drive amplitudes. As a result, even a weak dispersive interaction can lead to strong hybridization between these Floquet modes. A similar argument explains the other two avoided crossings highlighted in Fig. 8. Importantly, capturing this hybridization accurately would be difficult—if not impossible—using a perturbative expansion of the nonlinearity; see also Refs. [42, 47]. In Appendix E1, we show that the leading-order process responsible for the coupling between  $|\phi_{7s,0b}\rangle$  and  $|\phi_{17s,1b}\rangle$  arises only at seventh order in the expansion of the nonlinear potential around its minimum.

These unwanted resonances between low-energy and high-energy Floquet modes underscore the importance of considering the joint dynamics of the double-SNAIL and the buffer mode, highlighting the limitations of the single-mode approximation. As we show below, the hybridization of the SNAIL mode with the buffer mode impacts the tunneling time of the Kerr-cat qubit.

## B. Impact of the buffer mode on tunneling time

We extend the Floquet-Markov formalism introduced in Sec. II to account for the fact that the SNAILS and the buffer mode are coupled to distinct environments. The master equation now includes two types of dissipative channels, associated with the matrix elements of the SNAIL charge operator

$$X_{\mu\nu k}^s = \frac{1}{T} \int_0^T e^{-ik\omega t} \langle \phi_\mu(t) | i(\hat{a}_b^\dagger - \hat{a}_b) | \phi_\nu(t) \rangle dt, \quad (18)$$

and the buffer charge operator

$$X_{\mu\nu k}^b = \frac{1}{T} \int_0^T e^{-ik\omega t} \langle \phi_\mu(t) | i(\hat{a}_b^\dagger - \hat{a}_b) | \phi_\nu(t) \rangle dt. \quad (19)$$

In these expressions, each index  $\mu$  and  $\nu$  labels a pair  $(i_s, j_b)$  of SNAIL and buffer excitation. The first type of matrix elements,  $X_{\mu\nu k}^s$ , describes dissipation due to the intrinsic bath of the double-SNAIL accounting, e.g., for dielectric losses. Importantly, in contrast to the similar-looking expression Eq. (10) in the single-mode approximation, this bath is not filtered by the buffer mode. We therefore consider a flat spectral density  $J_s(\omega) = \theta(\omega) \times 7.98$  kHz and a single effective temperature of  $T_s = 50$  mK. The second type of matrix elements,  $X_{\mu\nu k}^b$ , describes coupling of the buffer mode to its environment, dominated by the coupling to the drive line. This bath is likewise assumed to have a flat spectral density  $J_b(\omega) = \theta(\omega) \times 798$  kHz and a constant effective

temperature of  $T_b = 350$  mK. The specific numerical values for the spectral densities and temperatures are chosen so that the dissipative dynamics considered in Sec. II are recovered in the single-mode approximation.

With these definitions in hand, we now follow the approach discussed in Sec. IID and compute the tunneling time as a function of drive amplitude from the assignment error, as shown in Fig. 9(a). For drive amplitudes below  $\varepsilon_d/2\pi \approx 2.89$  GHz, the tunneling time exhibits a staircase-like increase thanks to the spectral kissing of the lowest-lying quasienergies and the induced interference of dissipative processes, just like in the case of the semiclassical treatment of the buffer mode in Sec. II. For larger drive amplitudes, where the spectral kissing is interrupted by avoided crossings, the tunneling time is considerably affected. Figure 9(b) shows the tunneling time in the range  $\varepsilon_d/2\pi \in (2.75, 5)$  GHz. This is accompanied in panel (c) by the fidelity of the Floquet tracking ( $|\langle \phi_\mu[\varepsilon_d] | \phi_\mu[\varepsilon_d + \delta\varepsilon_d] \rangle|^2$ ), which measures the squared overlap between each Floquet mode before and after each drive increment, and in panel (d) by representative Floquet matrix elements  $|X_{\mu\nu k}^s| = |X_{\mu\nu k}^s|$ . While we focus here on matrix elements of the first type, we note that the second type,  $X_{\mu\nu k}^b$ , exhibits similar features.

At  $\varepsilon_d/2\pi \approx 2.9$  GHz, a sharp dip is observed in the tunneling time. As shown in panel (c), this coincides with a sudden drop in the tracking overlap of  $|\phi_{3s,0b}\rangle$ , which hybridizes with  $|\phi_{15s,1b}\rangle$ . Consequently, the matrix elements connecting  $|\phi_{3s,0b}\rangle$  to higher-energy modes—dark-blue, light-blue, and solid-blue lines in Fig. 9(c)—rise sharply. Although hybridization between these states is relatively weak at this particular value of  $\varepsilon_d$ —on the order of 2%, as shown by the blue line in Fig. 9(c)—it is sufficient to disrupt the staircase-like increase of the tunneling time because the transition between the modes  $|\phi_{2s,0b}\rangle$  and  $|\phi_{3s,0b}\rangle$  is no longer suppressed, as the hybridization interrupts the coherent interference of jump operators shown, e.g., in Fig. 5. Moreover, there is a significant increase in the transition rates to high-energy modes. As shown in panel (d), the Floquet matrix elements  $|X_{\mu,\beta,k}|$  between  $(3s, 0b)$  and  $(12s, 1b)$  (dark blue line),  $(14s, 1b)$  (red and light blue lines), and  $(16s, 1b)$  (blue line) increase by several orders of magnitude.

Above  $\varepsilon_d/2\pi \approx 2.9$  GHz, the tunneling time exhibits a sharp increase followed by a new plateau, due to spectral kissing between  $\epsilon_{4s,0b}$  and  $\epsilon_{5s,0b}$ —a behavior reminiscent of the single-mode case. However, this plateau is interrupted several times whenever one of the low-lying modes—namely,  $|0s, 0b\rangle$  through  $|5s, 0b\rangle$ —hybridizes with higher-energy states. For instance, at  $\varepsilon_d/2\pi \approx 3.19$  GHz the mode  $|\phi_{4s,0b}\rangle$  hybridizes with  $|\phi_{16s,1b}\rangle$  leading to the dip in the tracking fidelity of the former, as shown by the blue curve of Fig. 9(c). This hybridization not only disrupts the suppression of tunneling between  $|\phi_{4s,0b}\rangle$  and  $|\phi_{5s,0b}\rangle$ , but also enhances matrix elements connecting  $|\phi_{4s,0b}\rangle$  to high-energy modes, as shown by the yellow and brown curves in Fig. 9(d), ultimately resulting in a pronounced drop in tunneling

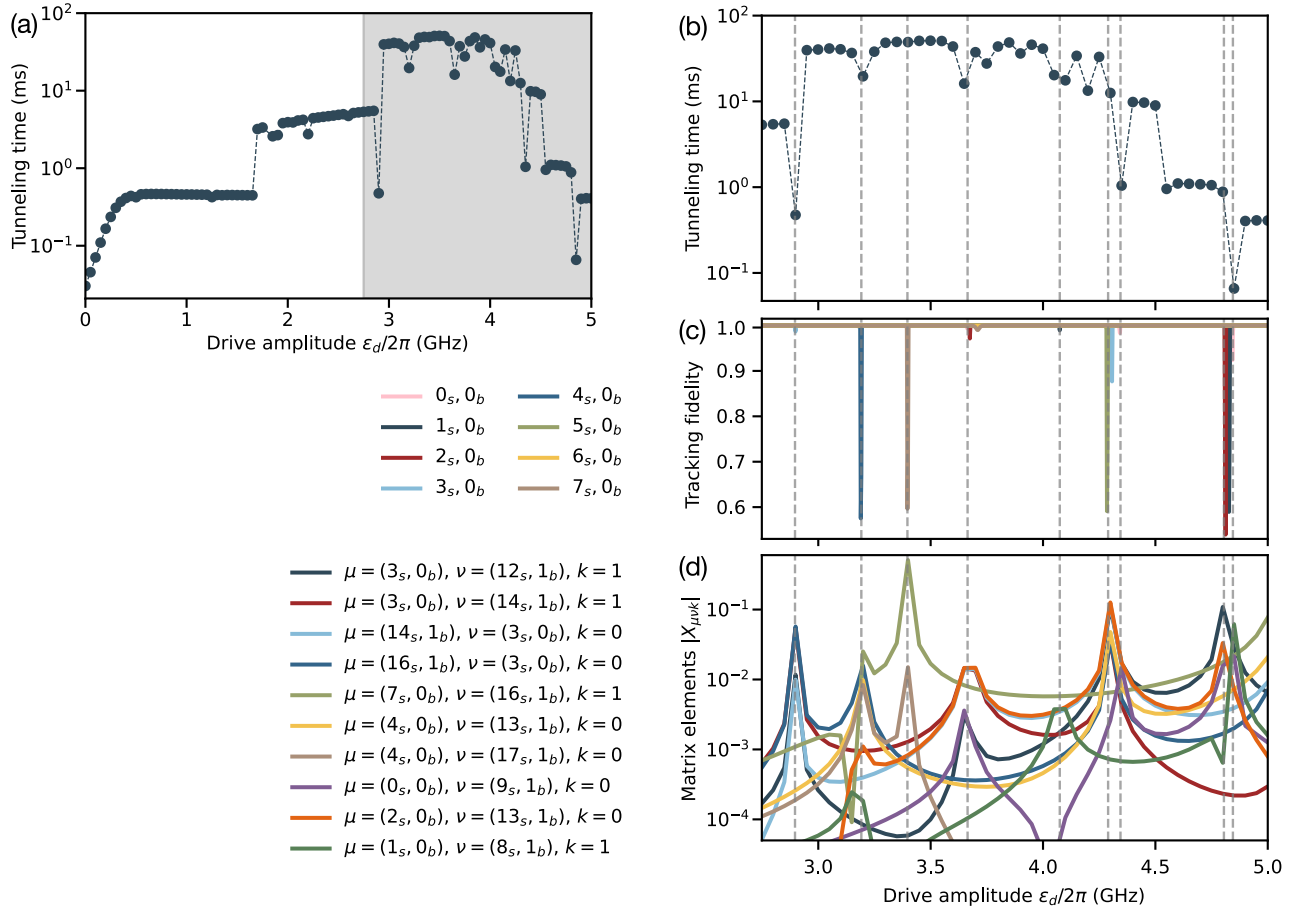


FIG. 9. (a) Tunneling time as a function of drive amplitude in the presence of the buffer mode. (b) Same as panel (a) in the reduced range  $\epsilon_d/2\pi \in (2.75, 5)$  GHz corresponding to cat states approximately 10 to 17 photons. See the legend on the left of the panel. (c) Fidelity of Floquet tracking,  $|\langle \phi_\mu[\epsilon_d] | \phi_\mu[\epsilon_d + \delta\epsilon_d] \rangle|^2$ . Drops in fidelity (highlighted by dashed lines) indicate the presence of resonances. (d) Representative Floquet matrix elements  $|X_{\mu\nu k}^s|$  as a function of the drive amplitude. The drops in the tracking fidelity coincide with resonant enhancements in matrix elements connecting low-lying modes to highly excited states, leading to the observed dips in tunneling time. See the legend on the left of the panel.

time.

Interestingly, the hybridization between  $|\phi_{7_s, 0_b}\rangle$  and  $|\phi_{17_s, 1_b}\rangle$  discussed in Sec. III A and highlighted here by the large dip in tracking fidelity (brown curve) in Fig. 9(c) does not lead to a sharp drop of the tunneling time since the quasienergies  $\epsilon_{7_s, 0_b}$  and  $\epsilon_{8_s, 0_b}$  have not yet kissed at  $\epsilon_d/2\pi \approx 3.4$  GHz. As a result, leakage to these states limits the tunneling time independently of their hybridization with other higher-energy modes.

Subsequent dips in tunneling time are caused by further resonances, including hybridizations between  $|\phi_{2_s, 0_b}\rangle$  and  $|\phi_{14_s, 1_b}\rangle$ , and between  $|3_s, 0_b\rangle$  and  $|\phi_{13_s, 1_b}\rangle$ . Beyond  $\epsilon_d/2\pi \approx 4.3$  GHz, these hybridizations become sufficiently strong—as illustrated by the yellow, dark blue, light blue, and red curves in Fig. 9(c), and the corresponding matrix element enhancements in Fig. 9(d)—to successively erode the staircase-like growth in tunneling time.

The overall decrease in tunneling time—punctuated by sharp dips—as a function of drive amplitude be-

yond a certain threshold was experimentally observed in Ref. [34], but its origin has remained an open question until now. Our results suggest that the cause of this observation is the same type of multiphoton resonance that leads to ionization of the hydrogen atom and the transmon qubit.

#### IV. SNAIL ARRAY MODES

In the previous section, we demonstrated that including the buffer mode in the circuit description led to a breakdown of the staircase pattern of the cat's tunneling time with increasing drive amplitude. In this section, we explore the role of internal degrees of freedom of the SNAIL circuit that we have dropped in the single-phase approximation of Eq. (5). These are high-frequency collective modes of the double SNAIL which we have so far implicitly assumed to remain in their ground state. In the context of fluxonium qubit readout, similar array modes

have been theoretically shown to give rise to additional multiphoton resonances involving excitations of the array and to lower the onset of measurement-induced transitions [72]. Furthermore, once populated, these modes contribute to dephasing over long timescales [61, 72], something which can significantly degrade the coherence time of the Kerr-cat qubit [36, 73]. Here, we show that although the array modes can in principle lead to multiphoton resonances and reduction of the coherence time to those induced by the buffer mode, under the parameters considered here, the presence of these modes does not lead to detrimental resonances at large drive amplitudes, and, therefore, does not lead to a reduction of the tunneling time. Moreover, these resonances mainly arise from a quadratic coupling induced by ground capacitance, which can be carefully engineered to remain negligible.

In the double-SNAIL circuit of Fig. 2(a) there are six interacting array collective modes. The lowest-energy mode corresponds to the one retained in the single-phase approximation of Eq. (5). Expressed in terms of the reduced fluxes across the six large junctions of the two SNAILS,  $\{\theta_j\}_{j=1}^6$ , the phase variable of this mode is given by  $\varphi = \sum_{j=1}^6 \theta_j$ , and we refer to it as the symmetric mode. The remaining five collective modes are nonlinear oscillators with fundamental frequencies around the plasma frequency of the large junctions,  $\sqrt{8E_{C_j}E_J}$ , which is much higher than the frequency  $\omega_{01}/2\pi \simeq 6.094$  GHz of the symmetric mode [60]. Owing to this large detuning and typically weak coupling, they generally interact with the symmetric mode only dispersively [60, 61, 72].

However, one of these modes stands out due to its comparatively lower plasma frequency and significantly stronger charge coupling to the symmetric mode [60, 61, 72]. To keep the analysis tractable while capturing the dominant effect, we retain only this mode. Its phase coordinate is defined in terms of the reduced fluxes across the large junctions as  $\varphi_- = \theta_1 + \theta_2 + \theta_3 - (\theta_4 + \theta_5 + \theta_6)$  and changes sign under exchange of the two SNAILS; accordingly, we call it the antisymmetric mode. The Hamiltonian describing the coupled symmetric and antisymmetric modes reads

$$\begin{aligned} \hat{H}_{sa} = & 4E_C \hat{n}^2 + 4\beta E_C \hat{n}_-^2 + g\hat{n}\hat{n}_- \\ & - 6E_J \cos\left(\frac{\hat{\varphi}}{6}\right) \cos\left(\frac{\hat{\varphi}_-}{6}\right) \\ & - 2\alpha E_J \cos\left(\frac{\hat{\varphi}}{2} + \varphi_x\right) \cos\left(\frac{\hat{\varphi}_-}{2}\right), \end{aligned} \quad (20)$$

where  $\beta$  is a factor relating the two capacitive energies. The two modes are coupled both through the cosine nonlinearities and via the quadratic term  $g\hat{n}\hat{n}_-$ , which arises from stray ground capacitances in the array; see Appendix F for details.

In the presence of a drive, whenever the antisymmetric-mode frequency lies near an integer multiple of the drive frequency, the Hamiltonian  $\hat{H}_{sa}$  can lead to similar mul-

tiphoton processes than those in the case of the buffer mode that disrupt the spectral kissing and the coherence of the Kerr-cat qubit. Indeed,  $\hat{H}_{sa}$  can be rewritten as

$$\begin{aligned} \hat{H}_{sa} = & 4E_C \hat{n}^2 + 4\beta E_C \hat{n}_-^2 + \frac{E_{J,-}}{2} \hat{\varphi}_-^2 + g\hat{n}\hat{n}_- \\ & - 6E_J \cos\left(\frac{\hat{\varphi}}{6}\right) - 2\alpha E_J \cos\left(\frac{\hat{\varphi}}{2} + \varphi_x\right) \\ & + \hat{H}_{\text{nl},-} + \hat{H}_{\text{nl. coupl.}} \end{aligned} \quad (21)$$

This Hamiltonian has the same form as in the buffer-mode case except for the nonlinear interaction of the extra mode  $\hat{H}_{\text{nl},-}$ , which does not play an important role, and a weak nonlinear coupling  $\hat{H}_{\text{nl. coupl.}}$ . Here we have introduced the effective Josephson energy of the antisymmetric mode

$$\begin{aligned} E_{J,-} = & E_J \left[ \frac{1}{6} \cos\left(\frac{\varphi_{\min}}{6}\right) + \frac{\alpha}{2} \cos\left(\frac{\varphi_{\min}}{2} + \varphi_{\text{ext}}\right) \right] \\ \approx & 0.16E_J, \end{aligned}$$

and we choose parameters such that  $\beta \approx 16.1$ , which sets the plasma frequency of the antisymmetric mode to  $\omega_- \equiv \sqrt{8\beta E_C E_{J,-}} \approx 2\pi \times 24.43$  GHz  $\approx 2\omega_d$ . Far from this frequency and for small to moderate  $g$ , the spectrum remains free of unwanted resonances. To probe a worst-case scenario, we set  $g/2\pi = 100$  MHz, making the capacitive coupling the dominant interaction.

As in the previous section, we first diagonalize the Hamiltonian in Eq. (20) to obtain the dressed eigenstates  $\{|i_s, j_a\rangle\}$ , where  $i_s$  and  $j_a$  label excitations in the symmetric and antisymmetric modes, respectively. We then add the drive to the symmetric mode and compute the Floquet spectrum as a function of drive amplitude, shown in Fig. 10(a). As with the case of the buffer mode, the pairwise spectral kissing among the quasienergies  $\epsilon_{n_s, 0_a}$  is interrupted by avoided crossings with quasienergies  $\epsilon_{m_s, 1_a}$ . Here, for clarity, we have chosen to label the Floquet spectrum following the asymptotic modes across each crossing. We also note that, just like with the buffer mode, there are no selection rules: all crossings seen in Fig. 10(a) are actual avoided crossings.

This spectrum reveals two key differences compared to the case of the buffer mode. First, for drive amplitudes above  $\sim 4.2$  GHz (shaded area), there are no avoided crossings disrupting the quasidegenerate pairs 0–1, 2–3, 4–5, and 5–6, which implies that the tunneling time should remain long throughout this range. Second, at lower drive amplitudes, hybridization with the antisymmetric mode involves only low-lying symmetric states. In contrast, in the buffer-mode case, the Kerr-cat is excited to high-energy levels, resulting in significant leakage out of the metapotential double well.

Moving on to the dissipative dynamics, we use the same Floquet–Markov master equation as in Sec. II. Since the drive port couples much more strongly to the symmetric mode than to the higher-energy modes [61], we assume only the symmetric mode to be lossy, coupled to the

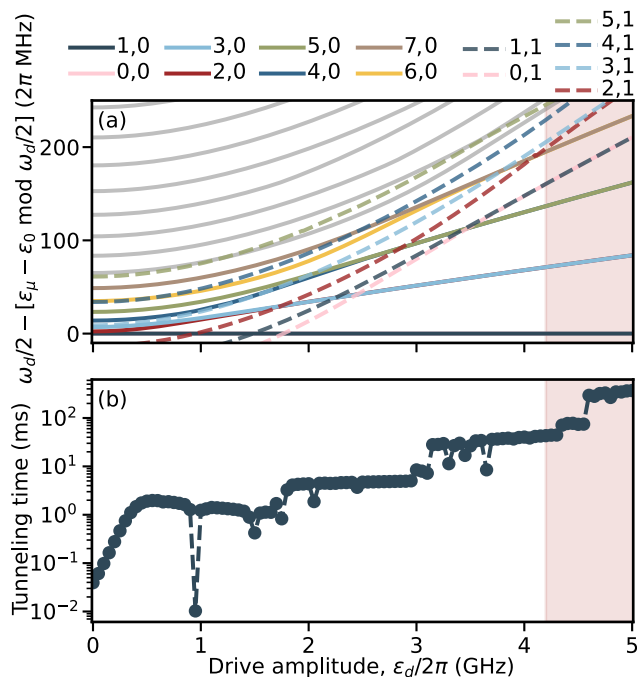


FIG. 10. (a) Spectral kissing of the quasienergies in the presence of one of the Josephson-junction array modes. Solid lines indicate the lowest quasienergies corresponding to modes with zero excitation in the array’s antisymmetric mode, while dashed lines correspond to modes with one excitation. No crossings are interrupting the spectral kissing of the relevant quasienergies above  $\sim 4.2$  GHz indicated by the shaded area. (b) The corresponding tunneling time as a function of drive amplitude.

environment via the charge operator  $\hat{n}$ . We take the same environment spectral density and frequency-dependent temperature as in Sec. II. Figure 10(b) shows the tunneling time as a function of drive amplitude, computed from the assignment error probability. As before, it exhibits a staircase-like increase interrupted by sharp dips associated with resonances in the Floquet spectrum. A prominent dip occurs at  $\varepsilon_d/2\pi \approx 1$  GHz due to the resonance between  $(1_s, 0_a)$  and  $(2_s, 1_a)$ . Crucially, however, the tunneling time does not collapse as it does in the buffer-mode case. For this set of parameters, in the high-drive regime  $\varepsilon_d/2\pi \gtrsim 4$  GHz (shaded area)—where resonances would be most detrimental—there are no resonances involving the relevant quasidegenerate quasienergy pairs. As a result, the tunneling time continues to increase without disruption. Moreover, for small ground capacitances and thus small  $g$  (e.g.,  $\lesssim 2\pi \times 10$  MHz), multiphoton resonances with the array modes become very weak. We therefore believe they are not responsible for the breakdown of the staircase pattern observed in Ref. [34].

## V. CONCLUSION

We show that, within the single-mode approximation, the staircase pattern of the Kerr-cat qubit’s tunneling time persists up to high drive amplitudes. In other words, the Kerr-cat qubit is intrinsically robust. This conclusion is reached by using a Floquet–Markov master equation that accounts for quasidegeneracies in the spectrum and treats nonperturbatively both the Josephson junction nonlinearity and the drive. In this framework, the plateaus in tunneling time as a function of drive amplitude arise from the coherent addition of dissipative transitions between quasidegenerate level pairs: at each spectral kissing point, tunneling between the wells of the metapotential is suppressed due to destructive interference between two relaxation pathways. Furthermore, we find that the tunneling time does not reliably indicate the Kerr-cat qubit’s coherence time  $T_Z$ , which is determined from the initial decay of the logical Pauli operator  $\hat{X}_L = |\beta + \alpha\rangle\langle\beta + \alpha| - |\beta - \alpha\rangle\langle\beta - \alpha|$ .

To reproduce the experimentally observed breakdown of the staircase pattern, we account for additional modes present in the implementation of the Kerr-cat qubit. Specifically, we consider the impact of the buffer mode through which the Kerr-cat is driven, the collective array modes of the double SNAIL used in the Kerr-cat qubit circuit, and the presence of a stray geometric inductance (Appendix G). For the parameters of the experiment of Refs. [30, 34], we find that the presence of these additional modes leads to multiphoton resonances in the quasienergy spectra. This type of resonance is understood to be responsible for ionization of highly-excited hydrogen atoms [42] and drive-induced transitions in transmon qubits [43–50]. Here, however, we find that mainly resonances caused by the buffer mode lead to a breakdown of the Kerr-cat’s staircase pattern. This conclusion aligns with recent studies that also identify multimode resonances as a limiting factor to the performance of strongly driven superconducting devices [51, 52, 72, 74]. Importantly, because the tunneling time depends on near-degeneracies among higher excited levels, resonances involving those levels impact Kerr-cat coherence. This is to be contrasted with the case of the transmon where only resonances within the computational subspace have a direct impact on ionization.

These observations come with a silver lining: the robustness of the Kerr-cat qubit in the absence of the buffer mode suggests that it should be possible to engineer the system in a way that restores this intrinsic protection. A key design element is the sign of the buffer–drive detuning. Placing the buffer above the drive frequency produces numerous resonances, whereas tuning it below the drive suppresses them almost entirely; see Appendix E2. This asymmetry arises from the negative anharmonicity of the double-SNAIL element. This suggests an approach to save the Kerr-cat qubit from its premature demise. Moreover, mitigating intrawell leak-

age—through, for instance, leakage-reduction techniques [36, 75, 76]—can further extend both the tunneling time and the coherence time  $T_Z$ , narrowing the discrepancy between them.

To further improve our predictions of the tunneling time and their comparison to experiment, it would be valuable to include  $1/f$  noise by averaging over fluctuations of the external flux around the operating point. In practice, this involves computing the distribution of tunneling times obtained from the Floquet–Markov treatment for different flux realizations. This form of noise has been shown to affect primarily the initial rise of the tunneling time, leaving its behavior at higher drive amplitudes essentially unchanged [30, 32]. As discussed in Sec. II E, having a more refined model—ideally informed by experiments—of the spectral density seen by the system would help more accurately match the height of the plateaus of the staircase. Moreover, although some avoided crossings may not affect the tunneling time when the system is not biased near a resonance by the drive, they still pose a problem for the adiabatic preparation of cat states. All avoided crossings affecting the Kerr-cat’s quasienergies  $\epsilon_{0_s,0_a}$  and  $\epsilon_{1_s,0_a}$  must be traversed rapidly enough for the system to evolve diabatically. Landau-Zener transition probabilities can be directly computed

from the Floquet spectrum using the methods presented here, which could inform future experiments.

Finally, although our analysis focuses on the Kerr-cat qubit, the methods developed here apply broadly to any strongly driven system with quasidegenerate spectra. Examples include superconducting circuits under subharmonic drives and subject to dissipation, as well as protected qubits operating in double-well potentials, where quasidegeneracies similarly govern coherence and tunneling dynamics.

## VI. ACKNOWLEDGMENTS

The authors are grateful to Manuel Muñoz-Arias, Nicholas E. Frattini, and Benjamin L. Brock for helpful discussions. This material is based upon work supported by the U.S. Department of Energy, Office of Science, National Quantum Information Science Research Centers, Quantum Systems Accelerator. Additional support is acknowledged from NSERC, the Ministère de l’Économie et de l’Innovation du Québec, the Fonds de recherche du Québec – Nature et technologie and the Canada First Research Excellence Fund, and the National Agency for Research and Development (ANID) through FONDECYT Postdoctoral Grant No. 3250130.

- 
- [1] I. L. Chuang, D. W. Leung, and Y. Yamamoto, Bosonic quantum codes for amplitude damping, *Phys. Rev. A* **56**, 1114 (1997).
  - [2] P. T. Cochrane, G. J. Milburn, and W. J. Munro, Macroscopically distinct quantum-superposition states as a bosonic code for amplitude damping, *Phys. Rev. A* **59**, 2631 (1999).
  - [3] D. Gottesman, A. Kitaev, and J. Preskill, Encoding a qubit in an oscillator, *Phys. Rev. A* **64**, 012310 (2001).
  - [4] J. Niset, U. L. Andersen, and N. J. Cerf, Experimentally feasible quantum erasure-correcting code for continuous variables, *Phys. Rev. Lett.* **101**, 130503 (2008).
  - [5] Z. Leghtas, G. Kirchmair, B. Vlastakis, R. J. Schoelkopf, M. H. Devoret, and M. Mirrahimi, Hardware-efficient autonomous quantum memory protection, *Phys. Rev. Lett.* **111**, 120501 (2013).
  - [6] M. H. Michael, M. Silveri, R. T. Brierley, V. V. Albert, J. Salmilehto, L. Jiang, and S. M. Girvin, New class of quantum error-correcting codes for a bosonic mode, *Phys. Rev. X* **6**, 031006 (2016).
  - [7] M.-A. Lemonde, D. Lachance-Quirion, G. Duclos-Cianci, N. E. Frattini, F. Hopfmueller, C. Gauvin-Ndiaye, J. Camirand-Lemyre, and P. St-Jean, [Hardware-efficient fault tolerant quantum computing with bosonic grid states in superconducting circuits](https://arxiv.org/abs/2409.05813) (2024), [arXiv:2409.05813 \[quant-ph\]](https://arxiv.org/abs/2409.05813).
  - [8] J. Guillaud, J. Cohen, and M. Mirrahimi, Quantum computation with cat qubits, *SciPost Phys. Lect. Notes* **72** (2023).
  - [9] M. Mirrahimi, Z. Leghtas, V. V. Albert, S. Touzard, R. J. Schoelkopf, L. Jiang, and M. H. Devoret, Dynamically protected cat-qubits: a new paradigm for universal quantum computation, *New J. Phys.* **16**, 045014 (2014).
  - [10] Z. Leghtas, S. Touzard, I. M. Pop, A. Kou, B. Vlastakis, A. Petrenko, K. M. Sliwa, A. Narla, S. Shankar, M. J. Hatridge, M. Reagor, L. Frunzio, R. J. Schoelkopf, M. Mirrahimi, and M. H. Devoret, Confining the state of light to a quantum manifold by engineered two-photon loss, *Science* **347**, 853–857 (2015).
  - [11] S. Puri, S. Boutin, and A. Blais, Engineering the quantum states of light in a Kerr-nonlinear resonator by two-photon driving, *npj Quantum Inf.* **3**, 18 (2017).
  - [12] P. Aliferis and J. Preskill, Fault-tolerant quantum computation against biased noise, *Phys. Rev. A* **78**, 052331 (2008).
  - [13] P. Aliferis, F. Brito, D. P. DiVincenzo, J. Preskill, M. Steffen, and B. M. Terhal, Fault-tolerant computing with biased-noise superconducting qubits: a case study, *New J. Phys.* **11**, 013061 (2009).
  - [14] D. K. Tuckett, S. D. Bartlett, and S. T. Flammia, Ultra-high error threshold for surface codes with biased noise, *Phys. Rev. Lett.* **120**, 050505 (2018).
  - [15] D. K. Tuckett, A. S. Darmawan, C. T. Chubb, S. Bravyi, S. D. Bartlett, and S. T. Flammia, Tailoring surface codes for highly biased noise, *Phys. Rev. X* **9**, 041031 (2019).
  - [16] J. Guillaud and M. Mirrahimi, Repetition cat qubits for fault-tolerant quantum computation, *Phys. Rev. X* **9**, 041053 (2019).
  - [17] A. S. Darmawan, B. J. Brown, A. L. Grimsmo, D. K. Tuckett, and S. Puri, Practical quantum error correction with the XZZX code and Kerr-cat qubits, *PRX*

- Quantum* **2**, 030345 (2021).
- [18] J. P. Bonilla Ataides, D. K. Tuckett, S. D. Bartlett, S. T. Flammia, and B. J. Brown, The XZZX surface code, *Nat. Commun.* **12**, 2172 (2021).
- [19] J. Guillaud and M. Mirrahimi, Error rates and resource overheads of repetition cat qubits, *Phys. Rev. A* **103**, 042413 (2021).
- [20] C. Chamberland, K. Noh, P. Arrangoiz-Arriola, E. T. Campbell, C. T. Hann, J. Iverson, H. Putterman, T. C. Bohdanowicz, S. T. Flammia, A. Keller, G. Refael, J. Preskill, L. Jiang, A. H. Safavi-Naeini, O. Painter, and F. G. Brandão, Building a fault-tolerant quantum computer using concatenated cat codes, *PRX Quantum* **3**, 010329 (2022).
- [21] S. Touzard, A. Grimm, Z. Leghtas, S. O. Mundhada, P. Reinhold, C. Axline, M. Reagor, K. Chou, J. Blumoff, K. M. Sliwa, S. Shankar, L. Frunzio, R. J. Schoelkopf, M. Mirrahimi, and M. H. Devoret, Coherent oscillations inside a quantum manifold stabilized by dissipation, *Phys. Rev. X* **8**, 021005 (2018).
- [22] R. Lescanne, M. Villiers, T. Peronnin, L. Morvan, P. Vernaz-Gris, W. Marcantoni, P. Rouchon, A. Sarlette, M. Mirrahimi, and P. Campagne-Ibarcq, Exponential suppression of bit-flips in a qubit encoded in an oscillator, *Nat. Phys.* **16**, 509 (2020).
- [23] C. Berdou, A. Murani, U. Réglade, W. Smith, M. Villiers, J. Palomo, M. Rosticher, A. Denis, P. Morfin, M. Delbecq, T. Kontos, N. Pankratova, F. Rautschke, T. Peronnin, L.-A. Sellem, P. Rouchon, A. Sarlette, M. Mirrahimi, P. Campagne-Ibarcq, S. Jezouin, R. Lescanne, and Z. Leghtas, One hundred second bit-flip time in a two-photon dissipative oscillator, *PRX Quantum* **4**, 020350 (2023).
- [24] U. Réglade, A. Bocquet, R. Gautier, J. Cohen, A. Marquet, E. Albertinale, N. Pankratova, M. Hallén, F. Rautschke, L.-A. Sellem, P. Rouchon, A. Sarlette, M. Mirrahimi, P. Campagne-Ibarcq, R. Lescanne, S. Jezouin, and Z. Leghtas, Quantum control of a cat qubit with bit-flip times exceeding ten seconds, *Nature* **629**, 778 (2024).
- [25] A. Marquet, A. Essig, J. Cohen, N. Cottet, A. Murani, E. Albertinale, S. Dupouy, A. Bienfait, T. Peronnin, S. Jezouin, R. Lescanne, and B. Huard, Autoparametric resonance extending the bit-flip time of a cat qubit up to 0.3 s, *Phys. Rev. X* **14**, 021019 (2024).
- [26] H. Putterman, K. Noh, R. N. Patel, G. A. Peairs, G. S. MacCabe, M. Lee, S. Aghaeimebodi, C. T. Hann, I. Jarrige, G. Marcaud, Y. He, H. Moradinejad, J. C. Owens, T. Scaffidi, P. Arrangoiz-Arriola, J. Iverson, H. Levine, F. G. S. L. Brandão, M. H. Matheny, and O. Painter, Preserving phase coherence and linearity in cat qubits with exponential bit-flip suppression, *Phys. Rev. X* **15**, 011070 (2025).
- [27] H. Putterman, K. Noh, C. T. Hann, G. S. MacCabe, S. Aghaeimebodi, R. N. Patel, M. Lee, W. M. Jones, H. Moradinejad, R. Rodriguez, N. Mahuli, J. Rose, J. C. Owens, H. Levine, E. Rosenfeld, P. Reinhold, L. Monceli, J. A. Alcid, N. Alidoust, P. Arrangoiz-Arriola, J. Barnett, P. Bienias, H. A. Carson, C. Chen, L. Chen, H. Chinkeziyan, E. M. Chisholm, M.-H. Chou, A. Clerk, A. Clifford, R. Cosmic, A. V. Curiel, E. Davis, L. DeLorenzo, J. M. D'Ewart, A. Diky, N. D'Souza, P. T. Dumitrescu, S. Eisenmann, E. Elkhouly, G. Evenbly, M. T. Fang, Y. Fang, M. J. Fling, W. Fon, G. Garcia, A. V. Gorshkov, J. A. Grant, M. J. Gray, S. Grimberg, A. L. Grimsmo, A. Haim, J. Hand, Y. He, M. Hernandez, D. Hover, J. S. C. Hung, M. Hunt, J. Iverson, I. Jarrige, J.-C. Jaskula, L. Jiang, M. Kalaei, R. Karabalin, P. J. Karalekas, A. J. Keller, A. Khalajhedayati, A. Kubica, H. Lee, C. Leroux, S. Lieu, V. Ly, K. V. Madrigal, G. Marcaud, G. McCabe, C. Miles, A. Milsted, J. Minguzzi, A. Mishra, B. Mukherjee, M. Naghiloo, E. Oblepias, G. Ortuno, J. Pagdilaio, N. Pancotti, A. Panduro, J. Paquette, M. Park, G. A. Peairs, D. Perello, E. C. Peterson, S. Ponte, J. Preskill, J. Qiao, G. Refael, R. Resnick, A. Retzker, O. A. Reyna, M. Runyan, C. A. Ryan, A. Sahnoud, E. Sanchez, R. Sanil, K. Sankar, Y. Sato, T. Scaffidi, S. Siavoshi, P. Sivaraajah, T. Skogland, C.-J. Su, L. J. Swenson, S. M. Teo, A. Tomada, G. Torlai, E. A. Wollack, Y. Ye, J. A. Zerrudo, K. Zhang, F. G. S. L. Brandão, M. H. Matheny, and O. Painter, Hardware-efficient quantum error correction via concatenated bosonic qubits, *Nature* **638**, 927 (2025).
- [28] H. Goto, Bifurcation-based adiabatic quantum computation with a nonlinear oscillator network, *Sci. Rep.* **6**, 21686 (2016).
- [29] A. Grimm, N. E. Frattini, S. Puri, S. O. Mundhada, S. Touzard, M. Mirrahimi, S. M. Girvin, S. Shankar, and M. H. Devoret, Stabilization and operation of a Kerr-cat qubit, *Nature* **584**, 205–209 (2020).
- [30] N. E. Frattini, R. G. Cortiñas, J. Venkatraman, X. Xiao, Q. Su, C. U. Lei, B. J. Chapman, V. R. Joshi, S. M. Girvin, R. J. Schoelkopf, S. Puri, and M. H. Devoret, Observation of pairwise level degeneracies and the quantum regime of the Arrhenius law in a double-well parametric oscillator, *Phys. Rev. X* **14**, 031040 (2024).
- [31] J. Venkatraman, R. G. Cortiñas, N. E. Frattini, X. Xiao, and M. H. Devoret, A driven Kerr oscillator with twofold degeneracies for qubit protection, *Proc. Natl. Acad. Sci. U.S.A.* **121**, e2311241121 (2024).
- [32] A. Hajr, B. Qing, K. Wang, G. Koolstra, Z. Pedramrazi, Z. Kang, L. Chen, L. B. Nguyen, C. Jünger, N. Goss, I. Huang, B. Bhandari, N. E. Frattini, S. Puri, J. Dreschel, A. N. Jordan, D. I. Santiago, and I. Siddiqi, High-coherence Kerr-cat qubit in 2D architecture, *Phys. Rev. X* **14**, 041049 (2024).
- [33] A. Z. Ding, B. L. Brock, A. Eickbusch, A. Koottandavida, N. E. Frattini, R. G. Cortiñas, V. R. Joshi, S. J. de Graaf, B. J. Chapman, S. Ganjam, *et al.*, Quantum control of an oscillator with a Kerr-cat qubit, *Nat. Commun.* **16**, 1 (2025).
- [34] A. C. C. de Albornoz, R. G. Cortiñas, M. Schäfer, N. E. Frattini, B. Allen, D. G. Cabral, P. E. Videla, P. Khazaei, E. Geva, V. S. Batista, *et al.*, Oscillatory dissipative tunneling in an asymmetric double-well potential, *arXiv preprint arXiv:2409.13113* (2024).
- [35] A. Polkovnikov, Phase space representation of quantum dynamics, *Ann. Physics* **325**, 1790 (2010).
- [36] H. Putterman, J. Iverson, Q. Xu, L. Jiang, O. Painter, F. G. S. L. Brandão, and K. Noh, Stabilizing a bosonic qubit using colored dissipation, *Phys. Rev. Lett.* **128**, 110502 (2022).
- [37] D. Ruiz, R. Gautier, J. Guillaud, and M. Mirrahimi, Two-photon driven Kerr quantum oscillator with multiple spectral degeneracies, *Phys. Rev. A* **107**, 042407 (2023).

- [38] Q. Su, R. G. Cortiñas, J. Venkatraman, and S. Puri, Unraveling the switching dynamics in a quantum double-well potential, [arXiv preprint arXiv:2501.00209 \(2024\)](#).
- [39] J. Venkatraman, X. Xiao, R. G. Cortiñas, and M. H. Devoret, Nonlinear dissipation in a driven superconducting circuit, *Phys. Rev. A* **110**, 042411 (2024).
- [40] Personal communication with nicholas e. fratinni and benjamin l. brock.
- [41] N. E. Frattini, U. Vool, S. Shankar, A. Narla, K. M. Sliwa, and M. H. Devoret, 3-wave mixing Josephson dipole element, *Appl. Phys. Lett.* **110**, 222603 (2017).
- [42] H. P. Breuer and M. Holthaus, Adiabatic processes in the ionization of highly excited hydrogen atoms, *Z. Phys. D* **11**, 1 (1989).
- [43] D. Sank, Z. Chen, M. Khezri, J. Kelly, R. Barends, B. Campbell, Y. Chen, B. Chiaro, A. Dunsworth, A. Fowler, E. Jeffrey, E. Lucero, A. Megrant, J. Mutus, M. Neeley, C. Neill, P. J. J. O'Malley, C. Quintana, P. Roushan, A. Vainsencher, T. White, J. Wenner, A. N. Korotkov, and J. M. Martinis, Measurement-induced state transitions in a superconducting qubit: Beyond the rotating wave approximation, *Phys. Rev. Lett.* **117**, 190503 (2016).
- [44] M. Khezri, A. Opremcak, Z. Chen, K. C. Miao, M. McEwen, A. Bengtsson, T. White, O. Naaman, D. Sank, A. N. Korotkov, Y. Chen, and V. Smelyanskiy, Measurement-induced state transitions in a superconducting qubit: Within the rotating-wave approximation, *Phys. Rev. Appl.* **20**, 054008 (2023).
- [45] R. Shillito, A. Petrescu, J. Cohen, J. Beall, M. Hauru, M. Ganahl, A. G. Lewis, G. Vidal, and A. Blais, Dynamics of transmon ionization, *Phys. Rev. Appl.* **18**, 034031 (2022).
- [46] J. Cohen, A. Petrescu, R. Shillito, and A. Blais, Reminiscence of classical chaos in driven transmons, *PRX Quantum* **4**, 020312 (2023).
- [47] M. F. Dumas, B. Groleau-Paré, A. McDonald, M. H. Muñoz Arias, C. Lledó, B. D'Anjou, and A. Blais, Measurement-induced transmon ionization, *Phys. Rev. X* **14**, 041023 (2024).
- [48] M. Féchant, M. F. Dumas, D. Bénâtre, N. Gosling, P. Lenhard, M. Spiecker, W. Wernsdorfer, B. D'Anjou, A. Blais, and I. M. Pop, Offset charge dependence of measurement-induced transitions in transmons, [arXiv preprint arXiv:2505.00674 \(2025\)](#).
- [49] Z. Wang, B. D'Anjou, P. Gigon, A. Blais, and M. S. Blok, Probing excited-state dynamics of transmon ionization, [arXiv preprint arXiv:2505.00639 \(2025\)](#).
- [50] M. Xia, C. Lledó, M. Capocci, J. Repicky, B. D'Anjou, I. Mondragon-Shem, R. Kaufman, J. Koch, A. Blais, and M. Hatridge, Exceeding the parametric drive strength threshold in nonlinear circuits, [arXiv preprint arXiv:2506.03456 \(2025\)](#).
- [51] T. Connolly, P. D. Kurilovich, V. D. Kurilovich, C. G. L. Böttcher, S. Hazra, W. Dai, A. Z. Ding, V. R. Joshi, H. Nho, S. Diamond, D. K. Weiss, V. Fatemi, L. Frunzio, L. I. Glazman, and M. H. Devoret, Full characterization of measurement-induced transitions of a superconducting qubit, [arXiv preprint arXiv:2506.05306 \(2025\)](#).
- [52] W. Dai, S. Hazra, D. K. Weiss, P. D. Kurilovich, T. Connolly, H. K. Babla, S. Singh, V. R. Joshi, A. Z. Ding, P. D. Parakh, J. Venkatraman, X. Xiao, L. Frunzio, and M. H. Devoret, Spectroscopy of drive-induced unwanted state transitions in superconducting circuits, [arXiv preprint arXiv:2506.24070 \(2025\)](#).
- [53] B. Oelschlägel, T. Dittrich, and P. Hänggi, Damped periodically driven quantum transport in bistable systems, *Acta Phys. Pol. B* **24**, 845 (1993).
- [54] S. Kohler, T. Dittrich, and P. Hänggi, Floquet-Markovian description of the parametrically driven, dissipative harmonic quantum oscillator, *Phys. Rev. E* **55**, 300 (1997).
- [55] M. Grifoni and P. Hänggi, Driven quantum tunneling, *Phys. Rep.* **304**, 229 (1998).
- [56] V. Sivak, N. Frattini, V. Joshi, A. Lingenfelter, S. Shankar, and M. Devoret, Kerr-free three-wave mixing in superconducting quantum circuits, *Phys. Rev. Appl.* **11**, 054060 (2019).
- [57] B. R. Mollow, Pure-state analysis of resonant light scattering: Radiative damping, saturation, and multiphoton effects, *Phys. Rev. A* **12**, 1919 (1975).
- [58] C. Lledó, R. Dassonneville, A. Moulinas, J. Cohen, R. Shillito, A. Bienfait, B. Huard, and A. Blais, Cloaking a qubit in a cavity, *Nat. Commun.* **14**, 6313 (2023).
- [59] N. A. Masluk, I. M. Pop, A. Kamal, Z. K. Mineev, and M. H. Devoret, Microwave characterization of Josephson junction arrays: Implementing a low loss superinductance, *Phys. Rev. Lett.* **109**, 137002 (2012).
- [60] D. G. Ferguson, A. A. Houck, and J. Koch, Symmetries and collective excitations in large superconducting circuits, *Phys. Rev. X* **3**, 011003 (2013).
- [61] G. Viola and G. Catelani, Collective modes in the fluxonium qubit, *Phys. Rev. B* **92**, 224511 (2015).
- [62] R. Shillito, A. Petrescu, J. Cohen, J. Beall, M. Hauru, M. Ganahl, A. G. Lewis, G. Vidal, and A. Blais, Dynamics of transmon ionization, *Phys. Rev. Appl.* **18**, 034031 (2022).
- [63] H. Breuer and M. Holthaus, Quantum phases and Landau-Zener transitions in oscillating fields, *Phys. Lett. A* **140**, 507 (1989).
- [64] J. Chávez-Carlos, M. A. Prado Reynoso, R. G. Cortiñas, I. García-Mata, V. S. Batista, F. Pérez-Bernal, D. A. Wisniacki, and L. F. Santos, Driving superconducting qubits into chaos, *Quantum Sci. Technol.* **10**, 015039 (2024).
- [65] R. Blümel, A. Buchleitner, R. Graham, L. Sirko, U. Smilansky, and H. Walther, Dynamical localization in the microwave interaction of Rydberg atoms: The influence of noise, *Phys. Rev. A* **44**, 4521 (1991).
- [66] H. P. Breuer and F. Petruccione, *The theory of open quantum systems* (Oxford University Press, Great Clarendon Street, 2002).
- [67] T. Mori, Floquet states in open quantum systems, *Annu. Rev. Condens. Matter Phys.* **14**, 35 (2023).
- [68] A. Rivas, A. D. K. Plato, S. F. Huelga, and M. B. Plenio, Markovian master equations: a critical study, *New Journal of Physics* **12**, 113032 (2010).
- [69] S. Puri, A. Grimm, P. Campagne-Ibarcq, A. Eickbusch, K. Noh, G. Roberts, L. Jiang, M. Mirrahimi, M. H. Devoret, and S. M. Girvin, Stabilized cat in a driven nonlinear cavity: A fault-tolerant error syndrome detector, *Phys. Rev. X* **9**, 041009 (2019).
- [70] B. Bhandari, I. Huang, A. Hajr, K. Yanik, B. Qing, K. Wang, D. I. Santiago, J. Dressel, I. Siddiqi, and A. N. Jordan, Symmetrically threaded SQUIDs as next generation Kerr-cat qubits, [arXiv preprint arXiv:2405.11375 \(2024\)](#).

- [71] X. Xiao, J. Venkatraman, R. G. Cortiñas, S. Chowdhury, and M. H. Devoret, A diagrammatic method to compute the effective Hamiltonian of driven nonlinear oscillators, [arXiv preprint arXiv:2304.13656 \(2024\)](#), [arXiv:2304.13656 \[quant-ph\]](#).
- [72] S. Singh, G. Refael, A. Clerk, and E. Rosenfeld, Impact of Josephson junction array modes on fluxonium readout, [arXiv preprint arXiv:2412.14788 \(2025\)](#), [arXiv:2412.14788 \[cond-mat.mes-hall\]](#).
- [73] A. Labay-Mora, A. Mercurio, V. Savona, G. L. Giorgi, and F. Minganti, Chiral cat code: Enhanced error correction induced by higher-order nonlinearities, [arXiv preprint arXiv:2503.11624 \(2025\)](#).
- [74] L. Carde, P. Rouchon, J. Cohen, and A. Petrescu, Flux-pump-induced degradation of  $T_1$  for dissipative cat qubits, *Phys. Rev. Appl.* **23**, 024073 (2025).
- [75] D. Haxell, F. Adinolfi, A. Bruno, L. Michaud, V. H. Kamrul, P. Pandey, and A. Grimm, Enhancing the coherent-state lifetime of a Kerr-cat qubit through leakage suppression (part i), APS March Meeting 2025, Session MAR-A17, Anaheim Convention Center (2025), presented on March 17, 2025.
- [76] F. Adinolfi, D. Haxell, A. Bruno, L. Michaud, V. H. Kamrul, P. Pandey, and A. Grimm, Enhancing the coherent-state lifetime of a Kerr-cat qubit through leakage suppression (part ii), APS March Meeting 2025, Session MAR-A17, Anaheim Convention Center (2025), presented on March 17, 2025.
- [77] T. Bilitewski and N. R. Cooper, Scattering theory for Floquet-Bloch states, *Phys. Rev. A* **91**, 033601 (2015).
- [78] J. Jeske, D. J. Ing, M. B. Plenio, S. F. Huelga, and J. H. Cole, Bloch-Redfield equations for modeling light-harvesting complexes, *J. Chem. Phys.* **142**, 064104 (2015).
- [79] D. Farina and V. Giovannetti, Open-quantum-system dynamics: Recovering positivity of the Redfield equation via the partial secular approximation, *Phys. Rev. A* **100**, 012107 (2019).
- [80] M. Cattaneo, G. L. Giorgi, S. Maniscalco, and R. Zambri, Local versus global master equation with common and separate baths: superiority of the global approach in partial secular approximation, *New J. Phys.* **21**, 113045 (2019).
- [81] A. Trushechkin, Unified Gorini-Kossakowski-Lindblad-Sudarshan quantum master equation beyond the secular approximation, *Phys. Rev. A* **103**, 062226 (2021).
- [82] P. Jurcevic and L. C. G. Govia, Effective qubit dephasing induced by spectator-qubit relaxation, *Quantum Science and Technology* **7**, 045033 (2022).
- [83] A. Petrescu, M. Malekakhlagh, and H. E. Türeci, Lifetime renormalization of driven weakly anharmonic superconducting qubits. II. The readout problem, *Phys. Rev. B* **101**, 134510 (2020).
- [84] L. Verney, R. Lescanne, M. H. Devoret, Z. Leghtas, and M. Mirrahimi, Structural instability of driven Josephson circuits prevented by an inductive shunt, *Phys. Rev. Appl.* **11**, 024003 (2019).
- [85] M. Burgelman, P. Rouchon, A. Sarlette, and M. Mirrahimi, Structurally stable subharmonic regime of a driven quantum Josephson circuit, *Phys. Rev. Appl.* **18**, 064044 (2022).
- [86] G. Kiršanskas, M. Franckić, and A. Wacker, Phenomenological position and energy resolving Lindblad approach to quantum kinetics, *Phys. Rev. B* **97**, 035432 (2018).
- [87] E. Kleinerherbers, N. Szpak, J. König, and R. Schützhold, Relaxation dynamics in a Hubbard dimer coupled to fermionic baths: Phenomenological description and its microscopic foundation, *Phys. Rev. B* **101**, 125131 (2020).
- [88] E. Mozhgunov and D. Lidar, Completely positive master equation for arbitrary driving and small level spacing, *Quantum* **4**, 227 (2020).
- [89] G. McCauley, B. Cruikshank, D. I. Bondar, and K. Jacobs, Accurate Lindblad-form master equation for weakly damped quantum systems across all regimes, *npj Quantum Inf.* **6**, 74 (2020).
- [90] F. Nathan and M. S. Rudner, Universal Lindblad equation for open quantum systems, *Phys. Rev. B* **102**, 115109 (2020).
- [91] J. H. Shirley, Solution of the Schrödinger equation with a Hamiltonian periodic in time, *Phys. Rev.* **138**, B979 (1965).
- [92] S. Bravyi, D. P. DiVincenzo, and D. Loss, Schrieffer-Wolff transformation for quantum many-body systems, *Ann. Phys.* **326**, 2793 (2011).
- [93] M. Nakagawa and N. Kawakami, Nonequilibrium topological phase transitions in two-dimensional optical lattices, *Phys. Rev. A* **89**, 013627 (2014).
- [94] M. Bukov, L. D'Alessio, and A. Polkovnikov, Universal high-frequency behavior of periodically driven systems: from dynamical stabilization to Floquet engineering, *Adv. Phys.* **64**, 139 (2015).
- [95] L. S. Theis and F. K. Wilhelm, Nonadiabatic corrections to fast dispersive multiqubit gates involving  $z$  control, *Phys. Rev. A* **95**, 022314 (2017).
- [96] J. Venkatraman, X. Xiao, R. G. Cortiñas, A. Eickbusch, and M. H. Devoret, Static effective Hamiltonian of a rapidly driven nonlinear system, *Phys. Rev. Lett.* **129**, 100601 (2022).
- [97] A. Petrescu, C. Le Calonnec, C. Leroux, A. Di Paolo, P. Mundada, S. Sussman, A. Vrajitoarea, A. A. Houck, and A. Blais, Accurate methods for the analysis of strong-drive effects in parametric gates, *Phys. Rev. Appl.* **19**, 044003 (2023).
- [98] N. E. Frattini, *Three-wave mixing in superconducting circuits: Stabilizing cats with SNAILs*, Ph.D. thesis, Yale University (2021).
- [99] D. Kafri, C. Quintana, Y. Chen, A. Shabani, J. M. Martinis, and H. Neven, Tunable inductive coupling of superconducting qubits in the strongly nonlinear regime, *Phys. Rev. A* **95**, 052333 (2017).
- [100] R. P. Feynman, R. B. Leighton, and M. Sands, *The Feynman Lectures on Physics*, Vol. 2 (Addison-Wesley, 1964) Chap. 23, reprinted by Springer, 1992.

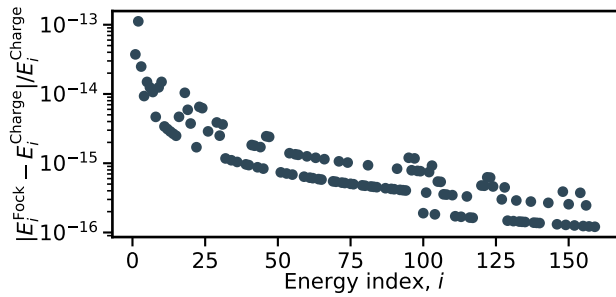


FIG. 11. Relative error in the energies obtained from numerical diagonalization of the double-SNAIL Hamiltonian  $\hat{H}_s$  (see Eq. (5)), comparing results from the Fock basis and the charge basis. Convergence with respect to the maximum charge ( $n_{\max} = 400$ ) in  $\hat{n} = \sum_{n=-n_{\max}}^{\max} |n\rangle\langle n|$  is verified independently. The Fock basis is truncated at  $n_{\text{cut}} = 250$ . As is typical for periodic-potential Hamiltonians, diagonalization in the Fock basis does not converge with increasing  $n_{\text{cut}}$ ; therefore, comparison with the charge basis is necessary to assess accuracy.

### Appendix A: Numerical details of the Floquet analysis

In this Appendix, we provide additional numerical details supporting the simulations presented in Sec. II of the main text. The single-mode Hamiltonian  $\hat{H}_s$  introduced in Eq.(4) exhibits a  $12\pi$  phase periodicity and should, in principle, be diagonalized in either the charge or phase basis. However, for experimentally relevant parameters, the potential wells are sufficiently deep that diagonalization in the Fock basis provides a spectrum nearly identical—up to numerical precision—to that obtained in the charge basis, at least for the lowest  $\sim 160$  energy levels, see Fig. 11. Given the convenience of the Fock basis for phase-space representations, we adopt it throughout this work.

Our numerical simulations employ a Hilbert space truncated at 250 Fock states for diagonalization, from which the lowest 160 energy levels are retained for Floquet-state tracking. The relatively large Hilbert space size is necessary due to the small Kerr nonlinearity of the double-SNAIL mode,  $K/2\pi = 1.18$  MHz. This weak nonlinearity allows the potential to support approximately 530 bound states, nearly all of which—except those close to the top of the potential well—experience a positive ac-Stark shift. Truncating below this number introduces an artificial negative Stark shift in the highest retained levels, causing resonances with lower energy levels as the drive amplitude increases. Such truncation effects can ultimately impact the low-lying levels critical for Kerr-cat physics. For instance, retaining only 120 levels introduces truncation errors for drive amplitudes exceeding  $\varepsilon_d/2\pi \approx 8.5$  GHz. Throughout this work, we consistently retain 160 levels, which we have verified are sufficient for drive amplitudes up to at least

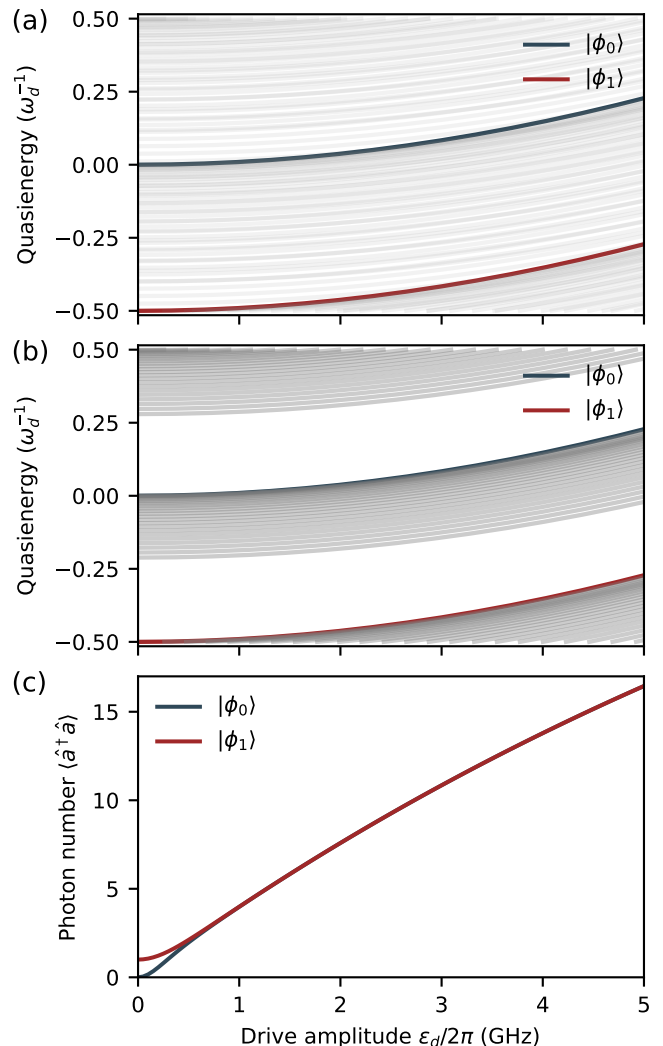


FIG. 12. (a) Floquet quasienergies of the lowest 100 modes plotted as a function of drive amplitude. The lowest Floquet modes  $\mu = 0$  and  $\mu = 1$  are indicated by dark blue and red lines, respectively. (b) Same plot for the lowest 50 modes, showing more clearly that the spectrum separates into two bands centered at 0 and  $-\omega_d/2 \pmod{\omega_d}$ , corresponding to even and odd states. (c) Average photon number  $\langle \hat{a}^\dagger \hat{a} \rangle$  in the  $\mu = 0$  (dark blue) and  $\mu = 1$  (red) Floquet modes, shown as a function of drive amplitude.

$\varepsilon_d/2\pi = 10$  GHz. A more thorough discussion on truncation effects in strongly driven systems can be found in Ref. [42].

In Fig. 12(a), we plot the Floquet spectrum as a function of drive amplitude, highlighting the first two Floquet modes in dark blue and red, respectively. In Fig. 12(b), we see clearly that spectrum shows two distinct bands: one centered around zero energy modulo  $\omega_d$ , corresponding to the even Floquet modes, and another centered near  $-\omega_d/2$  modulo  $\omega_d$ , associated with the odd Floquet modes. In Fig. 12(b), we present the average photon number  $\langle \hat{a}^\dagger \hat{a} \rangle$  for the two lowest Floquet modes, corre-

sponding to the cat states of interest. This allows mapping between drive amplitude and photon number (in the laboratory frame) within the cat-state manifold.

Having computed the Floquet spectrum as a function of drive amplitude, we can relate it to quantities measured experimentally in Refs. [30–33]. In these experiments, an additional weak probe tone  $\delta\hat{H}(t) = \zeta \cos(\omega_s t) \hat{n} \equiv \delta\Omega(t) \hat{n}$  at frequency  $\omega_s$  is used alongside the squeezing drive. The oscillator field is monitored via heterodyne detection, from which the tunneling time is extracted [30, 33, 34], as discussed in Sec. IID and Appendix C. Starting from coherent states  $|\beta \pm \alpha\rangle$ , transitions induced by the probe drive outside the metapotential well manifest as increased heterodyne signal amplitude corresponding to the opposite phase-space region ( $\beta \mp \alpha$ ) [30, 33, 34]. Here, we show that these transitions rates and thus the measured heterodyne signal are directly proportional to the Floquet matrix elements  $X_{\mu\nu k}$ . Indeed, writing the total Hamiltonian as

$$\hat{H}_{\text{tot}}(t) = \hat{H}(t) + \delta\hat{H}(t), \quad (\text{A1})$$

with  $\hat{H}(t)$  defined in Eq.(4) and following Ref. [77], the transition amplitude from the coherent state  $|\beta + \alpha\rangle = (|\phi_0\rangle + |\phi_1\rangle)/\sqrt{2}$  to Floquet mode  $|\phi_\mu(t)\rangle$  ( $\mu \neq 0, 1$ ), at first order of  $\delta\hat{H}$ , is given by

$$\begin{aligned} |\langle\phi_\mu(t)|\psi(t)\rangle| &= \frac{1}{\sqrt{2}} \left| \sum_k X_{\mu 0k} \int_0^t ds \delta\Omega(s) e^{i\Delta_{\mu 0k}s} \right. \\ &\quad \left. + \sum_k X_{\mu 1k} \int_0^t ds \delta\Omega(s) e^{i\Delta_{\mu 1k}s} \right|, \end{aligned} \quad (\text{A2})$$

where  $|\psi(t)\rangle = \mathcal{T} e^{-i \int_0^t ds \hat{H}_{\text{tot}}(s)} |\beta + \alpha\rangle$  is the instantaneous state. Thus, the probe drives transitions only when  $\omega_s \approx \Delta_{\mu 0k}$  or  $\omega_s \approx \Delta_{\mu 1k}$ , with rates proportional to  $X_{\mu 0k}$  and  $X_{\mu 1k}$ , respectively. Since heterodyne detection discriminates well occupancy (left or right), only those transitions that mediate interwell tunneling produce an enhanced signal; states that undergo spectral kissing no longer induce tunneling and thus become “invisible” to this measurement scheme [30, 33].

### Appendix B: Partial secular Floquet Markov master equation

In this appendix, we derive the master equation used throughout this work by extending the standard Floquet–Markov formalism [54, 55, 65] to accommodate quasidegenerate spectra. We begin from the total system–bath Hamiltonian

$$\hat{H}_{\text{tot}}(t) = \hat{H}(t) + \sum_i \omega_i \hat{b}_i^\dagger \hat{b}_i + \hat{p} \sum_i g_i \hat{p}_i, \quad (\text{B1})$$

where  $\hat{H}(t)$  is defined in Eq. (4) of the main text, and  $\hat{p} = i(\hat{a}^\dagger - \hat{a}) = \hat{n}/n_{\text{zpf}}$  and  $\hat{p}_i = i(\hat{b}_i^\dagger - \hat{b}_i)$  are the

(normalized) charge operators of the double-SNAIL and each bosonic bath mode, respectively. This Hamiltonian thus describes charge–charge coupling between the driven SNAIL circuit and its electromagnetic environment; see Fig. 2(a) and (c). Following Ref. [66], and working in the interaction picture under the Born–Markov approximation, the master equation can be expressed as

$$\begin{aligned} \frac{d\hat{\rho}^I}{dt} &= \int_0^{+\infty} d\tau \sum_i g_i^2 \\ &\times \left[ \langle \hat{p}_i^I(t) \hat{p}_i^I(t - \tau) \rangle_B (\hat{p}^I(t - \tau) \hat{\rho}^I \hat{p}^I(t) \right. \\ &\quad \left. - \hat{p}^I(t) \hat{p}^I(t - \tau) \hat{\rho}^I) \right] + \text{h.c.} \end{aligned} \quad (\text{B2})$$

Here, any operator  $\hat{O}$  in the interaction picture is denoted as  $\hat{O}^I = \mathcal{U}^\dagger(t) \hat{O} \mathcal{U}(t)$  with

$$\begin{aligned} \mathcal{U}(t) &= \mathcal{T} \exp \left[ -i \int_0^t (\hat{H}(s) + \sum_i \omega_i \hat{b}_i^\dagger \hat{b}_i) ds \right] \\ &= \hat{U}(t) e^{-it \sum_i \omega_i \hat{b}_i^\dagger \hat{b}_i}. \end{aligned} \quad (\text{B3})$$

Assuming the bath is in a thermal state, the correlation function becomes

$$\begin{aligned} \langle \hat{p}_i^I(t) \hat{p}_i^I(t - \tau) \rangle_B &= \\ n_{\text{th}}(\omega_i) e^{i\omega_i \tau} + (n_{\text{th}}(\omega_i) + 1) e^{-i\omega_i \tau}, \end{aligned} \quad (\text{B4})$$

where  $n_{\text{th}}(\omega_i) = 1/(e^{\hbar\omega_i/(k_B T(\omega_i))} - 1)$  is the average occupation of bath mode  $i$ .

Equation (B2) can be applied to any time-dependent system, as long as the dissipation is weak and exhibits short-time correlations. Given the periodicity of the Hamiltonian,  $\hat{H}(t + T) = \hat{H}(t)$ , we can now simplify the master equation by decomposing the charge operator into the Floquet-mode basis at time  $t$  as

$$\begin{aligned} \hat{p} &= \sum_{\mu\nu} \langle\phi_\mu(t)|\hat{p}|\phi_\nu(t)\rangle |\phi_\mu(t)\rangle \langle\phi_\nu(t)| \\ &= \sum_{\mu\nu k} X_{\mu\nu k} e^{+ik\omega_d t} |\phi_\mu(t)\rangle \langle\phi_\nu(t)|, \end{aligned} \quad (\text{B5})$$

where the Fourier coefficients  $X_{\mu\nu k}$  are defined in Eq.(10). Since the modes at time  $t$  are related to  $t = 0$  by  $|\phi_\mu(t)\rangle = e^{i\epsilon_\mu t} \hat{U}(t)$ , in the interaction picture the decomposition becomes

$$\hat{p}^I = \sum_{\mu\nu k} X_{\mu\nu k} e^{+i\Delta_{\mu\nu k} t} |\phi_\mu\rangle \langle\phi_\nu|, \quad (\text{B6})$$

where  $\Delta_{\mu\nu k} = \epsilon_\mu - \epsilon_\nu + k\omega_d$ . Substituting Eqs.(B4) and (B6) into Eq.(B2), and neglecting the Lamb–shift terms that simply renormalize the coherent dynamics, we ob-

tain

$$\begin{aligned}
\frac{d\hat{\rho}^I}{dt} &= \frac{1}{2} \sum_{\mu\nu k} \sum_{\mu'\nu'k'} X_{\mu\nu k} X_{\mu'\nu'k'} e^{i(\Delta_{\mu\nu k} - \Delta_{\mu'\nu'k'})t} \times \\
&J(\Delta_{\mu\nu k}) n_{th}(\Delta_{\mu\nu k}) [|\phi_\alpha\rangle \langle\phi_\beta| \hat{\rho}^I |\phi_{\beta'}\rangle \langle\phi_{\alpha'}| \\
&- |\phi_{\beta'}\rangle \langle\phi_{\alpha'}| \phi_\alpha\rangle \langle\phi_\beta| \hat{\rho}^I] + \frac{1}{2} \sum_{\mu\nu k} \sum_{\mu'\nu'k'} X_{\mu\nu k} X_{\mu'\nu'k'} \times \\
&e^{i(\Delta_{\mu\nu k} - \Delta_{\mu'\nu'k'})t} J(-\Delta_{\mu\nu k}) (n_{th}(-\Delta_{\mu\nu k}) + 1) \times \\
&[|\phi_\alpha\rangle \langle\phi_\beta| \hat{\rho}^I |\phi_{\beta'}\rangle \langle\phi_{\alpha'}| - |\phi_{\beta'}\rangle \langle\phi_{\alpha'}| \phi_\alpha\rangle \langle\phi_\beta| \hat{\rho}^I] + \text{h.c.}
\end{aligned} \tag{B7}$$

Here, the bath's spectral density is defined as

$$J(\omega) = 2\pi \sum_i g_i^2 \delta(\omega - \omega_i), \tag{B8}$$

which vanishes for  $\omega < 0$ . To cast Eq. (B7) into Lindblad form, one typically invokes the full secular approximation [53, 55], retaining only terms with  $(\mu', \nu', k') = (\mu, \nu, k)$ . This approximation is valid only if different Floquet transition frequencies are well separated, i.e.,

$$|\Delta_{\mu'\nu'k'} - \Delta_{\mu\nu k}| \gg |X_{\mu'\nu'k'} X_{\mu\nu k}| \kappa(\Delta_{\mu\nu k}) \tag{B9}$$

for  $(\mu', \nu', k') \neq (\mu, \nu, k)$  with  $\kappa(\Delta_{\mu\nu k})$  defined in Eq. (12). However, in the Kerr-cat qubit, the spectrum exhibits multiple near-degeneracies (“spectral kissing,” see Fig.3), violating Eq.(B9). Instead, we employ the partial secular approximation: transitions satisfying Eq. (B9) are discarded, but those with

$$|\Delta_{\mu'\nu'k'} - \Delta_{\mu\nu k}| \lesssim |X_{\mu'\nu'k'} X_{\mu\nu k}| \kappa(\Delta_{\mu\nu k}) \tag{B10}$$

are retained, see for instance Refs. [78–82]. For these quasidegenerate pairs we approximate  $e^{i(\Delta_{\mu\nu k} - \Delta_{\mu'\nu'k'})t} \approx 1$ , consistent with the Born–Markov accuracy (i.e., neglecting terms  $\mathcal{O}(g_i^4) = \mathcal{O}(\kappa^2)$  [78–81]).

For compactness, we group transitions into classes  $[\alpha, \beta, k]$ , where  $(\mu', \nu', k') \in [\mu, \nu, k] \iff |\Delta_{\mu\nu k} - \Delta_{\mu'\nu'k'}| \lesssim |X_{\mu'\nu'k'} X_{\mu\nu k}| \kappa(\Delta_{\mu\nu k})$ . In terms of these classes, the master equation interaction-picture becomes

$$\frac{d\hat{\rho}^I}{dt} = \mathcal{L}\hat{\rho}^I, \tag{B11}$$

with the Lindbladian

$$\mathcal{L} = \sum_{[\mu, \nu, k]} \kappa(\Delta_{\mu\nu k}) \mathcal{D} \left[ \sum_{(\mu', \nu', k') \in [\mu, \nu, k]} X_{\mu'\nu'k'} |\phi_{\mu'}\rangle \langle\phi_{\nu'}| \right]. \tag{B12}$$

In this expression, the first sum runs over the distinct classes of transitions, and the second sum runs over quasidegenerate transitions within a given class.

By construction, this Lindbladian naturally accounts for strong drive effects through the Floquet quasienergies  $\Delta_{\mu\nu k}$  and Floquet modes  $|\phi_\mu\rangle$ , including all perturbative and nonperturbative corrections beyond the

rotating-wave approximation [46, 74, 83–85]. Moreover, the coefficients  $X_{\mu\nu k}$  represent transition amplitudes between Floquet modes  $|\phi_\nu\rangle \rightarrow |\phi_\mu\rangle$  assisted by  $|k|$  photons from the drive. Although the Lindbladian itself connects time-independent Floquet modes, the full temporal dependence of the driven dynamics is encoded in these coefficients through the time-dependent Floquet modes, see Eq. (10). Thus, the master equation captures not only the stroboscopic evolution but also the fast micromotion dynamics.

In the absence of quasidegeneracies—i.e., when each class  $[\mu, \nu, k]$  contains only a single transition—the master equation reduces to the standard Floquet–Markov secular form. Crucially, when quasidegeneracies occur, the resulting dissipator

$$\mathcal{D} \left[ \sum_{(\mu', \nu', k') \in [\mu, \nu, k]} X_{\mu'\nu'k'} |\phi_{\mu'}\rangle \langle\phi_{\nu'}| \right] \tag{B13}$$

captures interference effects among transitions within the same class. This contrasts sharply with the incoherent sum of dissipators

$$\sum_{(\mu', \nu', k')} |X_{\mu'\nu'k'}|^2 \mathcal{D} [|\phi_{\mu'}\rangle \langle\phi_{\nu'}|], \tag{B14}$$

which results from applying the usual secular approximation.

Finally, because quasidegenerate transitions survive the partial secular treatment, the steady state  $\hat{\rho}_\infty^I$  (or “limit cycle,” satisfying  $\mathcal{L}\hat{\rho}_\infty^I = 0$ ) is not necessarily diagonal in the Floquet mode basis. For instance, in the Kerr-cat qubit, finite tunneling times and intrawell leakage produce a steady-state mixture of localized well states that retains coherences between Floquet modes.

It is instructive to compare our partial-secular Floquet–Markov equation Eq. (7) with other extensions of the Lindblad formalism for quasidegenerate spectra (e.g., Refs. [86–90]). In our treatment, the partial-secular approximation necessarily introduces an explicit threshold for grouping transitions, see Eq. (B10); in our regime of parameters, we define two transitions  $\Delta_{\mu\nu k}$  and  $\Delta_{\mu'\nu'k'}$  as quasidegenerate when  $|\Delta_{\mu\nu k} - \Delta_{\mu'\nu'k'}|/2\pi < 100$  kHz. By contrast, alternative approaches avoid any fixed threshold but at the expense of retaining an explicitly time-dependent Lindbladian even in the interaction picture—making relevant quantities such as the Liouvillian gap not well-defined. Here, the Lindbladian in Eq. (7) remains time-independent. Moreover, when expressed in the Floquet-mode basis  $\{|\phi_\mu\rangle\}$ , it is highly sparse, making both its diagonalization and the simulation of the driven dynamics efficient in memory usage and computation time.

### Appendix C: Further details of tunneling time calculation

To obtain the tunneling time as would be done via heterodyne detection in an experiment, we use an ideal likelihood discriminator. First, let us denote  $\hat{\rho}_{\pm}(t)$  the evolved state at time  $t$  where the initial condition is  $\hat{\rho}_{\pm}(0) = |\beta \pm \alpha\rangle\langle\beta \pm \alpha|$ . At each time step, we obtain the Husimi-Q distributions of the evolved states denoted by  $Q_{\pm}[\gamma](t) = \langle\gamma|\hat{\rho}_{\pm}(t)|\gamma\rangle/\pi$ . Here  $|\gamma\rangle$  is a coherent state. We then construct the log-likelihood function  $\lambda(t) \equiv \ln(Q_{+}(t)/Q_{-}(t))$ . When the state is initialized in  $\hat{\rho}_{+}(0)$ , the probability

$$P(+|+) = \int d^2\gamma \Theta[\lambda(t)]Q_{+}(t), \quad (\text{C1})$$

where  $\Theta$  is the Heaviside function, would be the probability of correctly assigning the outcome “+” from a single-shot reading of the heterodyne signal at time  $t$ . Likewise, when the state is initialized in  $\hat{\rho}_{-}(0)$ ,

$$P(-|-) = \int d^2\gamma \Theta[-\lambda(t)]Q_{-}(t), \quad (\text{C2})$$

would be the probability of correctly assigning the outcome “-” from a single-shot reading. The (averaged) assignment error is therefore  $\frac{1}{2}[P(-|+) + P(+|-)] = 1 - \frac{1}{2}[P(+|+) - P(-|-)]$ . Following Refs. [30, 32–34], we extract the tunneling time by fitting a single-exponential decay to

$$X_{+}(t) = P(+|+) - P(-|+) = 1 - 2P(-|+) \quad (\text{C3})$$

for the initial condition  $\hat{\rho}_{+}(0)$ , and

$$X_{-}(t) = P(+|-) - P(-|-) = 2P(+|-) - 1 \quad (\text{C4})$$

for  $\hat{\rho}_{-}(0)$ . Numerically, these two tunneling time estimates agree closely. In the main text, we report their average.

### Appendix D: Approximate Floquet Hamiltonian

To obtain an analytical expression for the Floquet Hamiltonian using perturbation theory, it is convenient to first transform the original time-periodic Hamiltonian into a time-independent form using the Shirley (Fourier) space formalism [91]. In this representation, we then apply a time-independent Schrieffer–Wolff (SW) transformation to block-diagonalize the Hamiltonian perturbatively [92]. This method, which involves only time-independent operators and transformations, can be more transparent and intuitive.

An alternative approach avoids the mapping to Shirley space and instead applies a time-dependent SW transformation directly in the original time domain [83, 93–97]. This technique has been recently used to analyze  $T_1$

degradation in a dissipatively stabilized cat qubit [74], and to derive effective Lindblad operators for the Kerr-cat [39].

We begin by expanding  $\hat{H}_s$  from Eq. (5) in a power series around the minimum of its potential, yielding

$$\hat{H}_s = \omega_0 \hat{a}^\dagger \hat{a} + \sum_{n \geq 3} \frac{g_n}{n} (\hat{a} + \hat{a}^\dagger)^n, \quad (\text{D1})$$

where the coefficients are given by  $g_n = E_J c_n \varphi_{\text{zpf}}^n / (n-1)!$ . Here,  $c_n$  denotes the  $n$ th derivative of the cosine potential evaluated at the minimum. Using the relation  $E_J = \omega_0 / (2c_2 \varphi_{\text{zpf}}^2)$ , we can rewrite the coefficients as  $g_n = \omega_0 c_n \varphi_{\text{zpf}}^{n-2} / (2c_2 (n-1)!)$ . This makes explicit that the coefficients of the nonlinearity scale as  $g_3 \sim \mathcal{O}(\omega_0 \varphi_{\text{zpf}})$ ,  $g_4 \sim \mathcal{O}(\omega_0 \varphi_{\text{zpf}}^2)$ , and so on. These are naturally small parameters governed by the dimensionless zero-point fluctuations of the phase,  $\varphi_{\text{zpf}}$ . The perturbative expansion introduced below is organized in powers of  $\varphi_{\text{zpf}}$ .

We then add the charge drive to  $\hat{H}_s$ , resulting in the time-dependent Hamiltonian

$$\begin{aligned} \hat{H}(t) = & \omega_0 \hat{a}^\dagger \hat{a} + \sum_{n \geq 3} \frac{g_n}{n} (\hat{a} + \hat{a}^\dagger)^n \\ & + \frac{i\varepsilon_d}{4\varphi_{\text{zpf}}} \cos(\omega_d t + \lambda) (\hat{a}^\dagger - \hat{a}), \end{aligned} \quad (\text{D2})$$

where we have included a phase delay  $\lambda$  for generality. Following Ref. [30], we eliminate the drive term and fold it into the nonlinear potential transforming the Hamiltonian with a time-dependent displacement operator  $\hat{D}[\beta(t)] = \exp[\beta(t)\hat{a}^\dagger - \bar{\beta}(t)\hat{a}]$ , where the displacement amplitude is

$$\begin{aligned} \beta(t) = & \frac{\varepsilon_d}{4i\varphi_{\text{zpf}}} \left( \frac{e^{-i(\omega_d t + \lambda)}}{\omega_0 - \omega_d} + \frac{e^{i(\omega_d t + \lambda)}}{\omega_0 + \omega_d} \right) \\ = & \frac{\omega_d + \omega_0}{2\omega_d} \Pi e^{-i\omega_d t} + \frac{\omega_d - \omega_0}{2\omega_d} \bar{\Pi} e^{+i\omega_d t}, \end{aligned} \quad (\text{D3})$$

with the compact coefficient

$$\Pi = \frac{\varepsilon_d \omega_d e^{-i\lambda}}{2i\varphi_{\text{zpf}}(\omega_0^2 - \omega_d^2)} \quad (\text{D4})$$

which becomes useful below. In this section of the appendix, we use an overbar to denote complex conjugation.

The Hamiltonian in the displaced and rotating frame, with the additional rotation  $\hat{R}(t) = \exp[-i(\omega_d/2)\hat{a}^\dagger \hat{a}, t]$ , takes the form

$$\begin{aligned} \hat{H}_d(t) \equiv & \hat{R}^\dagger \left[ \hat{D}^\dagger \hat{H} \hat{D} - i\hat{D}^\dagger \dot{\hat{D}} \right] \hat{R} - i\hat{R}^\dagger \dot{\hat{R}} \\ = & (\omega_0 - \omega_d/2) \hat{a}^\dagger \hat{a} \\ & + \sum_{n \geq 3} \frac{g_n}{n} (\hat{a} e^{-i\frac{\omega_d}{2}t} + \Pi e^{-i\omega_d t} + \text{h.c.})^n. \end{aligned} \quad (\text{D5})$$

Crucially, since  $\omega_d/2 \approx \omega_0$ , all terms in this Hamiltonian are small in magnitude except for the rapid oscillations

introduced by the drive frequency  $\omega_d$ . For all parameter regimes considered in this work, the displacement amplitude satisfies  $|\Pi| < 1$ .

A straightforward rotating-wave approximation (RWA) applied to this Hamiltonian yields a squeezed Kerr oscillator, as in Eq. (1), with two-photon drive amplitude  $\varepsilon_2 = g_3\Pi$  and self-Kerr coefficient  $K = (3/2)g_d$ . The drive frequency must be tuned to account for the ac Stark shift, satisfying  $\omega_d/2 = \omega_0 + 3(1 + 2|\Pi|^2)$ .

While this RWA captures the basic structure, a more accurate description can be obtained via a SW perturbative expansion. Once we obtain the approximate Floquet Hamiltonian in this displaced and rotated frame, we construct the Floquet Hamiltonian in the laboratory frame by undoing the rotation and displacement transformations, as explained below in this section.

The usual time-dependent SW transformation for periodically driven systems consists of finding a hermitian generator  $\hat{G}(t)$  such that a time-independent Hamiltonian  $\hat{H}_F^d$  is obtained from the transformation [94], namely

$$e^{i\hat{G}(t)}[\hat{H}_d(t) - i\partial_t]e^{-i\hat{G}(t)} = \hat{H}_F^d - i\partial_t. \quad (\text{D6})$$

While the original Hamiltonian in Eq. (4) is periodic with period  $T = 2\pi/\omega_d$ , the displaced and rotated Hamiltonian is  $2T$ -periodic, and so the generator  $\hat{G}(t)$  is  $2T$ -periodic as well. Importantly,  $\hat{G}(t)$  does not vanish at stroboscopic times,  $\hat{G}(2mT) \neq 0$  (where  $m$  is an integer), and is thus referred to as the *non-stroboscopic kick operator*. The resulting time-independent Hamiltonian  $\hat{H}_F$  is known as the *non-stroboscopic Floquet Hamiltonian* [94]. A feature of this formalism is that  $\hat{H}_F$  is independent of the phase delay  $\lambda$  in the drive—or, equivalently, of the choice of the initial time. This is in contrast to the conventional (stroboscopic) Floquet Hamiltonian, which carries such a gauge dependence.

Rather than working directly with the time-dependent expression in Eq. (D6), we find it convenient to construct the Schrieffer–Wolff generator in the Shirley space [91]. In this extended Hilbert space, the operator  $\hat{H}_d(t) - i\partial_t$  is mapped to the Shirley Hamiltonian

$$\hat{H}_S = \frac{\omega_d}{2}\hat{m} \otimes \hat{\mathbf{1}} + \sum_{n=-\infty}^{\infty} \hat{\mathbf{1}}_{-n} \otimes \hat{H}_n, \quad (\text{D7})$$

where the  $\hat{H}_n$  are the Fourier components of the original time-dependent Hamiltonian in the displaced and rotated frame,

$$\hat{H}_d(t) = \sum_{n=-\infty}^{\infty} \hat{H}_n e^{in\frac{\omega_d}{2}t}, \quad (\text{D8})$$

Here,  $\hat{m} = \sum_m m|m\rangle\langle m|$  acts on the replica space, which accounts for the harmonics of the drive, and  $\hat{\mathbf{1}}_n = \sum_m |m\rangle\langle m+n|$  are ladder operators that shift the replica index. The full Hamiltonian  $\hat{H}_S$  thus acts on a tensor product of two spaces: the infinite-dimensional

replica space (first factor) and the original system Hilbert space (second factor).

The generator is mapped to Shirley space as

$$\hat{G}(t) = \sum_n \hat{G}_n e^{in(\omega_d/2)t} \rightarrow \hat{G} = \sum_n \hat{\mathbf{1}}_{-n} \otimes \hat{G}_n. \quad (\text{D9})$$

where  $\hat{G} = \hat{G}^\dagger$  and  $\hat{G}_n^\dagger = \hat{G}_{-n}$  to ensure hermiticity. As in standard SW perturbation theory, we construct the generator order by order, requiring that the transformed Hamiltonian be diagonal. In this case, however, we only demand diagonalization in the replica index, not in the full Shirley space. Specifically, we enforce the structure

$$\hat{H}'_S = e^{i\hat{G}} \hat{H}_S e^{-i\hat{G}} \stackrel{!}{=} \frac{\omega_d}{2}\hat{m} \otimes \hat{\mathbf{1}} + \hat{\mathbf{1}} \otimes \hat{H}_F^d, \quad (\text{D10})$$

where the right-hand side is the Shirley-space representation of a time-independent Hamiltonian  $\hat{H}_F^d$  in the Hilbert space. This ensures that  $\hat{H}_F^d$  captures the effective dynamics up to the desired order.

Let us now identify the small parameter that controls the perturbative expansion. In the standard Schrieffer–Wolff transformation, the expansion parameter is given by the ratio of the coupling strength between subspaces to their energy detuning. In our case, the smallest detuning in the diagonal part of  $\hat{H}_S$  is set by  $\omega_0$ , while the off-diagonal couplings have magnitude  $g_n$ , so the relevant small parameter is  $g_n/\omega_0 \propto \varphi_{\text{zpf}}^{n-2}$ . Crucially, since  $g_n/g_{n+1} \propto \varphi_{\text{zpf}}^{-1}$ , we can treat  $\varphi_{\text{zpf}}$  as the single small parameter controlling the entire expansion. This greatly simplifies the analysis, avoiding the need to treat each  $g_n$  individually as an independent perturbation.

We thus expand each operator  $\hat{H}_n$  and  $\hat{G}_n$  in powers of the small parameter  $\varphi_{\text{zpf}}$  as

$$\begin{aligned} \hat{H}_n &= \sum_{k \geq 0} \hat{H}_n^{(k)} \\ \hat{G}_n &= \sum_{k \geq 1} \hat{G}_n^{(k)} \end{aligned} \quad (\text{D11})$$

where the superscript  $(k)$  denotes terms of order  $\varphi_{\text{zpf}}^k$ . Note that the zeroth-order term of  $\hat{G}_n$  vanishes,  $\hat{G}_n^{(0)} = 0$ , since the Schrieffer–Wolff transformation needs to be reduced to the identity at zero order.

We expand  $\hat{H}'_S$  in Eq. (D10) as

$$\begin{aligned} \hat{H}'_S &= \\ &\left( \hat{H}_S^{(0)} \right) \\ &+ \left( \hat{H}_S^{(1)} + i[\hat{G}^{(1)}, \hat{H}_S^{(0)}] \right) \\ &+ \left( \hat{H}_S^{(2)} + i[\hat{G}^{(1)}, \hat{H}_S^{(1)}] - \frac{1}{2}[\hat{G}^{(1)}, [\hat{G}^{(1)}, \hat{H}_S^{(0)}]] \right. \\ &\quad \left. + i[\hat{G}^{(2)}, \hat{H}_S^{(0)}] \right) \\ &+ \dots, \end{aligned} \quad (\text{D12})$$

where each parentheses group terms of the same perturbative order. As usual in a Schrieffer–Wolff transformation, the generator at order  $k$ ,  $\hat{G}^{(k)} = \sum_n \hat{\mathbf{1}}_{-n} \otimes \hat{G}_n^{(k)}$ , is chosen such that the transformed Hamiltonian is diagonal at order  $k$ —in this case, diagonal in the replica index.

### 1. Zero order

At zeroth order, the transformed Shirley Hamiltonian is simply

$$\hat{H}'_S{}^{(0)} = \hat{H}_S^{(0)} = \frac{\omega_d}{2} \hat{m} \otimes \mathbf{1} + \mathbf{1} \otimes \hat{H}_0^{(0)}, \quad (\text{D13})$$

where  $\hat{H}_0^{(0)} = (\omega_0 - \omega_d/2) \hat{a}^\dagger \hat{a}$ . Thus, the Floquet Hamiltonian at zeroth order is simply  $\hat{H}_F^{d(0)} = \hat{H}_0^{(0)}$ , as expected.

### 2. First order

At first order, we require  $\hat{G}^{(1)}$  to cancel the off-diagonal terms in the replica index that appear in

$$\hat{H}'_S{}^{(1)} + i[\hat{G}^{(1)}, \hat{H}'_S{}^{(0)}]. \quad (\text{D14})$$

Since  $\hat{H}'_S{}^{(0)}$  is diagonal and  $\hat{G}^{(1)}$  is off-diagonal, the commutator  $[\hat{G}^{(1)}, \hat{H}'_S{}^{(0)}]$  is also off-diagonal. Therefore, the diagonal part of  $\hat{H}'_S{}^{(1)}$  becomes

$$\hat{H}'_S{}^{(1)} = \text{diag}(\hat{H}'_S{}^{(1)}) = \hat{\mathbf{1}} \otimes \hat{H}_0^{(1)} \quad (\text{D15})$$

with

$$\hat{H}_0^{(1)} = g_3(\Pi \hat{a}^{\dagger 2} + \bar{\Pi} \hat{a}^2). \quad (\text{D16})$$

Thus, the first-order Floquet Hamiltonian is  $\hat{H}_F^{d(1)} = \hat{H}_0^{(1)}$ . To first order in  $\varphi_{\text{zpf}}$ , this reproduces the two-photon drive term  $\varepsilon_2 = g_3 \Pi$ , consistent with the RWA.

For  $\hat{G}^{(1)}$  to cancel the off-diagonal terms in Eq. (D14), we need that,

$$0 \stackrel{!}{=} \hat{H}'_n{}^{(1)} - in \frac{\omega_d}{2} \hat{G}_n^{(1)} + i(\omega_0 - \frac{\omega_d}{2}) [\hat{G}_n^{(1)}, \hat{a}^\dagger \hat{a}], \quad (\text{D17})$$

for all  $n \neq 0$ .

We note that the first-order index-off-diagonal terms  $\hat{H}'_n{}^{(1)}$  are:

$$\begin{aligned} \hat{H}'_1{}^{(1)} &= g_3[\hat{a}^{\dagger 2} \hat{a} + (1 + 2|\Pi|^2) \hat{a}^\dagger] \\ \hat{H}'_2{}^{(1)} &= g_3 \bar{\Pi} (2 \hat{a}^\dagger \hat{a} + 1 + |\Pi|^2) \\ \hat{H}'_3{}^{(1)} &= \frac{g_3}{3} (\hat{a}^{\dagger 3} + 3 \bar{\Pi} \hat{a}^2) \\ \hat{H}'_4{}^{(1)} &= g_3 \bar{\Pi} \hat{a}^{\dagger 2} \\ \hat{H}'_5{}^{(1)} &= g_3 \bar{\Pi}^2 \hat{a}^\dagger \\ \hat{H}'_6{}^{(1)} &= \frac{g_3}{3} \bar{\Pi}^3. \end{aligned} \quad (\text{D18})$$

From these, we obtain

$$\begin{aligned} \hat{G}_1^{(1)} &= \frac{-ig_3}{\omega_0} [\hat{a}^{\dagger 2} \hat{a} + (1 + 2|\Pi|^2) \hat{a}^\dagger] \\ \hat{G}_2^{(1)} &= \frac{-ig_3}{\omega_d} \bar{\Pi} (2 \hat{a}^\dagger \hat{a} + 1 + |\Pi|^2) \\ \hat{G}_3^{(1)} &= \frac{-ig_3}{9\omega_0} \hat{a}^{\dagger 3} - \frac{ig_3}{2\omega_d - \omega_0} \bar{\Pi}^2 \hat{a} \\ \hat{G}_4^{(1)} &= \frac{-ig_3}{2\omega_0 + \omega_d} \bar{\Pi} \hat{a}^{\dagger 2} \\ \hat{G}_5^{(1)} &= \frac{-ig_3}{\omega_0 + 2\omega_d} \bar{\Pi}^2 \hat{a}^\dagger \\ \hat{G}_6^{(1)} &= \frac{-ig_3}{9\omega_d} \bar{\Pi}^3. \end{aligned} \quad (\text{D19})$$

### 3. Second order

The second-order terms in the SW expansion are

$$\begin{aligned} \hat{H}'_S{}^{(2)} + i[\hat{G}^{(1)}, \hat{H}'_S{}^{(1)}] - \frac{1}{2} [\hat{G}^{(1)}, [\hat{G}^{(1)}, \hat{H}'_S{}^{(0)}]] \\ + i[\hat{G}^{(2)}, \hat{H}'_S{}^{(0)}]. \end{aligned} \quad (\text{D20})$$

The second-order generator  $\hat{G}^{(2)}$ , which we do not write explicitly here, is determined by requiring that the off-diagonal terms in the replica index cancel out. The remaining diagonal terms simplify significantly for our Hamiltonian and reduce to

$$\hat{\mathbf{1}}_0 \otimes \left( \hat{H}_0^{(2)} + \frac{i}{2} \sum_n [\hat{G}_n^{(1)}, \hat{H}'_{-n}{}^{(1)}] \right), \quad (\text{D21})$$

yielding the second-order contribution to the Floquet Hamiltonian:

$$\hat{H}_F^{d(2)} = \Delta \hat{a}^\dagger \hat{a} - K \hat{a}^{\dagger 2} \hat{a}^2, \quad (\text{D22})$$

with

$$\begin{aligned} \Delta &= 3g_4(1 + 2|\Pi|^2) \\ &\quad - 4g_3^2 \left[ \frac{5 + 6|\Pi|^2}{3\omega_0} + \frac{|\Pi|^2}{2\omega_0 + \omega_d} \right] \\ K &= -\frac{3g_4}{2} + \frac{10g_3^2}{\omega_0}. \end{aligned} \quad (\text{D23})$$

Thus, the Floquet Hamiltonian in the displaced and rotated frame, up to second order, is

$$\begin{aligned} \hat{H}_F^d &= \left( \omega_0 - \frac{\omega_d}{2} + \Delta \right) \hat{a}^\dagger \hat{a} - K \hat{a}^{\dagger 2} \hat{a}^2 \\ &\quad + \varepsilon_2 \hat{a}^{\dagger 2} + \bar{\varepsilon}_2 \hat{a}^2, \end{aligned} \quad (\text{D24})$$

with  $\varepsilon_2 = g_3 \Pi$ . We note that setting  $\Pi = 0$  and  $\omega_d = 0$  recovers an approximate diagonalization of the undriven SNAIL Hamiltonian in Eq. (5), as expected, since we are removing off-diagonal terms proportional to  $\varphi_{\text{zpf}}$ .

#### 4. Floquet Hamiltonian in the laboratory frame

We begin by expressing the relation between a state in the displaced and rotating frame  $|\psi(t)\rangle_d$  and the laboratory frame  $|\psi(t)\rangle$ ,

$$|\psi(t)\rangle_d = \hat{R}^\dagger(t) \hat{D}^\dagger(t) |\psi(t)\rangle. \quad (\text{D25})$$

This state evolves under the Hamiltonian  $\hat{H}_d(t)$  via

$$|\psi(t)\rangle_d = \mathcal{T} \exp \left[ -i \int_0^t d\tau \hat{H}_d(\tau) \right] \times |\psi(0)\rangle_d \quad (\text{D26})$$

where  $\hat{H}_d(t)$  is given in Eq. (D5). Since  $\hat{R}(0) = \hat{\mathbf{1}}$  but  $\hat{D}(0) \neq \hat{\mathbf{1}}$ , the initial state in the displaced and rotating frame is

$$|\psi(0)\rangle_d = \hat{D}^\dagger(0) |\psi(0)\rangle. \quad (\text{D27})$$

The Schrieffer-Wolff transformation constructed in the previous subsections defines a generator  $\hat{G}(t)$  such that the state

$$|\psi(t)\rangle_{d,G} \equiv e^{i\hat{G}(t)} |\psi(t)\rangle_d \quad (\text{D28})$$

evolves under the time-independent Floquet Hamiltonian  $\hat{H}_F^d$  introduced in Eq. (D6) according to

$$\begin{aligned} |\psi(t)\rangle_{d,G} &= e^{-it\hat{H}_F^d} |\psi(0)\rangle_{d,G} \\ &= e^{-it\hat{H}_F^d} e^{i\hat{G}(0)} \hat{D}^\dagger(0) |\psi(0)\rangle. \end{aligned} \quad (\text{D29})$$

We thus recover the state in the lab frame as

$$|\psi(t)\rangle = \hat{U}(t) |\psi(0)\rangle, \quad (\text{D30})$$

with an explicit form of the lab-frame propagator given by

$$\hat{U}(t) = \hat{D}(t) \hat{R}(t) e^{-i\hat{G}(t)} e^{-it\hat{H}_F^d} e^{i\hat{G}(0)} \hat{D}^\dagger(0). \quad (\text{D31})$$

Evaluating this operator at  $t = T$ , we obtain an explicit form for the stroboscopic Floquet propagator in the lab frame,  $\hat{U}(T) \equiv \exp(-iT\hat{H}_F)$ , which is the operator used in our numerical calculations. Since  $\hat{D}(T) = \hat{D}(0)$ , and using the identity  $\hat{R}(T) e^{-i\hat{G}(T)} = e^{-i\hat{G}(0)} \hat{R}(T)$ , we can rewrite the propagator as

$$\hat{U}(T) = \hat{D}(0) e^{-i\hat{G}(0)} \hat{R}(T) e^{-iT\hat{H}_F^d} e^{i\hat{G}(0)} \hat{D}^\dagger(0). \quad (\text{D32})$$

Next, we observe that  $\hat{R}(T) = e^{-i\pi\hat{a}^\dagger\hat{a}}$  is the parity operator and commutes with  $\hat{H}_F^d$ , since the latter conserves parity [see Eq. (D24)]. Thus, we can write the Floquet-mode decomposition

$$\hat{U}(T) = \sum_{\mu} e^{-iT\epsilon_{\mu}} |\phi_{\mu}\rangle \langle\mu|, \quad (\text{D33})$$

with

$$|\phi_{\mu}(0)\rangle \equiv \hat{D}(0) e^{-i\hat{G}(0)} |\phi_{\mu}^d\rangle \quad (\text{D34})$$

relating the lab-frame Floquet modes to the displaced-and-rotated frame Floquet modes  $|\phi_{\mu}^d\rangle$ , and

$$e^{-iT\epsilon_{\mu}} \equiv e^{-iT[\epsilon_{\mu}^d + \frac{\omega_d}{2} \bmod(\mu, 2)]} \quad (\text{D35})$$

relating the lab-frame Floquet quasienergies to the displaced-and-rotated-frame Floquet eigenenergies  $\epsilon_{\mu}^d$ . Here,  $\epsilon_{\mu}^d$  and  $|\phi_{\mu}^d\rangle$  are eigenenergies and eigenstates, respectively, of the Hamiltonian  $\hat{H}_F^d$ . It can be shown that the Floquet modes in the lab frame—which evolve under  $e^{it\epsilon_{\mu}} \hat{U}(t)$ —are  $T$ -periodic functions of time.

Let us clarify the relationship between the eigenenergies  $\epsilon_{\mu}^d$  of the displaced-and-rotated-frame Floquet Hamiltonian defined in Eq. (D6) and the quasienergies in the lab frame  $\epsilon_{\mu}$ . The eigenenergies  $\epsilon_{\mu}^d$  are not folded—they can grow unbounded—while the lab-frame quasienergies  $\epsilon_{\mu}$  are defined modulo the drive frequency, and therefore lie within a Brillouin zone, which we take to be  $[-\omega_d/2, +\omega_d/2]$ . See Fig. 12(a) for the corresponding numerical spectrum in the lab frame. This distinction arises because the non-stroboscopic Floquet Hamiltonian  $\hat{H}_F^d$  is not defined via the stroboscopic propagator, unlike the standard Floquet Hamiltonian, whose quasienergies are inherently folded into the Brillouin zone. In our case, the appropriate folding to obtain the lab-frame quasienergies from the eigenvalues  $\epsilon_{\mu}^d$  of  $\hat{H}_F^d$  is given by:

$$\epsilon_{\mu} = \begin{cases} [(\epsilon_{\mu}^d + \frac{\omega_d}{2}) \bmod \omega_d] - \frac{\omega_d}{2} & \text{if } \mu \text{ is even,} \\ [\epsilon_{\mu}^d \bmod \frac{\omega_d}{2}] - \frac{\omega_d}{2} & \text{if } \mu \text{ is odd.} \end{cases}$$

#### 5. Floquet matrix elements for the master equation

In the previous subsection, we constructed the Floquet spectrum in the laboratory frame in terms of the spectrum of the squeezed Kerr Hamiltonian, for which approximate analytical expressions are available (see, e.g., Ref. [20]). Building on this, we now derive approximate expressions for the matrix elements  $X_{\mu\nu k}$  appearing in Eq. (10), which govern the dynamics in the Floquet-Markov master equation.

We begin by noting that

$$|\phi_{\mu}(t)\rangle = e^{it(\epsilon_{\mu} - \epsilon_{\mu}^d)} \hat{D}(t) \hat{R}(t) e^{-i\hat{G}(t)} |\phi_{\mu}^d(0)\rangle. \quad (\text{D36})$$

Rather than applying these operators to the Floquet modes on the right-hand side, we apply them to the annihilation operator, working to first order in  $\varphi_{\text{zpf}}$ . We define

$$\begin{aligned} \tilde{a}(t) &\equiv e^{i\hat{G}(t)} \hat{R}^\dagger(t) \hat{D}^\dagger(t) \hat{a} \hat{D}(t) \hat{R}(t) e^{-i\hat{G}(t)} \\ &= \hat{a} e^{-i\frac{\omega_d}{2}t} + \beta(t) + i[\hat{G}^{(1)}(t), \hat{a}] e^{-i\frac{\omega_d}{2}t} \\ &= \sum_n \tilde{a}_n e^{in\frac{\omega_d}{2}t}, \end{aligned} \quad (\text{D37})$$

with the following Fourier coefficients to first order in  $\varphi_{\text{zpf}}$ :

$$\begin{aligned}
\tilde{a}_{-4} &= -\frac{g_3}{2\omega_d - \omega_0} \Pi^2 \\
\tilde{a}_{-3} &= \frac{2g_3}{\omega_d} \Pi \hat{a} \\
\tilde{a}_{-2} &= \frac{g_3}{\omega_0} \hat{a}^2 + \frac{\omega_d + \omega_0}{2\omega_d} \Pi \\
\tilde{a}_{-1} &= \hat{a} \\
\tilde{a}_0 &= -\frac{g_3}{\omega_0} [2\hat{a}^\dagger \hat{a} + 1 + 2|\Pi|^2] \\
\tilde{a}_1 &= -\frac{2g_3}{\omega_d} \bar{\Pi} \hat{a} \\
\tilde{a}_2 &= -\frac{g_3}{3\omega_0} \hat{a}^{\dagger 2} + \frac{\omega_d - \omega_0}{2\omega_d} \bar{\Pi} \\
\tilde{a}_3 &= -\frac{2g_3}{2\omega_0 + \omega_d} \bar{\Pi} \hat{a}^\dagger \\
\tilde{a}_4 &= -\frac{g_3}{\omega_0 + 2\omega_d} \bar{\Pi}^2.
\end{aligned} \tag{D38}$$

We now define the coefficients  $\tilde{p}_n$  such that

$$\begin{aligned}
i[\tilde{a}^\dagger(t) - \tilde{a}(t)] &= \sum_n i(\tilde{a}_{-n}^\dagger - \tilde{a}_n) e^{in\frac{\omega_d}{2}t} \\
&\equiv \sum_n \tilde{p}_n e^{in\frac{\omega_d}{2}t},
\end{aligned} \tag{D39}$$

and are given by

$$\begin{aligned}
\tilde{p}_0 &= 0 \\
\tilde{p}_1 &= i\hat{a}^\dagger + \frac{2ig_3}{\omega_d} \bar{\Pi} \hat{a} \\
\tilde{p}_2 &= i\frac{\omega_0}{\omega_d} \bar{\Pi} + \frac{4ig_3}{3\omega_0} \hat{a}^{\dagger 2} \\
\tilde{p}_3 &= \frac{4ig_3(\omega_0 + \omega_d)}{\omega_d(2\omega_0 + \omega_d)} \bar{\Pi} \hat{a}^\dagger \\
\tilde{p}_4 &= -2ig_3 \bar{\Pi}^2 \frac{\omega_0}{4\omega_d^2 - \omega_0^2},
\end{aligned} \tag{D40}$$

and  $\tilde{p}_{-n} = \tilde{p}_n^\dagger$ . These coefficients enter the matrix elements of interest as

$$i \langle \phi_\mu(t) | (\hat{a}^\dagger - \hat{a}) | \phi_\nu(t) \rangle = e^{it(\epsilon_\nu - \epsilon_\mu + \epsilon_\mu^d - \epsilon_\nu^d)} \sum_n \langle \phi_\mu^d | \tilde{p}_n | \phi_\nu^d \rangle e^{in\frac{\omega_d}{2}t}, \tag{D41}$$

We can now compute some of the matrix elements. Let us first introduce the definition

$$\theta_{\mu,\nu} \equiv \epsilon_\nu - \epsilon_\mu + \epsilon_\mu^d - \epsilon_\nu^d. \tag{D42}$$

We begin with modes 0 and 1, which are always kissed. We got  $\theta_{0,1} = -\omega_d/2$  and  $\theta_{1,0} = \omega_d/2$  [see Fig. 12(a)], thus

$$\begin{aligned}
X_{010} &= \langle \phi_0^d | \tilde{p}_1 | \phi_1^d \rangle \approx i\bar{\alpha} + \frac{2ig_3}{\omega_d} \bar{\Pi} \alpha \\
X_{101} &= \langle \phi_1^d | \tilde{p}_1 | \phi_0^d \rangle \approx i\bar{\alpha} + \frac{2ig_3}{\omega_d} \bar{\Pi} \alpha,
\end{aligned} \tag{D43}$$

therefore,  $X_{010} - X_{101} \approx 0$ ; c.f. Fig. 4(a).

When levels 2 and 3 kiss, we get  $\theta_{2,3} = -\omega_d/2$  and  $\theta_{3,2} = \omega_d/2$ . Using the approximate expressions [20]

$$\begin{aligned}
|\phi_2^d\rangle &\approx (1/\sqrt{2})[\hat{D}(\alpha) - \hat{D}(-\alpha) |n=1\rangle \\
|\phi_3^d\rangle &\approx (1/\sqrt{2})[\hat{D}(\alpha) + \hat{D}(-\alpha) |n=1\rangle,
\end{aligned} \tag{D44}$$

for the eigenstates of the squeezed Kerr Hamiltonian at zero detuning, we have  $\hat{a} |\phi_2^d\rangle \approx |\phi_1^d\rangle + \alpha |\phi_3^d\rangle$  and  $\hat{a} |\phi_3^d\rangle \approx |\phi_0^d\rangle + \alpha |\phi_2^d\rangle$  and so

$$\begin{aligned}
X_{230} &= \langle \phi_2^d | \tilde{p}_1 | \phi_3^d \rangle \approx i\bar{\alpha} + \frac{2ig_3}{\omega_d} \bar{\Pi} \alpha \\
X_{321} &= \langle \phi_3^d | \tilde{p}_1 | \phi_2^d \rangle \approx i\bar{\alpha} + \frac{2ig_3}{\omega_d} \bar{\Pi} \alpha,
\end{aligned} \tag{D45}$$

as in Eq. (D43). The same expressions are obtained for the others  $X_{\mu(\mu+1)0}$  and  $X_{(\mu+1)\mu k}$ .

The matrix elements associated with the main source of leakage are  $X_{210}$  and  $X_{301}$ , which correspond to single-photon absorption from the bath. We have  $\theta_{2,1} = -\omega_d/2$  and  $\theta_{3,0} = \omega_d/2$ , thus

$$\begin{aligned}
X_{210} &= \langle \phi_2^d | \tilde{p}_1 | \phi_1^d \rangle \approx i \\
X_{301} &= \langle \phi_3^d | \tilde{p}_1 | \phi_0^d \rangle \approx i.
\end{aligned} \tag{D46}$$

Other matrix elements of interest are  $X_{201}$  and  $X_{311}$ , which correspond to two-photon absorption. In both cases we have  $\theta_{2,0} = \theta_{3,1} = 0$ , thus

$$\begin{aligned}
X_{201} &= \langle \phi_2^d | \tilde{p}_2 | \phi_0^d \rangle \approx \frac{8ig_3\bar{\alpha}}{3\omega_0} \\
X_{311} &= \langle \phi_3^d | \tilde{p}_2 | \phi_1^d \rangle \approx \frac{8ig_3\bar{\alpha}}{3\omega_0}.
\end{aligned} \tag{D47}$$

## Appendix E: Buffer mode

### 1. Perturbative expansion accounting for the buffer mode

Here, we revisit the perturbative expansion used to derive the Floquet Hamiltonian, now including the buffer mode. We show that accurately capturing the hybridization discussed in Sec. III A—between low-lying Floquet modes and those with a single buffer excitation—requires carrying the expansion to very high order in the nonlinearities, making the perturbative approach impractical for quantitative work, even though it can still offer analytic insight into quantities such as Floquet matrix elements. As an illustrative example, we show that the leading-order coupling between  $|\phi_{7s,0b}\rangle$  and  $|\phi_{17s,1b}\rangle$  appears only at order  $\mathcal{O}(\varphi_{\text{zpf}}^7)$ .

We start from the SNAIL–buffer Hamiltonian  $\hat{H}_{sb}$  in Eq. (3) and move to the frame in which the driven SNAIL Hamiltonian  $\hat{H}(t)$  becomes time-independent.

This transformation is generated by the kick operator  $e^{i\hat{K}(t)}$  defined as [55, 94]

$$\hat{U}(t) = e^{-i\hat{K}(t)} e^{-it\hat{H}_F}, \quad (\text{E1})$$

with  $\hat{K}(t+T) = \hat{K}(t)$ . In this frame,

$$\begin{aligned} \hat{H}_{sb}^{\text{eff}} &= e^{i\hat{K}(t)} \hat{H}_{sb} e^{-i\hat{K}(t)} + i(\partial_t e^{i\hat{K}(t)}) e^{-i\hat{K}(t)} \\ &= \hat{H}_F + \omega_b \hat{a}_b^\dagger \hat{a}_b \\ &\quad + i g n_{\text{zpf}} (\hat{a}_b^\dagger - \hat{a}_b) e^{i\hat{K}(t)} i (\hat{a}^\dagger - \hat{a}) e^{-i\hat{K}(t)}, \end{aligned} \quad (\text{E2})$$

where  $\hat{H}_F$  is the Floquet Hamiltonian of the laboratory frame. So far, we have transformed the problem of two modes with static coupling under a drive into an equivalent one with a time-independent bare Hamiltonians coupled via a time-dependent coupling. Importantly, using our analytic results for the single-mode case presented in Appendix D, we can evaluate the transition amplitude from  $|\phi_\nu, 0_b\rangle$  to  $|\phi_\mu, 1_b\rangle$ . Substituting Eq. (D31) and Eq. (D36) in Eq. (E1) yields

$$\begin{aligned} e^{i\hat{K}(t)} i (\hat{a}^\dagger - \hat{a}) e^{-i\hat{K}(t)} &= \sum_{\mu\nu n} e^{i(\theta_{\mu,\nu} + n\omega_d/2)t} \langle \phi_\mu^d | \tilde{p}_n | \phi_\nu^d \rangle \\ &\quad \times |\phi_\mu\rangle \langle \phi_\nu|, \end{aligned} \quad (\text{E3})$$

where  $\tilde{p}_n$  and  $\theta_{\mu,\nu}$  are defined in Eqs. (D39) and (D42). Finally, moving to the interaction picture  $|\phi_\mu\rangle \langle \phi_\nu| \rightarrow e^{i(\epsilon_\mu - \epsilon_\nu)t} |\phi_\mu\rangle \langle \phi_\nu|$  and  $\hat{a}_b \rightarrow \hat{a}_b e^{-i\omega_b t}$ , we find that transitions  $|\phi_\nu, 0_b\rangle \rightarrow |\phi_\mu, 1_b\rangle$  can only occur when  $n = 2$  and  $\Delta_{bd} \approx \epsilon_\mu^d - \epsilon_\nu^d$ , with  $\epsilon_\mu^d$  and  $\epsilon_\nu^d$  the eigenenergies of  $\hat{H}_F^d$ . For  $\mu = 17_s$  and  $\nu = 7_s$ , the amplitude is proportional to  $\langle \phi_{17}^d | \tilde{p}_2 | \phi_7^d \rangle$ . Because these states have the same parity, the leading coupling arises from  $\hat{a}^{\dagger 2k}$  terms. Since  $\tilde{p}_2$  is the Fourier component at  $\omega_d$ , we know from Eq. (D5) that terms with  $\hat{a}^{\dagger 2k}$  come as  $\sim \varphi_{\text{zpf}}^{(3k-2)} \hat{a}^{\dagger 2k} \Pi^{k-1}$ . To identify the dominant  $k$ , we numerically evaluate  $|\varphi_{\text{zpf}}^{(3k-2)} \Pi^{k-1} \langle \phi_{17}^d | \hat{a}^{\dagger 2k} | \phi_7^d \rangle|$  with  $|\phi_7^d\rangle$  and  $|\phi_{17}^d\rangle$  approximated by the corresponding eigenstates of the squeezed-Kerr oscillator, see e.g., Ref. [20]. The matrix elements peak at  $k = 3$ , confirming that the leading coupling indeed scales as  $\sim \varphi_{\text{zpf}}^7$ . In this illustrative case, knowing which states hybridize at some particular drive amplitude allows us to determine the required expansion order; in general, such information is unavailable, making a full nonlinear potential treatment indispensable.

## 2. Negative detuning

In the main text, we examined the buffer mode with its frequency chosen above the drive frequency, as in experimental implementations [30, 34]. We showed that energy collisions between low-lying levels ( $i_s, 0_b$ ) and ( $j_s, 1_b$ ) with  $i_s < j_s$  occur at moderate drive amplitude because

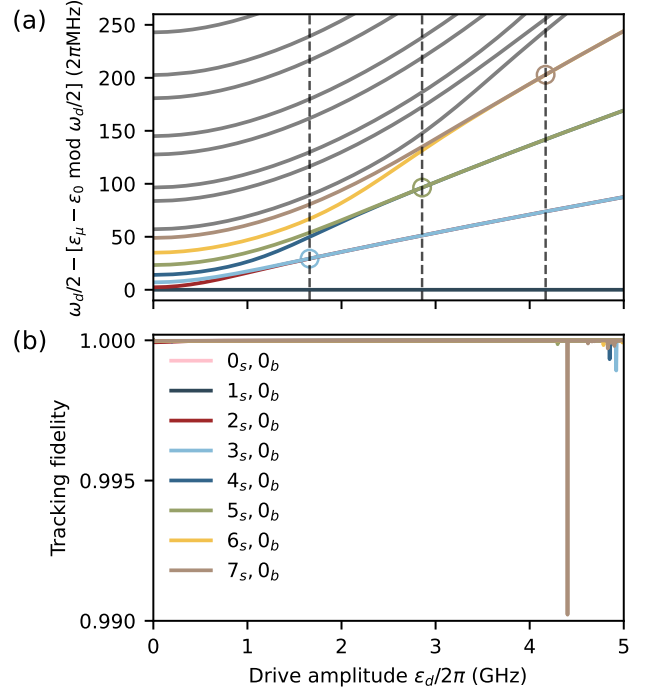


FIG. 13. (a) Floquet spectrum of the Kerr-cat qubit coupled to a buffer mode detuned below the drive  $\Delta_{bd}/2\pi = (\omega_b - \omega_d)/2\pi \approx -285$  MHz, i.e., the opposite regime from Fig. 8 in the main text. (b) Floquet-state tracking fidelity  $|\langle \phi_\mu[\varepsilon_d] | \phi_\mu[\varepsilon_d + \delta\varepsilon_d] \rangle|^2$ , which remains essentially unity for all relevant states. A slight ( $< 1\%$ ) drop is observed for the  $(7_s, 0_b)$  state, along with even smaller dips near 5 GHz. These deviations are due to crossings with very high-energy quasienergies such as  $\epsilon_{122s, 2b}$  and are only artifacts of our finite Hilbert-space truncation ( $160 \times 6$ ).

the negative Stark shift of the transition  $\epsilon_{j_s, 1_b} - \epsilon_{i_s, 0_b}$  can compensate its initial detuning at  $\varepsilon_d = 0$ , namely  $\Delta_{bd} - (j_s(j_s - 1) - i_s(i_s - 1))K$ . From this argument it follows that these resonances can be avoided simply by choosing  $\Delta_{bd} < 0$ , i.e., placing the buffer mode below the drive frequency. In Fig. 13(a) we set  $\Delta_{bd} = -285$  MHz, —the same magnitude used in Sec. III, but negative—and plot the Floquet spectrum versus drive amplitude for states with zero buffer excitations. Unlike the  $\Delta_{bd} > 0$  case where single-buffer-excitation levels cross the zero-excitation manifold at  $\varepsilon_d/2\pi \in (2.8, 5)$  GHz; see Fig. 8(a), here all one buffer mode excitation levels remain at least 300 MHz above the relevant zero-excitation levels (i.e.,  $\omega_d - (\varepsilon_{j_s, 1_b} - \varepsilon_{0_s, 0_b} \bmod \omega_d/2) \geq 300$  MHz), placing them outside the plotted range. As a result, we recover the uninterrupted spectral-kissing structure of the single mode case.

This conclusion is confirmed in Fig. 13(b), which shows the Floquet-state tracking fidelity  $|\langle \phi_\mu[\varepsilon_d] | \phi_\mu[\varepsilon_d + \delta\varepsilon_d] \rangle|^2$ , which remains essentially unity for all relevant levels. Only a slight ( $< 1\%$ ) drop for the  $7_s, 0_b$  state—which, in any case, does not affect the tunneling time, see Sec. III—along with even smaller dips near  $\varepsilon_d/2\pi \approx 5$  GHz. These

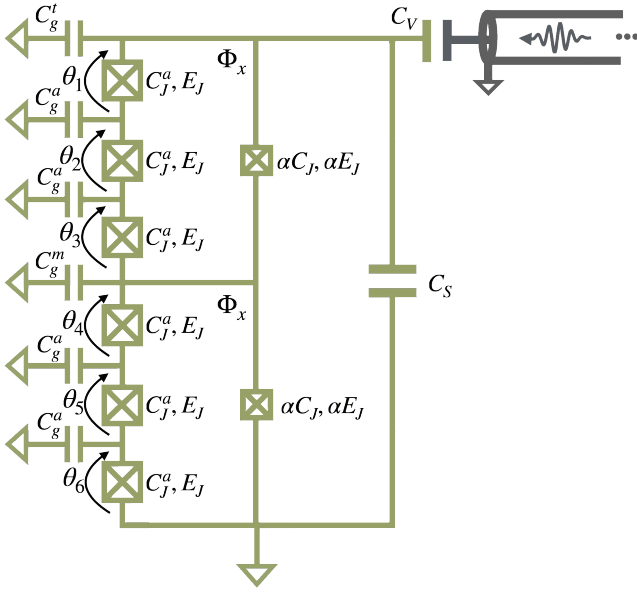


FIG. 14. Circuit diagram of the shunted double SNAIL capacitively coupled to the drive line. Each island in the array is connected to ground through a parasitic ground capacitance.

features are artifacts of our finite Hilbert-space truncation ( $160 \times 5$ ), marking the practical limit of the chosen basis size at this large drive amplitude.

In summary, placing the buffer mode below the drive is an effective strategy to suppress buffer-induced resonances in the low-lying manifold, reproducing the large tunneling times of the ideal single-mode case. In more complex circuits with multiple buffer modes (e.g., Ref. [33]), careful engineering of each mode's frequency is essential to avoid multimode transitions and fully recover single-mode robustness.

## Appendix F: SNAIL array modes

Figure 14 shows a more detailed schematic of the double-SNAIL circuit analyzed in Sec. IV. We first work out the Lagrangian in the absence of the ground capacitances  $C_g^a$ ,  $C_g^m$ , and  $C_g^t$ . These will be incorporated later.

In terms of the fluxes  $\{\theta_j\}_{j=1}^6$  across the large junc-

tions, the Lagrangian reads

$$\begin{aligned}
 \mathcal{L} = & \frac{C_J^a}{2} \sum_{i=1}^6 \dot{\theta}_i^2 + \frac{C_V}{2} \left( \sum_{i=1}^6 \dot{\theta}_i - V \right)^2 \\
 & + \frac{C_S}{2} \left( \sum_{i=1}^6 \dot{\theta}_i \right)^2 \\
 & + \frac{\alpha C_J^a}{2} \left[ \left( \sum_{i=1}^3 \dot{\theta}_i \right)^2 + \left( \sum_{i=4}^6 \dot{\theta}_i \right)^2 \right] \\
 & + E_J \sum_{i=1}^6 \cos \left( \frac{2\pi}{\Phi_0} \theta_i \right) \\
 & + \alpha E_J \cos \left( \frac{2\pi}{\Phi_0} \sum_{i=1}^3 \theta_i + \varphi_x \right) \\
 & + \alpha E_J \cos \left( \frac{2\pi}{\Phi_0} \sum_{i=4}^6 \theta_i + \varphi_x \right)
 \end{aligned} \tag{F1}$$

Following Ref. [60], we perform a change of variables based on the symmetries of the circuit that decouples the kinetic energy terms. There is permutation symmetry among  $\{\theta_1, \theta_2, \theta_3\}$ , among  $\{\theta_4, \theta_5, \theta_6\}$ , and a swap between these two triplets  $\{\theta_1, \theta_2, \theta_3\} \leftrightarrow \{\theta_4, \theta_5, \theta_6\}$ . It is thus convenient to introduce the collective flux variables  $\{\phi, \phi_-, \xi_1, \xi_2, \chi_1, \chi_2\}$ , which are linear combinations of the original variables defined as

$$\begin{aligned}
 \theta_i &= \frac{\phi + \phi_-}{6} + \sum_{\mu=1}^2 W_{\mu,i} \xi_\mu, \quad i = 1, 2, 3 \\
 \theta_i &= \frac{\phi - \phi_-}{6} + \sum_{\mu=1}^2 W_{\mu,i-3} \chi_\mu, \quad i = 4, 5, 6,
 \end{aligned} \tag{F2}$$

where  $W$  is a  $(2 \times 3)$  semiorthogonal matrix, with the properties  $\sum_{i=1}^3 W_{\mu,i} = 0$  and  $\sum_{i=1}^3 W_{\mu,i} W_{\nu,i} = \delta_{\mu\nu}$  [60]. In particular, we have that the collective flux used in the single-phase approximation corresponds to  $\phi = \sum_{i=1}^6 \theta_i$ . As we explain below, the other collective mode that plays an important role is  $\phi_- = \theta_1 + \theta_2 + \theta_3 - (\theta_4 + \theta_5 + \theta_6)$ . While  $\phi$  is symmetric under all three groups of symmetries,  $\phi_-$  is antisymmetric under the swap of the triplets. In terms of the new variables, the Lagrangian of the

double-SNAIL circuit becomes

$$\begin{aligned}
\mathcal{L} = & \frac{C}{2} \dot{\phi}^2 - C_V \dot{\phi} V \\
& + \frac{C_-}{2} \dot{\phi}_-^2 \\
& + \frac{C_J^a}{2} \sum_{\mu=1}^2 (\xi_\mu^2 + \chi_\mu^2) \\
& + E_J \sum_{i=1}^3 \cos \left( \frac{\varphi + \varphi_-}{6} + \frac{2\pi}{\Phi_0} \sum_{\mu=1}^2 W_{\mu,i} \xi_\mu \right) \\
& + E_J \sum_{i=1}^3 \cos \left( \frac{\varphi - \varphi_-}{6} + \frac{2\pi}{\Phi_0} \sum_{\mu=1}^2 W_{\mu,i} \chi_\mu \right) \\
& + 2\alpha E_J \cos \left( \frac{\varphi}{2} + \varphi_{\text{ext}} \right) \cos \left( \frac{\varphi_-}{2} \right).
\end{aligned} \tag{F3}$$

Here, we introduced the reduced fluxes  $\varphi = 2\pi\phi/\Phi_0$  and  $\varphi_- = 2\pi\phi_-/\Phi_0$ , and defined  $C = C_J^a(1/6 + \alpha/2) + C_S + C_V$ , and  $C_- = C_J^a(1/6 + \alpha/2)$ . Note that the kinetic energy terms are now decoupled, and the modes interact only through the nonlinearity. Owing to the properties of the matrix  $W$ , the potential minimum occurs at  $\phi_- = \chi_\mu = \xi_\mu = 0$  and  $\varphi = \varphi_{\text{min}} \neq 0$ . Setting  $\phi_- = \chi_\mu = \xi_\mu = 0$  amounts to ignoring the five high-energy modes and recovers the single-phase approximation, which is given by

$$\begin{aligned}
\mathcal{L}_{\text{SP}} = & \frac{C}{2} \dot{\phi}^2 + \frac{C_V}{2} (\dot{\phi} - V)^2 \\
& + 6E_J \cos \left( \frac{\varphi}{6} \right) + 2\alpha E_J \cos \left( \frac{\varphi}{2} + \varphi_{\text{ext}} \right)
\end{aligned} \tag{F4}$$

and leads to the Hamiltonian expressed in Eqs. (4) and (5).

The Hamiltonian associated with Eq. (F3) is straightforward to obtain. To determine the plasma frequencies of the circuit modes, we first identify the minimum of the potential energy. For the parameters used throughout the main text, see Fig. 1—namely,  $E_J/2\pi = 272.436$  GHz,  $E_C/2\pi = 107.8$  MHz,  $\alpha = 0.046$ , and  $\varphi_{\text{ext}} = 0.33 \times 2\pi$ —the minimum is located at  $\varphi_{\text{min}} = 0.255$ . Choosing  $(C_S + C_V)/C_J^a = 2.83$  leads to the following plasma frequencies

$$\begin{aligned}
\omega_{p,+} = & \sqrt{8E_C E_{J,+}} = 2\pi \times 6.096 \text{ GHz} \\
\omega_{p,-} = & \sqrt{8\beta E_C E_{J,-}} = 2\pi \times 24.43 \text{ GHz} \\
\omega_{p,\mu} = & \sqrt{8\beta_\mu E_C E_{J,\mu}} = 2\pi \times 26.31 \text{ GHz}
\end{aligned} \tag{F5}$$

corresponding to the symmetric mode, the antisymmetric mode, and the remaining four transverse modes, respectively. Here,  $\beta = C/C_- \approx 16.1$  and  $\beta_\mu = C/C_J^a \approx 3$  are ratios of the total effective capacitance of each mode. The quantity  $E_{J,x}$  denotes the curvature of the potential along mode  $x$  at the minimum, i.e.,  $E_{J,x} = E_J \left( \frac{d^2 U}{dx^2} \right)_{\text{min}}$ .

When we include the ground capacitances shown in Fig. 14, the Lagrangian in Eq. (F3) acquires an extra

kinetic energy contribution that can be written in matrix form as  $(1/2)\boldsymbol{\theta}^\top \mathbf{C}_0 \boldsymbol{\theta}$ , where  $\boldsymbol{\theta}^\top = (\theta_1, \dots, \theta_6)$  and the (normalized) matrix  $\mathbf{C}_0/C_g^t$  is given by

$$\begin{pmatrix}
1 & 1 & 1 & 1 & 1 & 1 \\
1 & 1 & 1 & 1 & 1 & 1 \\
1 & 1 & 1+2a & 1+2a & 1+2a & 1+2a \\
1 & 1 & 1+2a & 1+m+2a & 1+m+2a & 1+m+2a \\
1 & 1 & 1+2a & 1+m+2a & 1+m+3a & 1+m+3a \\
1 & 1 & 1+2a & 1+m+2a & 1+m+3a & 1+m+4a
\end{pmatrix},$$

with  $a = C_g^a/C_g^t$  and  $m = C_g^m/C_g^t$ ; see Fig. 14. Transforming this matrix to the new basis defined by Eq. (F2) and including it in Eq. (F3) gives the full circuit Lagrangian in terms of the collective modes. After obtaining the full Hamiltonian, we choose the value of the capacitances to obtain three energies quoted in Sec. IV, namely  $E_C/2\pi = 107.8$  MHz,  $\beta \approx 16.1$  and  $g/2\pi = 100$  MHz. We do so by considering  $C_g^a = C_g^t = C_g^m$  for simplicity, and fixing the ratio  $C_g^a/C_J^a = 0.03$  and an updated ratio  $(C_S + C_V)/C_J^a = 3.074$ . This choice gives us the correct value for  $\beta$  and fixes the proportionality between  $E_C$  and  $g$ . The only remaining free parameter is  $C_J^a$ , which fixes their values. The plasma frequencies of the transversal modes become

$$\begin{aligned}
\omega_{p,\xi_1}/2\pi = & 27.124 \text{ GHz} \\
\omega_{p,\xi_2}/2\pi = & 27.378 \text{ GHz} \\
\omega_{p,\chi_1}/2\pi = & 27.113 \text{ GHz} \\
\omega_{p,\chi_2}/2\pi = & 27.369 \text{ GHz},
\end{aligned} \tag{F6}$$

and the charge-charge coupling energies between the symmetric mode and each of these transversal modes are

$$\begin{aligned}
g_{\xi_1}/2\pi = & 21.8 \text{ MHz} \\
g_{\xi_2}/2\pi = & -12.6 \text{ MHz} \\
g_{\chi_1}/2\pi = & 7.7 \text{ MHz} \\
g_{\chi_2}/2\pi = & 1.5 \text{ MHz}.
\end{aligned} \tag{F7}$$

We note that these parameters are obtained from the full Hamiltonian without approximation: the exact inverse of the capacitance matrix is used to construct the Hamiltonian. Eq. (F7) confirms that, among the high-energy collective modes, the lowest-energy mode—the antisymmetric mode—couples much more strongly to the symmetric mode than the others. The same conclusion was reached in Refs. [60, 61, 72], where a perturbative expansion in the ground capacitance ratio  $C_g^a/C_J^a$  was used.

It is worth remarking that in Sec. IV, we could have tuned the plasma frequency of the antisymmetric mode to more closely resemble the scenario with the buffer mode. The value we chose was  $\omega_- \approx 2\omega_d + 2\pi \times 54$  MHz. If we have instead chosen  $\omega_- \approx 2\omega_d + 2\pi \times 300$  MHz, the antisymmetric mode would mediate multiphoton resonances similar to those found in the buffer-mode case. For instance, the resonance between  $(17_s, 1_b)$  and  $(7_s, 0_b)$  discussed in Sec. III for the buffer mode would have a

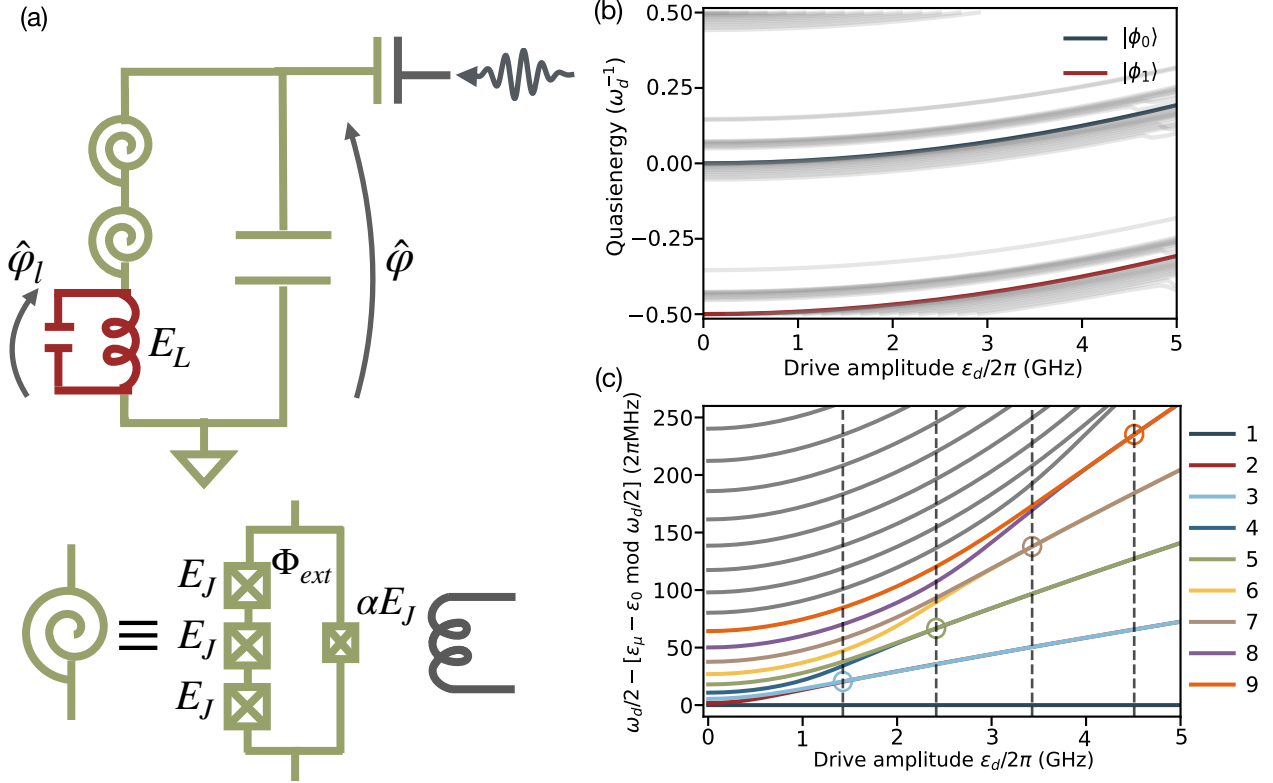


FIG. 15. (a) Circuit implementation of the Kerr-cat qubit used in Refs. [30, 33, 34], now explicitly including the finite geometric inductance (red). Because the inductive energy  $E_L$  is comparable to the SNAIL Josephson energy  $E_J$ , usual expansions in  $E_J/E_L$  cannot be used. Instead, we account for the inductance by retaining the high-frequency inductive mode that arises from the finite self-capacitance (red capacitor). (b) Floquet spectrum versus drive amplitude for the lowest 50 levels. The first two Floquet modes—representing the cat states—are highlighted in dark blue and red. (c) Spectral-kissing pattern in the presence of the serial inductor, matching the behavior observed in the single mode case.

analog here, with the energy difference

$$E_{17s,1a} - E_{7s,0a} \approx 7\omega_d + (\omega_- - 2\omega_d) - K(17 \cdot 16 - 7 \cdot 6), \quad (\text{F8})$$

which could be bridged by the ac-Stark shift, leading to an energy difference an integer multiple of the drive frequency, causing a multiphoton resonance, just as in the buffer-mode case.

However, the values of the ground capacitances assumed here are deliberately exaggerated to probe a worst-case scenario. In practice, these capacitances are expected to be significantly smaller, resulting in a weaker charge-charge coupling between the Kerr cat qubit and the array modes. We therefore hypothesize that, regardless of the array-mode frequencies, it is hybridization with the buffer mode that sets the dominant limitation on Kerr-cat coherence in current experiments.

### Appendix G: Stray geometric inductance

In this Appendix, we assess the impact of the serial inductance present in the circuit implementation of the

Kerr-cat qubit in Refs. [30, 33, 34] as shown in Fig. 15(a). Recent work [26] has shown that such inductances can nontrivially renormalize the circuit potential and can degrade the performance of dissipative cat qubits if not properly optimized. Here we show that, although this serial inductance does modify the double-SNAIL potential [98], its effect on the Kerr-cat spectrum is minimal and does not affect the Kerr-cat qubit's performance.

A common approach to include the serial inductance in the circuit description is to adiabatically eliminate the very high-frequency mode introduced by the small intrinsic self-capacitances in parallel with the inductor (see the red capacitor in Fig. 15(a)), then perform a perturbative expansion in the typically small parameter  $E_J/E_L$ , where  $E_L$  is the inductive energy, to obtain an effective single-mode potential which accounts for the presence of the inductance; see for instance Ref. [99] for more details. That approach leads to higher Josephson harmonics in the cosine potential and improves predictions of the onset of measurement-induced transitions in strongly driven circuits [48–50]. However, this method requires  $E_J \ll E_L$ . In the Kerr-cat experiments of Refs. [30, 33, 34],  $E_L \sim E_J$ , so the  $E_J/E_L$  expansion cannot be used. Instead,

Ref. [98] incorporated the inductance by renormalizing the coefficients of the Taylor expansion of the potential about its minimum. While valid for the regime of parameters of interest, this method does not account for the full nonlinear potential and may therefore miss drive-activated multiphoton resonances that could be present if the full circuit nonlinearities are retained [47].

Here, following Ref. [26], we forgo any perturbative expansion by explicitly including the high-frequency inductance mode and retaining the full cosine potential

$$\hat{H}_{sl} = 4E_C \hat{n}^2 + U_s(\hat{\phi} - \hat{\phi}_l) + \omega_l \hat{a}_l^\dagger \hat{a}_l, \quad (\text{G1})$$

where  $U_s$  is the double-SNAIL potential from Eq. (5), and

$$\hat{\phi}_l = \sqrt{\omega_l/2E_L}(\hat{a}_l + \hat{a}_l^\dagger), \quad (\text{G2})$$

is the reduced phase of the inductive mode of frequency  $\omega_l$ . We choose parameters close to those in Refs. [30, 34], namely  $E_L/2\pi = 214.55$  GHz,  $E_J/2\pi = 273.28$  GHz and  $E_C/2\pi = 129.87$  MHz. In Eq. (G1), the inductive phase  $\hat{\phi}_l$  couples to the SNAIL phase  $\hat{\phi}$  via  $U_s$ . Diagonalizing  $\hat{H}_{sl}$  yields dressed eigenstates that we label as  $|i_s, j_l\rangle$ , where  $i_s$  and  $j_l$  are the SNAIL and inductance-mode excitations. For this diagonalization, we use a Hilbert space of 250 Fock states in the SNAIL mode and 10 Fock states in the inductance mode, then retain the lowest 250 eigenlevels. We then add a charge drive on the SNAIL mode and perform the Floquet analysis as before, yielding Floquet modes  $|\phi_{i_s, j_l}\rangle$ . In particular, the cat states  $|\phi_{0_s, 0_l}\rangle$ ,  $|\phi_{1_s, 0_l}\rangle$ , along with all other relevant Kerr-cat levels, now fully account for the presence of the inductance while at the same time encompass all circuit nonlinearities.

Because the impedance of a geometric inductance  $Z_l = \omega_l L$  cannot exceed the vacuum impedance,  $Z_{\text{vac}} \approx 376.73 \Omega$  [100], this sets an upper bound on  $\omega_l$ . Taking  $Z_l \approx Z_{\text{vac}}$  gives  $\omega_l/2\pi \approx 80$  GHz. Although we present results for these values, varying  $Z_l$  and thus  $\omega_l$  over other realistic ranges yields the same conclusion.

The Floquet spectrum shown in Fig. 15(b) closely resembles that of the single-mode case (Sec. II), exhibiting no resonances for the drive amplitudes considered here (up to  $\approx 20$  photons in the cat manifold). Moreover, because the inductance mode lies at much higher frequency, any levels involving its excitation lie well above the manifold of interest and do not perturb the low-lying spectrum. We therefore conclude that—even though the serial inductance renormalizes the circuit potential (e.g., modifying the self-Kerr and third-order nonlinearities)—the overall structure of the Kerr-cat spectrum—e.g., the spectral-kissing shown in Fig. 15(c)—remains unchanged, and we observe the same physics as in the single-mode case.